University of Alberta

Adsorbent materials for the separation and purification of carbon dioxide

by

Brenden Michael Stephen Tanchuk

A thesis submitted to the Faculty of Graduate Studies and Research
in partial fulfillment of the requirements for the degree of

Master of Science

in

Chemical Engineering

Department of Chemical and Materials Engineering

Fall 2013

Edmonton, Alberta

Abstract

Two separations are necessary to enable the post-combustion capture of CO_2. The fraction of CO_2 in a flue gas stream must first be separated from the diluents present and then the concentrated stream of CO_2 must be thoroughly dried in order for it to be compressed for sequestration. This work characterized the first non-porous, amine grafted nano-titanate adsorbents and probed their characteristics for CO_2 removal from flue gas. This work also established the adsorbent, instrumentation, and process considerations prerequisite to developing an adsorptive CO_2 drying process.

Engelhard Titanosilicate 2 (ETS-2) was chosen as a substrate for amine grafting due to its high surface area (~300 m^2/g), native surface hydroxyl concentration, and lack of microporosity; eliminating the risk of fouling the adsorbent under certain process conditions. Aminosilanes containing a single (N1), two (N2), and three (N3) amine groups were chemically grafted to the surface of Na-ETS-2 substrates. The N3 sample displayed complete monolayer coverage and was capable of adsorbing five times as much atmospheric CO_2 as the N1 sample.

An ideal desiccant for drying CO_2 should have a high moisture capacity and selectivity, and should be regenerable using low-grade waste heat and humid ambient air. The CO_2 drying performance of Na-, Ca-, and Ca/H- forms of ETS-10 were compared to that of commercial silica and zeolite desiccants. Ca-ETS-10 was found to have the highest moisture capacity with a temperature swing of 30-70°C using over a CO_2 feed stream at 50–100% relative humidity and a humid regeneration air stream.

Acknowledgements

I would like to lead off by expressing my gratitude to my supervisor, Dr. S. M. Kuznicki for his guidance and leadership, along with the latitude he allowed me to pursue my own hunches and ideas throughout the course of my research. His expectations coupled with his trust and support have enabled me to achieve more than I would have thought possible when I first walked into his office at the beginning of my program.

I would also like to especially thank Dr. J. Sawada for his support and assistance designing, constructing, commissioning, rebuilding, writing, proofing, presenting, and talking for the past two years. My journey would not have been what it was without you.

P. Swenson for somehow tricking me into thinking this would all be a good idea, and for being right. Your friendship and support have been key to my continued sanity.

A. Zeko and Dr. T. Kuznicki for their assistance in manuscript preparation.

W. An, L. Wu, M. Shi, J. Kim, J. Smith, B. Olson, N. Robertson for their support, assistance, and advice.

And most importantly, my love and thanks to J. Peck for her love and support through our past seven years together; For her faith and belief in me, for tolerating those late nights in the lab, and for being my best friend and partner.

Table of Contents

List of Tables

List of Figures

Nomenclature

Abbreviations

AS	aminosilane
DEA	diethanolamine
DEG	diethylene glycol
EDX	energy dispersive X-ray spectroscopy
EOR	enhanced oil recovery
ETS-10	Engelhard Titanosilicate 10
ETS-2	Engelhard Titanosilicate 2
FW	formula weight
HMS	hexagonal mesoporous silica
ID	inner diameter
MDEA	methyldiethanolamine
MEA	monoethanolamine
MFC	mass flow controller
MS	mass spectroscopy
OD	outer diameter
OECD	Organization for Economic Co-operation and Development
PCC	post combustion capture
PEI	polyethylenimine
PSA	pressure swing adsorption
RH	relative humidity
SEM	scanning electron microscopy

T_4EG	tetraethylene glycol
TEG	triethylene glycol
TG	thermogravimetric
TGA	thermogravimetric analysis
TG-MS	thermogravimetric mass spectroscopy
TSA	temperature swing adsorption
Wt	weight
XRD	X-ray diffraction

Symbols

Å	angstrom
e_w	partial pressure of water vapor
e^*_w	saturated vapor pressure
H_{ppmv}	humidity in ppmv
P	total pressure
T	temperature
T_{dp}	dewpoint
ϕ	Relative humidity

1. Introduction

1.1 Carbon Dioxide Capture, Storage, and Utilization

1.1.1 Carbon Dioxide

Carbon dioxide is a chemical compound consisting of a single carbon atom covalently bonded to a pair of oxygen atoms. It exists in the atmosphere naturally at a concentration of 0.039 percent by volume. Carbon dioxide is produced naturally by a number of biological processes including fermentation and cellular respiration, and is emitted from volcanos and other thin areas of the earth's crust. The main source of human released carbon dioxide is the combustion of fossil fuels, the simplest example of which is the combustion of methane shown here

$$CH_4 + 2O_2 \rightarrow CO_2 + 2H_2O$$

The United Nations reported in 2009 that global anthropogenic carbon dioxide emissions were approximately 30 billion tonnes (United Nations Statistics Division 2012). This number had steadily increased over the ten previous years as developing nations increase their energy utilization. This increase is projected to continue with total global CO_2 emissions reaching 35.2 billion tonnes by 2020 and 43.2 billion tonnes by 2035 (United States Energy Information Administration 2011). Figure 1-1 shows the evolution of this projection as well as the historical CO_2 emissions back to 1990.

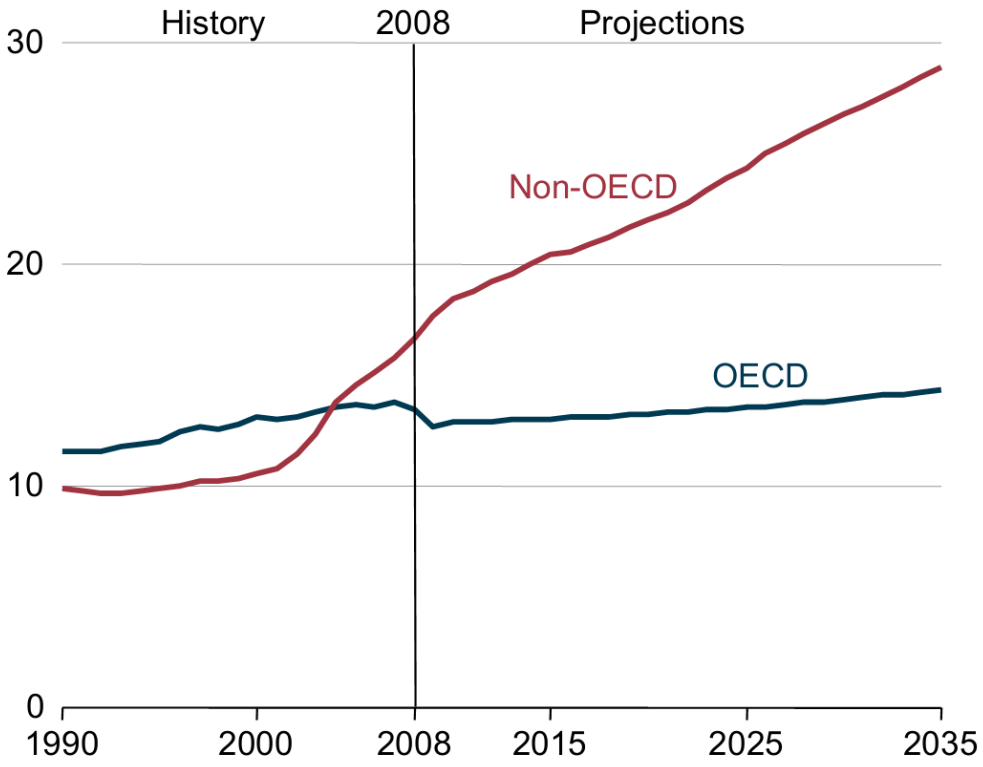

Figure 1-1. Global energy related CO_2 emissions, 1990-2035 (projected) in billions of tonnes for Organisation for Economic Co-operation and Development (OECD) members and nonmembers (United States Energy Information Administration 2011)

current levels production, the atmospheric levels of CO_2 have increased to 380 ppm from 280 ppm in the early 1900s (Solomon, et al. 2007). The projected increases in emissions are anticipated to in turn further raise the concentration of CO_2 in the atmosphere. These past and future increases are attributed to as one of the major causes of increasing the greenhouse effect of the atmosphere and thereby significantly contributing to global warming.

1.1.2 Carbon Dioxide Capture

A direct method of reducing CO_2 emissions is to reduce fossil fuel consumption either through alternative energy sources or systemic social changes to use less

energy. However with alternative sources unable to match the scale and mobility of fossil fuels and developing nations growing need for energy, these solutions are infeasible for the foreseeable future. One alternative, indirect solution which has been proposed is the post combustion capture (PCC) of CO_2, whereby emissions would be reduced by selectively removing CO_2 from flue gas streams at point sources such as coal or natural gas fired power plants. Such a flue gas stream would contain significant amounts of nitrogen, carbon dioxide, water vapor and trace amounts of carbon monoxide, partially combusted hydrocarbons, sulphur oxides (SO_x) and nitrous oxides (NO_x). Once the CO_2 in the flue gas is concentrated and purified it can then be sequestered.

A number of methods have been proposed for carbon sequestration from adsorption to solid substrates for burial, oceanic sequestration, or underground sequestration of the compressed CO_2 gas. One sequestration method injects CO_2 into low or non-producing oil wells, which has shown the added benefit of revitalizing these oil wells and increasing their oil production. This process is referred to as enhanced oil recovery (EOR), and provides a practical use for the sequestered CO_2 (Kovscek and Cakici 2005) (Aycaguer, Lev-On and Winer 2001). However, before any sequestration process is undertaken, the CO_2 stream must be bone dry. This requirement is necessary to prevent corrosion in piping and equipment from carbonic acid formation and to prevent hydrate formation at the high pressures necessary for sequestration. There are two main separations to creating this gas stream: concentrating CO_2 from the other components, and then

drying it. Different methods for selectively removing CO_2 from the other flue gas components have been proposed for carbon capture.

1.1.3 Liquid Amine Scrubbers

Conventionally, to remove an acid gas such as CO_2 from a gas stream, an amine scrubber would be used. Amine scrubbers use a fluid that chemically binds CO_2 to the solvent which lends the process a very high selectivity toward CO_2 over other components in the flue gas stream. Figure 1-2 shows a process flow diagram for an amine scrubber. Flue gas is compressed and run through an absorber column, with amine solution misting counter currently, absorbing the CO_2 from the flue gas. The CO_2-rich amine solution is then pumped through a heat exchanger to the desorber column. Here the amine solution is heated to 100°C to 120°C using a reboiler or direct steam heating (Nielsen and Kohl 1997). At this temperature the CO_2 will desorb from the amine and move to the

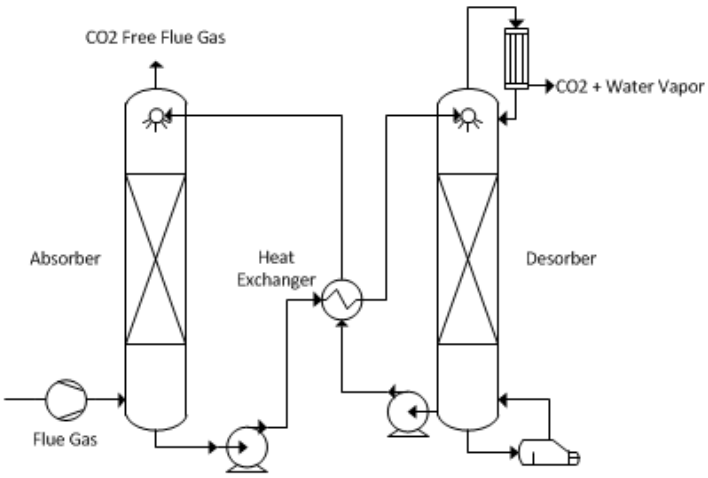

Figure 1-2. Process flow diagram of an amine scrubber with a reboiler

top of the column, saturated with water vapor. The condenser drops out the majority of the water vapor, but the CO_2 stream leaving the desorber is saturated with water at its exit temperature and will require subsequent drying prior to compression. The lean amine solution is then recirculated back to the adsorber column, with heat being recovered to the rich amine stream via the heat exchanger. Alkanolamines are typically used in amine scrubbers, with monoethanolamine (MEA) being the most common, although diethanolamine (DEA) or methyldiethanolamine (MDEA) may also be used, alone or in combination (Nielsen and Kohl 1997). Amines react with CO_2 via the following mechanisms (Nielsen and Kohl 1997)

$$H_2O \leftrightarrow H^+ + OH^-$$

$$CO_2 + H_2O \leftrightarrow HCO_3{}^- + H^+$$

$$RNH_2 + H^+ \leftrightarrow RNH_3{}^+$$

$$RNH_2 + CO_2 \leftrightarrow RNHCOO^- + H^+$$

For MEA, the heat of reaction with CO_2 is approximately 85 kJ/mol (Nielsen and Kohl 1997). Amine solutions have the benefit of having a high capacity for CO_2 even at low gas stream pressures.

There are issues with amine scrubbing systems that make it attractive to find alternative separation technologies. Acid gas saturated amine solutions are corrosive to carbon steel, necessitating the use of more expensive stainless steel equipment and piping in the process. Regeneration of the amine solution results in some volatilization of amines, releasing them to the atmosphere over time. Regeneration also causes thermal degradation of the amines over time, so to

maintain the concentration of the solution new amines must be added over time. These factors combined with the cost and complexity of amine scrubbers makes them an imperfect solution for PCC, despite amine scrubbing being a well-developed technology.

1.1.4 Physical Solvent Processes

Another method of separating CO_2 from a flue gas stream is the use of an organic solvent/solution which will selectively absorb CO_2. The solvents utilized in these processes include methanol, propylene carbonate, and ethers of polyethylene glycol, among others (Nielsen and Kohl 1997). These processes operate best at high gas stream pressures, allowing for the maximum amount of CO_2 per unit volume of solvent to be absorbed. Similar to amine scrubbers, physical absorbent separation units use an absorption and a regeneration column. Figure 1-3 shows three different regeneration methods may be used to remove the CO_2 from the solvent solution: flash regeneration, inert gas stripping, or thermal regeneration (Nielsen and Kohl 1997).

However because organic physical absorbents exhibit their highest capacity at elevated pressures, there will be a large compression cost associated with using them for capturing CO_2 from low pressure flue gas streams. The carbonated solvents are likewise quite acidic and so carry many of the same materials requirements found in the amine systems.

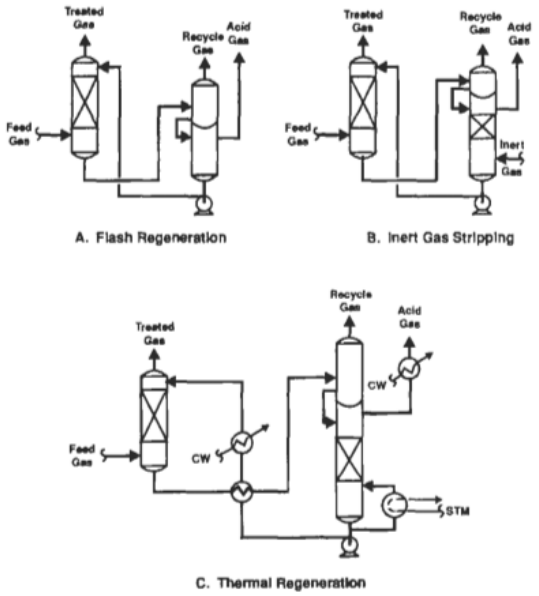

Figure 1-3. Simplified process flow diagrams for solvent absorption processes showing basic regeneration methods (Nielsen and Kohl 1997)

1.1.5 Packed Bed Adsorption

The idea of using a solid adsorbent for separating CO_2 from a flue gas stream has grown in recent years. These adsorbents materials include zeolites (Arean and Delgado 2010) (Liu, et al. 2011) (Wang and LeVan 2009) (Zhao, et al. 2007) (Zukal, Mayerova and Kubu 2010), metal oxides (Baltusaitis, et al. 2011) (Chang, et al. 2011) (Grasa and Abanades 2006) (Lu, et al. 2009) (Ramis, Busca and Lorenzelli 1991) (Wang, et al. 2011), and activated carbons, all of which exhibit a high adsorption capacity for CO_2. These adsorbents would be operated in a packed bed configuration using either a pressure swing adsorption (PSA) or a thermal swing adsorption (TSA) cycle. In both cases the CO_2 would be the preferentially adsorbed component and would be concentrated on the solid rather than in the gas stream. Figure 1-4 shows a process flow diagram of a two bed

PSA unit. The feed gas is compressed and flows in the bottom of the first bed. Once the first bed has reached saturation, the feed gas flow is changed to the second bed. The first bed is then vented, lowering the pressure in the bed, desorbing the adsorbed species. This cycle is continued as each bed is saturated. Both types of packed bed system have the benefit of using simple, relatively inexpensive controls, equipment, and vessels. The recovery of N_2 from air using molecular sieves is an example of a PSA process that recovers the adsorbed gas in high purity.

In a TSA cycle, CO_2 is adsorbed at temperatures approaching ambient and then the adsorbent is heated to desorb the gas concentrated on the solid. Figure 1-5 shows a process flow diagram for a TSA process for the drying of natural gas

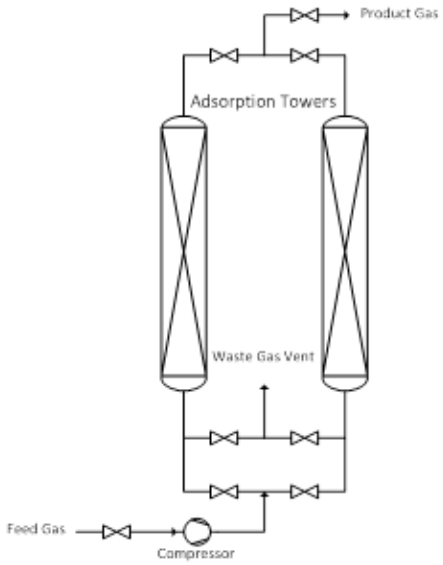

Figure 1-4. Process flow diagram of a two bed PSA

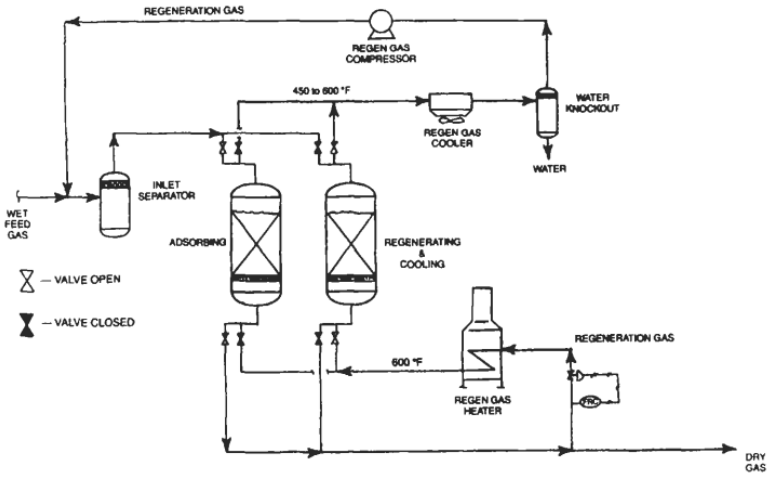

Figure 1-5. Process flow diagram of zeolite TSA system for natural gas drying (Nielsen & Kohl, 1997)

with zeolites. The process is similar to that of the PSA unit, except that the adsorbent be is heated instead of depressurized to initiate desorption.

A PSA or TSA system may use zeolite molecular sieves, activated carbon, or a range of desiccants depending on the target separation. Each adsorbent for CO_2 removal from flue gas has different strengths and sensitivities, but all are affected by moisture in the flue gas stream. Zeolite molecular sieves will progressively be deactivated by any measurable amount of moisture over time. Metal oxides are also effective desiccants and are selective for water over CO_2. Activated carbons would be ideal to remove CO_2 from air but suffer from capillary condensation when the relative humidity of a gas stream exceeds 40%-50% at which point the pore spaces fill with water. Thus to use these adsorbents, a flue gas stream would need to be dried prior to CO_2 adsorption.

1.1.6 Solid-Supported Amines

Solid amine sorbents are a class of materials that have been developed, combining the chemical specificity and water tolerance of a liquid amine system with the ease of handling offered by a solid adsorbent in a packed bed system. These sorbents would be regenerated thermally, similar to bulk amine solutions, and as such would be used in a TSA process.

One method of producing a solid amine sorbent is to pair a chemically stable micro or mesoporous solid adsorbent with an amine matched to the steric considerations and pore volume of the adsorbent. The amine remains present in the porous support due to the adsorptive force within the pores, which reduces the amine's vapor pressure compared to that of the liquid amine. While the vapor pressure of the amine is lower when adsorbed than in the bulk liquid, it is still finite, and amine vapor may leach into the regeneration stripping stream. Jadhav et. al (2007) reported CO_2 adsorption capacities of up to 17.5 mL/g at 30°C and 14 mL/g at 120°C on zeolite 13X loaded with 18.7 wt% MEA. Other work exploring amine impregnation of zeolite 13X obtained breakthrough CO_2 adsorption capacities of 19.98 mg/g MEA impregnated 13X and 22.78 mg/g for isopropanol amine impregnation (Chatti, et al. 2009). Some of the highest CO_2 adsorption capacities have been reported on amine impregnated hexagonal mesoporous silica (HMS). Chen et. al (2010) reported a CO_2 adsorption capacity of 184 mg/g with 60 wt% loading of polyethylenimine (PEI) on HMS.

Another method for immobilizing an amine is to chemically graft the amine functionality to the surface of a solid. Using this method, the possibility of vapor

loss is eliminated by covalently bonding the organic chain to the surface of the material. Conventional amine fluids used in liquid amine scrubbers such as MEA and DEA lack the chemical functionality necessary for grafting them to the surface of a solid. However, alkoxy and halogen-terminated aminosilane molecules have both a chemical function which will bond to the surface of a substrate and the amine functionality required for interaction with CO_2. Previous work has identified chemically stable, siliceous materials such as SBA-15 and silica gel as substrates for the tethers (Chang, et al. 2009) (Hiyoshi, Yogo and Yashima 2005) (Knofel, et al. 2007) (Ko, Shin and Choi 2011) (Sayari and Harlick 2010) (Zhao, Shen and Bai 2012). Such amorphous metal oxides are well-suited for chemical grafting as, unlike crystalline materials, all of the surface-exposed atoms terminate in hydroxyl groups. This allows a high density of tethers to be exposed along the pore walls. To date, all previous materials studied have been porous substrates due to the enhanced surface area and tether loading that comes with such materials. A risk lies with porous materials, however, because pore systems can concentrate non-target gases and vapours. This characteristic makes porous materials prone process upset when exposed to very high humidity, mist, or a slug of liquid that moves through the system.

1.2 Carbon Dioxide Drying

There are two processes typically used for gas drying: glycol water absorption and packed bed desiccant drying. Glycol water absorption is typically used when a dewpoint above -40°C is acceptable and flow rates are relatively high. Packed bed TSA or PSA drying units are used if dewpoints lower than -40°C are needed or when relatively low flow rates makes glycol absorption driers impractical.

1.2.1 Issues with Wet CO_2

An issue that has not seen any reported exploration is how to remove water vapor from the CO_2 gas stream. The presence of water in the CO_2 stream causes two distinct problems. The first is the formation of carbonic acid when the water vapor combines with the CO_2 through the reaction shown here

$$CO_2 + H_2O \leftrightarrow H_2CO_3$$

This carbonic acid will corrode process equipment and piping. The second problem is that at the high pressures required for pipeline distribution or for deep-well injection it is possible for carbon dioxide hydrates to form. In order to prevent these issues, a CO_2 gas stream would be dried to below 10 parts per million on a volume basis (ppmv) humidity.

1.2.2 Gas Humidity

There are several different measurements of humidity in a gas stream. The three most commonly used are ppmv, relative humidity, and dew point. Relative humidity measures moisture as a percentage of the total possible moisture that a gas at that temperature could support and is described by the equation

$$\phi = \frac{e_w}{e^*_w} \times 100\%$$

where ϕ is the relative humidy, e_w is the partial pressure of water vapor, and e^*_w is the saturated vapor pressure of water at a given temperature. e^*_w itself is described by the Goff Gratch equation (Goff 1957)

$$\log_{10} e^*_w = -7.90298\left(\frac{373.16}{T} - 1\right) + 5.02808\log_{10}\left(\frac{373.16}{T}\right) - 1.3816 \times 10^{-7}\left(10^{11.344\left(1-\frac{T}{373.16}\right)} - 1\right) + 8.1328 \times 10^{-3}\left(10^{-3.49149\left(\frac{373.16}{T}-1\right)} - 1\right) + \log_{10}(1013.246)$$

where e^*_w is in hPa and T is temperature in K. The Goff Gratch equation is considered to be the reference equation for calculating the saturated vapor pressure over water.

Dew point references moisture content by reporting the temperature at which the moisture content of the gas would condense. In other words, it describes the temperature at which the partial pressure of water vapor e_w is the saturated vapor pressure or

$$e_w = e^*_w(T_{dp})$$

where T_{dp} is the dewpoint.

The partial pressure of water vapor e_w can be converted to gas water content in ppmv by the following relation

$$H_{ppmv} = \frac{e_w}{P} \times 10^6$$

where P is the total system pressure in hPa and H_{ppmv} is the humidity in ppmv.

Dewpoint and ppmv are both absolute measures of the absolute amount of moisture in a gas stream and are useful for comparing the humidities of gas

streams at different temperatures. Relative is an effective measure of the amount of humidity in a gas stream with respect to the maximum amount possible.

1.2.3 Glycol Drying

Glycol drying is a widely used gas dehydration process for drying natural gas and air. Figure 1-6 shows a simplified process flow diagram of a typical glycol dehydration plant. Feed gas enters the absorption section of the of the glycol contactor where moisture is absorbed by glycol fluid flowing down through the column. The dried gas is used to cool the glycol fluid using a heat exchanger, and then any entrained glycol droplets are scrubbed out. The moisture-rich glycol is then flashed to remove any absorbed hydrocarbons and is heated by several heat exchangers and eventually enters a glycol reconcentration column where water is boiled off. A condenser is used to limit the glycol losses in the reconcentration column. This condenser is cooled using the rich glycol stream prior to it entering the reconcentration column. The hot lean glycol from the reconcentrator is then moved to a surge tank and circulated through heat exchangers on its way back to the absorption contactor. The standard glycol used for drying natural gas is triethylene glycol (TEG), however other glycols including diethylene glycol (DEG), tetraethylene glycol (T_4EG) or other fluids such as methanol or glycerol may be utilized for niche applications (Nielsen and Kohl 1997).

Despite their effective use for drying natural gas, glycol drying is not ideal for drying CO_2. Conventional glycol drying systems are inefficient for drying gases

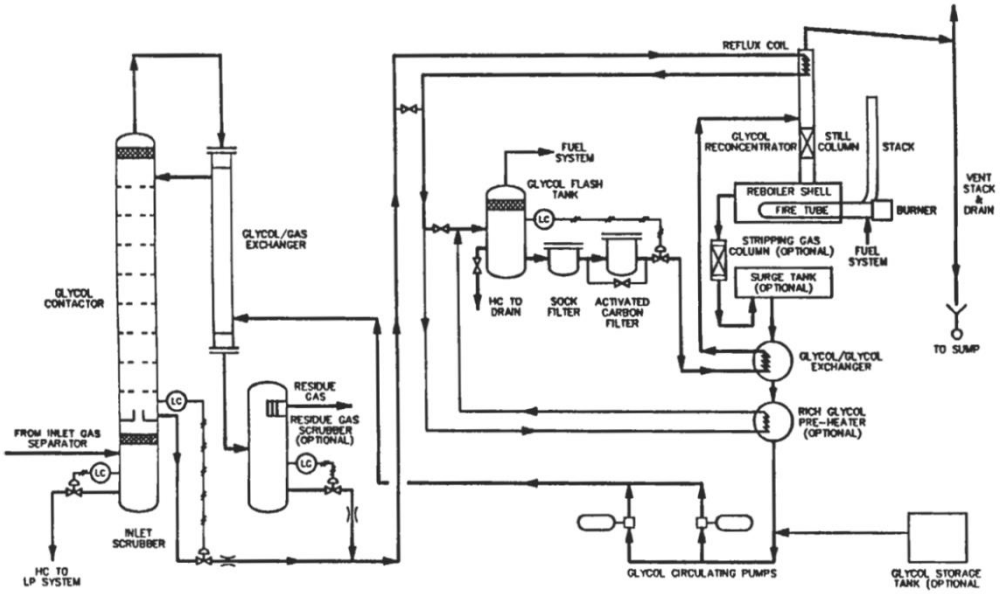

Figure 1-6. Simplified process flow diagram of a typical glycol dehydration process (Bentley 1991)

to dewpoints below -40°C. Glycols also have significant absorption capacities for CO_2 at elevated pressures (Jou, et al. 1987). The absorbed CO_2 works effectively as a purge to remove water from the glycol but this loss results in a significant reduction in the amount of CO_2 recovered from the drying process.

1.2.4 Packed Bed Drying

Packed bed TSA or PSA drying systems must be selective for moisture over CO_2 so that the CO_2 is produced as the product. Materials often used as desiccants in a packed bed configuration include silica gel, activated alumina, or zeolite molecular sieves. Figure 1-7 shows the equilibrium water capacity of these adsorbents as a function of relative humidity at 25°C. Silica gel has a higher water adsorption capacity at high humidity but little capacity at low humidity which is limiting for generating low dewpoint product gas. Alumina adsorbents

are used most commonly in PSA cycles for heatless air drying and, though the isotherms do no suggest it, are capable of generating gas having a lower dewpoint compared to the same process using silica gel. Zeolite molecular sieves exhibit an exceptionally high capacity for water at very low concentrations which precludes them from being used in a PSA cycle for bulk moisture removal and requires the adsorbent, in a TSA cycle, to be heated to temperatures in excess of 200°C to be regenerated.

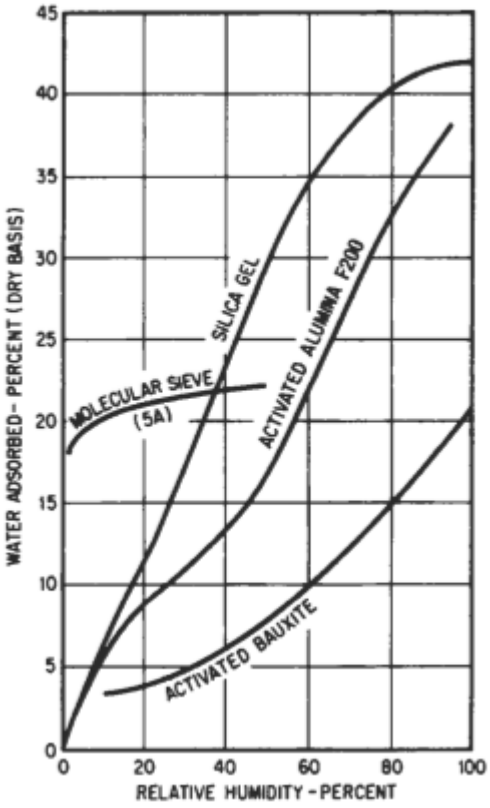

Figure 1-7. Equilibrium water adsorption capacities of several desiccants at 25°C as a function of relative humidity (Nielsen and Kohl 1997)

1.3 Relevant Adsorbents

1.3.1 Zeolites

Etymologically the word zeolite originates from the Greek words ζειν meaning "to boil" and λιθος meaning "stone" (Breck 1974). This name originates from naturally occurring zeolites being heated and a characteristic frothing being seen as water rapidly desorbed. In more conventional terms zeolites are crystalline inorganic materials with elemental compositions similar to quartz or feldspar minerals, but with a much more open, three dimensionally porous structure. In fact, zeolites have uniform 3-10 Å pores, capable of completely excluding molecules larger than their diameter, a process referred to as molecular sieving. The zeolite crystal structure is formed from tetrahedrally coordinated aluminum and silicon oxide units. The inclusion of aluminum in the framework gives it a net negative charge, which is balanced by the inclusion of charge-balancing cations (Breck 1974). These cations may be exchanged to modify the properties of the zeolites. Zeolitic materials have a number of industrial uses as ion exchangers, catalysts, and as adsorbents. Their adsorptive separations are based on two principles: molecular exclusion based on molecule size or separation based on the selectivity of the surface for polarizable molecules. More than 200 types of zeolite frameworks have thus far been identified and synthesized with up to 1000 theoretically possible (Breck 1974).

1.3.2 Silica Gel

Silica gel can be described as having the formula $SiO_2 \cdot nH_2O$. It is produced by reacting aqueous sodium silicate with sulphuric acid, which forms a hydrogel. The gel is then washed to remove the sodium sulphate, dried, and crushed and sieved to size. Depending on the synthesis conditions, the pore size and surface area of the silica gel material can be somewhat controlled, although the absolute pore size and pore size distribution is much greater than crystalline materials such as zeolites.

Each exterior surface atom of silica gel, and other similar highly siliceous materials, such as SBA-15, should terminate in a hydroxyl group. The number of these groups can be increased by adjusting the pH of a solution containing silica gel. These hydroxyl groups make siliceous materials ideal candidates for aminosilane grafting, as the chemistry of reacting the alkoxysilane requires the surface to be hydroxylated.

1.3.3 Engelhard Titanosilicate 2

Engelhard Titanosilicate 2 (ETS-2) first described in a 1989 patent (Kuznicki 1989) is actually somewhat misnamed. It is actually a form of sodium titanate which through the addition silica to the synthesis hydrogel, forms nanometer sized particles whose surfaces are covered in sodium titanate, an effective ion-exchanger. The small size of these nano-titanate particles gives them a high surface area (~300 m^2/g) with no porosity, meaning that these adsorbents will resist fouling conditions capable of deactivating porous materials. The surface of

ETS-2 also contains a high concentration of free hydroxyl groups, making ETS-2 an attractive support for aminosilane grafting as the lack of porosity places no limitations on the size of amine tethers which can be grafted, whereas porous substrates are limited by steric considerations.

1.3.4 Engelhard Titanosilicate 10

Engelhard Titanosilicate 10 (ETS-10) is a mixed octahedral/tetrahedral titanium silicate composed of titanium oxide octahedra and silicon oxide tetrahedra forming a three dimensional network of interconnected channels. Patented in 1989, ETS-10 is a synthetic form of the mineral zorite (Kuznicki 1989). Its chemical structure can be described by the oxide mole ratios:

$$1.0 \pm 0.25\ \mathrm{M}_{2/n}\mathrm{O} : \mathrm{TiO}_2 : y\ \mathrm{SiO}_2 : z\ \mathrm{H}_2\mathrm{O}$$

Where M is one or more cation having valence *n*, *y* ranges from 1.0 to 10.0, and *z* from 0 to 100. The preferred case has M being a mixture of alkali metal cations, and *y* is in the range from 2.5 to 5 (Kuznicki 1989). The framework is shown in Figure 1-8. This structure leads to ETS-10 have some unique properties. The arrangement of titanium atoms in the framework forms a quantum wire, which has been subject of recent investigation (Jeong, Lee, et al. 2009) (Jeong, Lim, et al. 2011) (Luca, et al. 2006) (Yilmaz, Warzywoda and Sacco 2006).

ETS-10 has also been investigated as an adsorbent for separating light

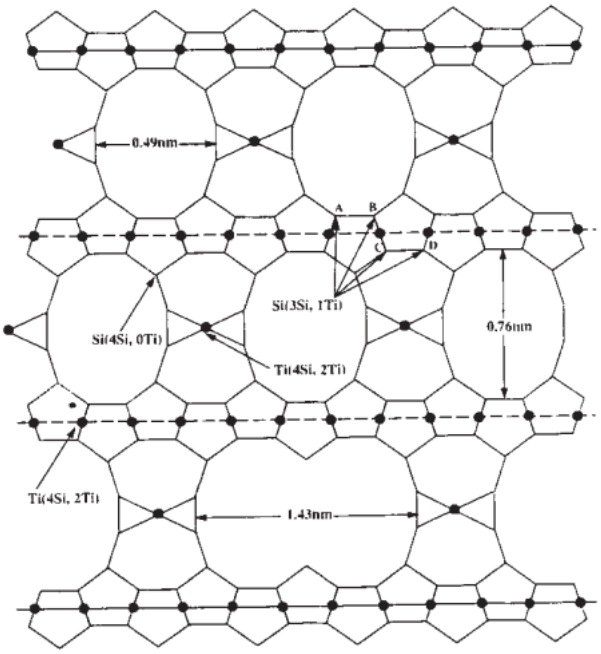

Figure 1-8. Framework structure of ETS-10 (Anderson, et al. 1994)

hydrocarbons (Anson, et al. 2008) (Avila, et al. 2011) (Al-Baghli and Loughlin 2006) (Shi, Lin, et al. 2010), as an adsorbent for noble gases (Anson, et al. 2008) (Kuznicki, et al. 2007), and as a desiccant (Kuznicki, Thrush and Garfinkel 1993). Some of these unique adsorption properties can be attributed to the fact that the pore walls of ETS-10 are composed entirely of silica and so offer adsorption properties that are a hybrid of silica and zeolite adsorption behaviors. Unlike amorphous silica gel, ETS-10 has a discrete, nanoscale, pore size which amplifies its adsorption characteristics compared to silica gel while maintaining the chemically passive surface silica gel is valued for. Being a crystalline molecular sieve, the atoms lining the pore walls do not terminate in hydroxyl groups and so ETS-10 is more suitable as a vessel for an amine fluid rather than

a support for grafted amines. Water adsorption isotherms for Ca-ETS-10 exhibiting this hybrid water adsorption behavior are shown as Figure 1-9.

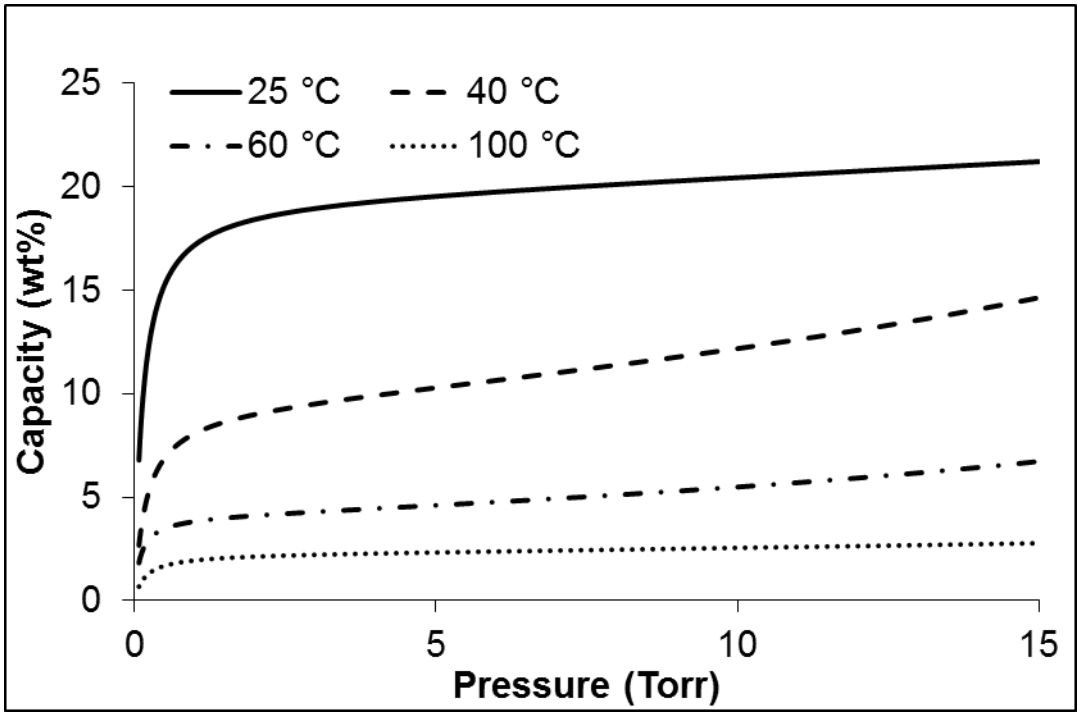

Figure 1-9. Ca-ETS-10 water adsorption isotherms

1.4 Project Objectives

Two separations are necessary for PCC of CO_2: the CO_2 from a flue gas stream must first be concentrated and the concentrated stream of CO_2 must be rigorously dried so that it can be compressed. To date no studies have been published that explore the use titanates as substrates for amine grafting. Furthermore, the process considerations and efficiency of drying a CO_2 stream have not been addressed in literature as perhaps the capture of CO_2 has long been seen as a tougher target.

ETS-2 was chosen as a support for direct CO_2 adsorption as this material has unique properties that make it a compelling substrate for grafted amines. Amine grafted ETS-2 is the first example, to date, of a non-porous material studied for such an application. ETS-10 was used in this study as a desiccant for CO_2 drying. The manner in which the moisture capacity decays with temperature makes ETS-10 particularly suited toward low-thermal-input CO_2 drying.

2. Experimental

2.1 Material Characterization

2.1.1 Powder X-Ray Diffraction

X-ray diffraction (XRD) was used to verify the identities of and to gain qualitative information about the purities and crystal structures of the adsorbents used in this study. XRD is an efficient method for identifying crystal phases in a powder sample and is able to match the phases of the sample and any impurities present against a database of patterns. Changes in the XRD pattern after treating an adsorbent, such as during ion exchange, can give information about changes to the adsorbent structure, such as changes in pore size or loss of crystallinity. A Rigaku Ultima IV with Co tube (38kV, 38mA) with an average Kα wavelength of 1.7902 Å equipped with a D/Tex detector with a Fe filter was used for all XRD characterisation. XRD patterns obtained were compared to data from the International Center for Diffraction Data-Powder Diffraction File (ICDD-PDF) using JADE 9.1, along with visual comparisons to existing standards and literature to verify sample identity and purity. All measurements were taken at room temperature on finely ground powder samples.

2.1.2 Scanning Electron Microscopy

To examine the size and morphology of the adsorbent crystals scanning electron micrographs were taken at several different levels of magnification. These micrographs have appearance similar to a traditional optical microscope image

but at much higher levels of magnification. For this study a Zeiss EVO MA 15 SEM with a LaB6 crystal source was used to generate the electron beam for the SEM analysis. The electron beam voltage was set to 5.0kV and the system optimized for magnification up to 10,000X. The adsorbent samples were ground to a fine powder and placed on a standard SEM stub for imaging.

2.1.3 Energy Dispersive X-ray Spectroscopy

Typically performed simultaneously with SEM or TEM, energy dispersive X-ray spectroscopy (EDX) is an analytical technique that measures the surface elemental composition of a sample (depth of ~10 μm). It is typically performed along with SEM or TEM since the electron beam which bombards the sample causes characteristic X-ray emissions. These quantized emissions are unique for every chemical element, allowing them to be identified, with the exception of the three lightest elements (H, He, and Li) which lack the necessary electrons to emit characteristic X-rays. This technique was used in this study to determine the extent of ion exchange and was performed, along with the capture of SEM micrographs, using the EDX detectors attached to the instrument.

2.1.4 Gas Adsorption

In this study gas adsorption isotherms were measured using the manometric adsorption method. In such an experiment the sample chamber, reservoir and manifold are first evacuated using vacuum. The probe gas is then taken into the manifold reservoir and the pressure is monitored. The valve separating the

sample chamber from the reservoir is then opened; allowing the probe gas to move into the previously evacuated sample chamber. The pressure is monitored as the gas expands and adsorption takes place. The final stable pressure of the combined volume is the equilibrium adsorption pressure. The volume of gas adsorbed can be determined by factoring out the decrease in pressure due to expansion into the void volumes. The dead space is measured using the same procedure except that the probe gas is a nonadsorbing species such as helium.

CO_2 isotherms were collected on a Micromeritics ASAP 2020C surface area and porosity analyzer. Isotherms were collected using the chemisorption function and the sample furnace. Samples (~ 250 mg) were packed into quartz u-tubes containing a 1 cm plug of quartz wool in the bottom. Samples were activated in-situ under a flow of N_2 (~ 200 ml/min) using a ramp rate of 10 °/min and were held under flow at 200°C for 15 minutes. The N_2 flow was then stopped and the sample evacuated for 60 minutes at 200°C. Samples were cooled, under vacuum, to their analysis temperature and isotherms were collected in fixed dosing mode with an equilibration delay of 5 seconds. Some replicate experiments were carried and it was found that the adsorption capacities were fully reproducible which suggests that the tethers are entirely stable at 200°C under hard vacuum.

2.1.5 Surface Area Calculations

The surface area of the adsorbents was measured using an ASAP 2020C surface area and porosity analyzer from Micrometrics. Typically nitrogen gas is utilized for surface area analysis due to its low cost and availability. However nitrogen is

known to have a quadropole moment that can interact with the framework of zeolites. It has been observed that nitrogen isotherms for zeolites may not be able to clearly distinguish between materials with distinctly different sized pores. This interaction may also cause pore size distributions and surface areas calculated from adsorption data to be skewed. In order to avoid this gas retention problem argon was used as the probe gas for measuring the surface area of zeolite 4A and ETS-10. Based on the argon adsorption isotherms, the surface area was calculated using the Langmuir method.

2.1.6 Bulk Density Measurement

In order to compare the adsorption capacity per unit volume of the various adsorbents used, their bulk densities were measured to compare the volumetric efficiency of the various adsorbents. First, an empty 3.7 mL glass vial was selected. Adsorbent pellet samples previously dried overnight in an oven at 80°C were removed from the oven and the pellet samples were immediately poured to fill the vial. The vial was tapped lightly to allow the pellets to settle and the vial was topped off with more pellets. After repeating the tap and fill process three times, the filled vial was weighed using a Denver Instruments analytical balance with a 0.1 mg sensitivity. The pellets were then poured out and the vial blown clean with building compressed air. This process was repeated three times and the average weight was taken. The volume of the vial was then measured by filling the vial with distilled water and measuring the weight change between the full and empty vial. Using a water density of 1g/mL, the volume of the vial was

calculated and this volume was then used in combination with the adsorbent sample weight to calculate the adsorbent bulk density.

2.1.7 Thermogravimetric Mass Spectroscopy (TG-MS)

The TG-MS plots were collected using a TA Instruments Q500 TGA coupled to a Pfeiffer Omnistar GSD 320 residual gas analyzer. TG scans were run using a balance purge rate of 40 ml/min and a sample purge rate of 150 ml/min. The sample purge gas was selected from N_2 or dry, compressed air depending on the sequence being run. Samples were loaded on platinum pans and heated at a rate of 10 °/min from ambient to 600°C.

The mass spectrometer was configured with a steel capillary heated to 200°C and connected to the TGA by means of a stainless steel adapter and a ¼" branch T-fitting. The capillary was positioned at the center of the tee close to the furnace exhaust to sample the evolved gases. The exhaust end of the T-fitting was connected to a 6 m length of ¼" OD tubing that prevented back-diffusion of atmospheric components and lead to a fumehood exhaust. Experiments were run in MID mode with fragments at m/z=12, 15, 16, 17, 18, and 44 tracked over time. These fragments were found to be the most diagnostic signals associated with the decomposition of the tethers. To start data collection, the two instruments were manually synchronized and an uncertainty of a few tenths of a degree for the starting temperature can be expected between the TG and MS plots.

2.1.8 Adsorption/Desorption Cycles

Adsorption/desorption cycles were collected by sequencing a series of activation and adsorption steps. The same TA Instruments Q500 instrumentation was used as for the TG-MS experiments. To achieve equal volumetric flow rates for N_2 and CO_2 the TG instrument setpoints were determined using an Agilent ADM 1000 volumetric flow meter connected to the exhaust of the furnace. This step was necessary as the TG instruments flow controllers were not calibrated for CO_2 and if the same setpoint was used for both gases then the measured flows differed substantially. Careful matching of the flow rates is important because a large difference in flow rate will change the force on the sample pan and an artificial weight change will be registered when the flow switches from one gas to another. The flow values in brackets correspond to the instrument setpoint values. Samples were equilibrated at 40°C and then heated at 20 deg/min to 150°C under N_2 (40 ml balance purge, 118 ml/min sample purge). An isothermal dwell of 20 min at 150°C was followed by a cooling step to 70°C. After an isothermal dwell of 5 min at 70°C, the sample purge gas was switched to CO_2 (200 ml/min) and the sample equilibrated for 20 min. The CO_2 was desorbed by switching the sample gas back to N_2 and heating the sample to 150°C under the same conditions as previous. A total of 20 of these sequences were carried out for each sample. The tuned analysis protocol was tried on a sample of ground quartz wool and it was determined that, after the flow rates were properly matched, the switching event did not cause a measurable deflection in the baseline signal.

2.2 CO_2 Adsorbent Sample Preparation

2.2.1 ETS-2 Synthesis and Amine Grafting

The ETS-2 samples used were synthesized hydrothermally using a previously published procedure (Kuznicki, 1989). 1.0 g samples of ETS-2 were combined with 28 mmol of aminosilane in a round bottomed flask. Approximately 75 mL of toluene was added and the mixture was heated under reflux using a heating mantle for six hours. Following this reflux, the samples were filtered and washed with toluene and then washed with deionized water. The samples were then dried in an oven at 80°C before being transferred to tightly capped glass vials.

Aminosilane molecules were reacted with ETS-2 samples, grafting them to the surface with a siloxane bond. The aminosilane molecules used in this study were (3-1minopropyl)trimethoxysilane (Sigma Aldrich), [3-(2-Aminoethylamino) propyl]trimethoxysilane (Sigma Aldrich), and N 1-(3-Trimethoxysilylpropyl) diethylenetriamine (Sigma Aldrich). These molecules are referred to further as N1, N2, and N3 respectively, in reference to the number of amine groups present in the molecule and the resulting grafted samples are designated N1-ETS-2, N2-ETS-2, and N3-5TS-3 respectively.

2.3 CO_2 Drying Sample Preparation

2.3.1 Material Sources

The silica gel used in this study was Grace Davison Grade 40 silica gel (lot #908) which arrived with a particle size from 3.36 to 1.68 mm (No.6 to No.12 mesh). The zeolite 4A used was purchased from Dessican Inc. and arrived in beads with a particle size from 4 to 2 mm (No.5 to No.10 mesh). Alumina used was obtained from Sigma Aldrich as activated aluminum oxide in a ~0.104 mm (No.150 mesh) powder. ETS-10 samples were synthesized from raw materials. The synthesis procedure is outlined later in this chapter.

2.3.2 ETS-10 Synthesis and Ion Exchange

ETS-10 is synthesized in the sodium ion form as previously described and was ion exchanged to the calcium and mixed calcium/hydrogen ion forms. The calcium ion exchange was carried out by mixing the synthesized powder with a calcium chloride solution. The ion exchange mixture was prepared by adding 30 g calcium chloride dehydrate (Fisher) to 150 g of de-ionized water, stirring to dissolve the calcium chloride, then adding 15 g of ETS-10 powder. The mixture was then agitated and placed in a sealed vessel in an oven at 80°C under static conditions for four hours. After this time the powder was again washed with de-ionized and filtered using a Buchner vacuum funnel and Whatman grade 4 filter paper, and dried in an oven at 80°C.

The mixed calcium hydrogen exchange was carried out by dissolving 4 g calcium chloride in 150 g of de-ionized water and then adding 15 g of ETS-10.

The mixture was placed in an oven under static conditions at 80°C overnight in a sealed container. The next morning the sample was filtered and then dried in an oven at 80°C for two hours. The sample was then dispersed in 150 g de-ionized water. HCl (1M, Fisher) was added to the mixture until a pH of 2 was achieved. The sample was then stirred overnight at room temperature. It was then washed with deionized water and filtered using a Buchner vacuum funnel and Whatman grade 4 filter paper, and was then dried in an oven at 80°C.

2.3.3 Adsorbent Bed Preparation

The adsorbent samples for the various forms of ETS-10 and for activated alumina, which were in powder form, were pressed into binderless dense pellets. Approximately one gram of adsorbent powder was poured into a 19.05 mm stainless steel die to form each pellet. In order to ensure smooth action of the die, it was wiped down with vacuum oil using a kimwipe before each pellet was pressed. The powder was then compressed in the die using a Carver manual hydraulic press. A pressure of 16 tonnes was applied. These pellets as well as the commercially produced silica and zeolite 4A pellets were crushed separately using an agate mortar and pestle. The crushed pellets were then sieved separating the 1.19 mm to 0.595 mm (No.16 to No.30 mesh) fraction for use in the carbon dioxide drying experiments.

2.4 CO_2 Drying Experiment Apparatus and Operation

To measure the performance of the various adsorbents an experimental apparatus was designed and constructed. The test equipment needed to provide a variety of inlet moisture levels, measure <10 ppm concentrations of moisture in the presence of CO_2, and control the temperature of the bed and purge streams. A photograph of the experimental setup is included as Figure 2-1 and a process flow diagram is included as Figure 2-2. In order to control the input stream humidity, the inlet stream coming from the carbon dioxide cylinder (Praxair) was split and run through two mass flow controllers (MC, Alicat Scientific) scaled for 0 to 500 cc/min gas flows at 25°C and 101.325 kPa mass reference conditions. The flows for these and other Alicat meters were converted to flows at STP (0°C and 100 kPa). The flow from one mass flow controller (MFC) bubbled through a 300 mL liquid contactor partially filled with de-ionized water to a 50 mL accumulator, saturating it with moisture, while the second stream went directly to the accumulator. By adjusting the flowrate of the two MFCs, the dry and moisture saturated gas streams could be blended in the accumulator to achieve gas moisture contents from 0 to 100% relative humidity. The liquid contactor was only partially filled with water in order to prevent liquid water from being carried over from the liquid contactor to the downstream tubing and accumulator. Moisture blending calibration runs were carried out, with the outlet humidity from the accumulator being recorded at various blending levels using a Fisher Scientific Traceable Humidity Meter. The moisture blending calibration

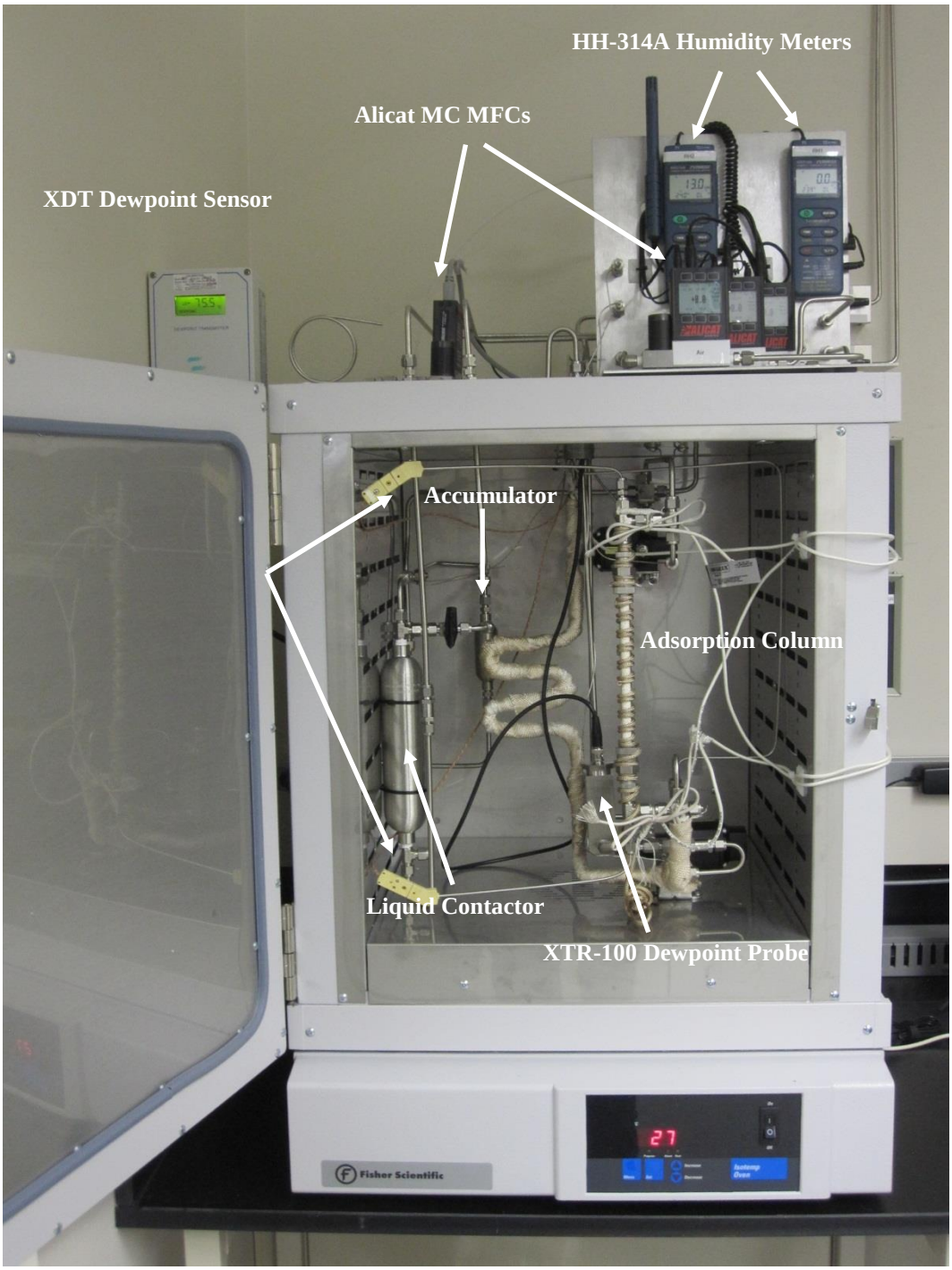

Figure 2-1. Annotated photograph of CO_2 drying experimental setup

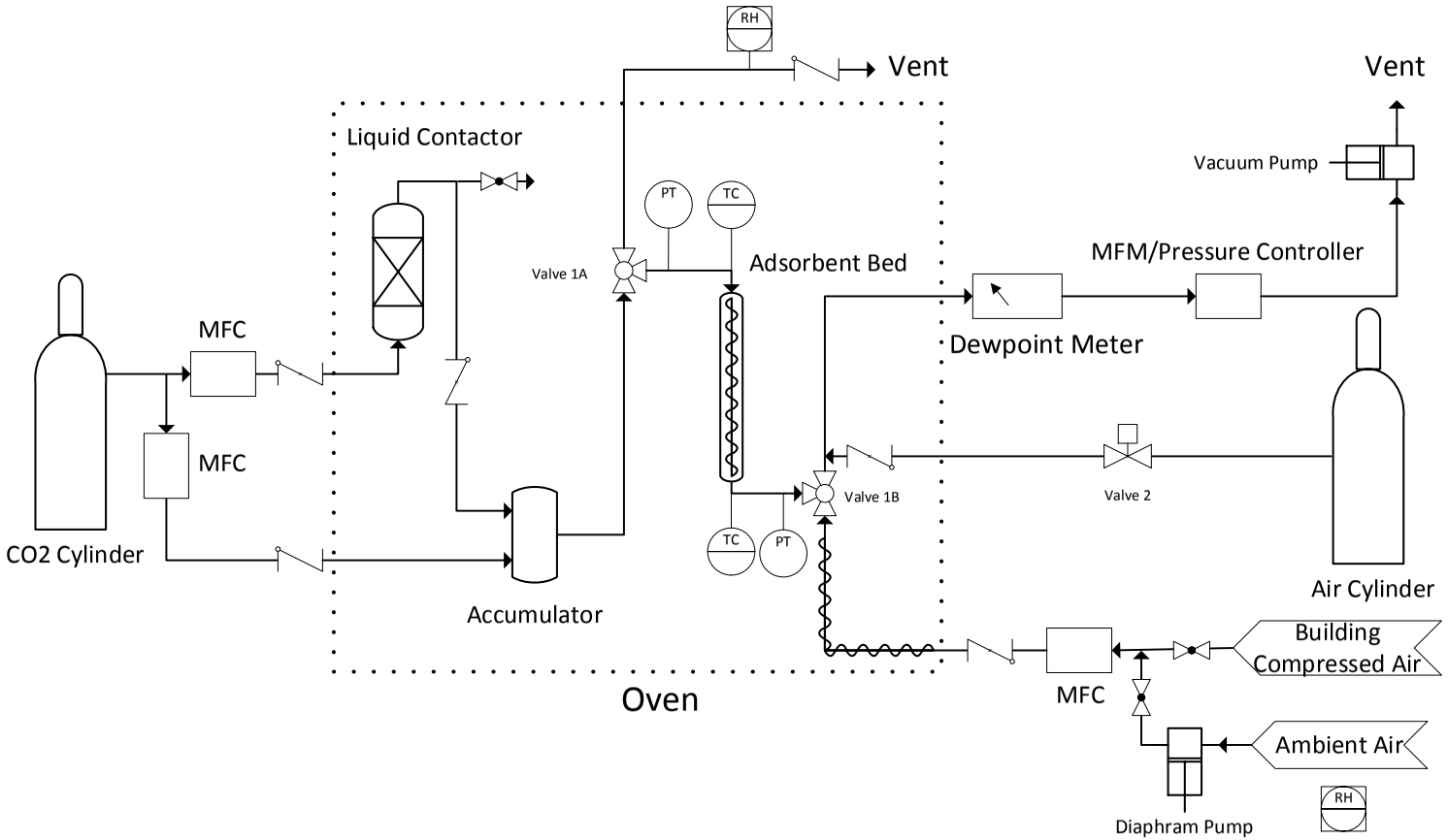

Figure 2-2. Process flow diagram of CO_2 drying experimental setup

curve is show as Figure 2-3. Though the mixing deviates from a linear trend below a wet gas fraction of 0.2 the equation

$$RH = 1.0431x - 0.0284$$

where *x* is the wet gas fraction, can be used to determine the mixed gas humidity as in all experiments the wet gas fraction was 0.5 or greater which is well within the linear range of the calibration plot.

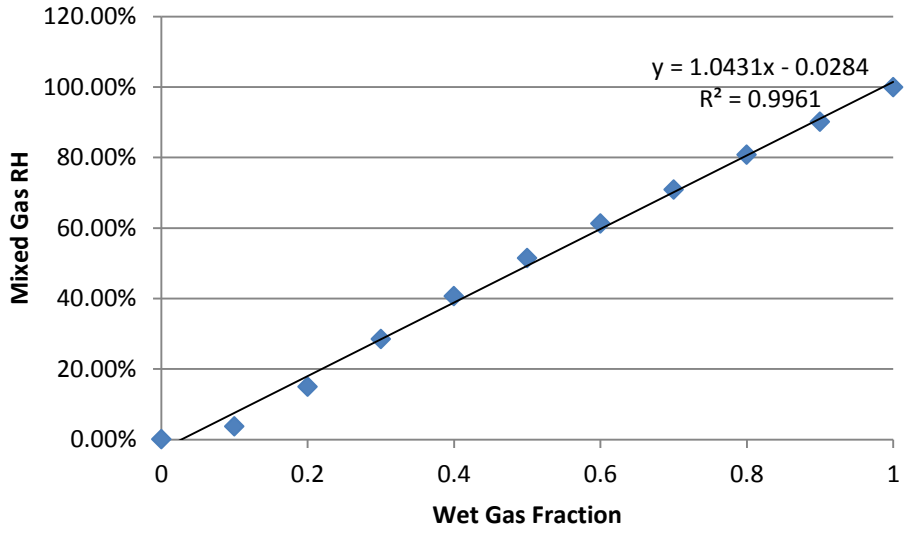

Figure 2-3. CO_2 drying experiment moisture blending calibration curve

The gas stream from the accumulator traveled to the top of the adsorbent bed and flowed down through it. The adsorbent bed itself was made of borosilicate glass with an outer diameter of 12.7 mm. A bed packed with zeolite 4A pellets is shown as Figure 2-4. The adsorbent was packed into the bed and kept in place by plugs of ~ 2 g of glass wool packed at both ends of the bed. The pressure at the inlet and exit of the bed is monitored by a pair of PX209 0-15 psia pressure transducers (Omega Environmental). The temperature at the inlet and exit of the

Figure 2-4. Sample adsorbent bed packed with zeolite 4A pellets

bed are also measured using two HGKMQSS K-type thermocouples with ungrounded probes (Omega Environmental). In order to maintain a stable temperature for humidification and to prevent condensation all equipment in contact with moist CO_2 was kept inside a Fisher Isotemp oven maintained at 30°C.

The outlet of the desiccant bed is plumbed to a high sensitivity dewpoint meter, which assessed the amount of moisture remaining in the gas stream. The sensor used was a COSA Xentaur XDT transmitter with a high capacitance Al_2O_3 XTR-100 sensor element capable of measuring dewpoints from -100°C to 20°C (0.013 ppmv to 23080 ppmv).

The product flow rate was measured by an Alicat Scientific MC mass flow/backpressure controller. This instrument allows the column to be maintained at atmospheric pressure while simultaneously recording the product flow rate. Downstream of this pressure controller a vacuum pump can be used to create a pressure differential for smoother operation of the backpressure controller though this was not typically required.

To regenerate the bed the three-way valves around the bed are actuated, shifting the system from adsorption to desorption mode. Another Alicat Scientific MC MFC (0-500 sccm) was used to control the flow of regeneration air. Either building-supplied compressed air or ambient air (compressed and delivered via a diaphragm pump (KNF Neuberger)) was selected as the regeneration air. The ambient air humidity was measured by a HH-314A portable temperature/humidity meter (Omega Environmental).

The regeneration air source was controlled by a three-way valve. The regeneration air flowed from the MFC to the bottom of the adsorbent bed flowing counter current to the wet gas stream in the adsorption phase. While flowing to the bed the regeneration air was heated to 70°C by a HTC-120 heating cord (Omega Environmental) wrapped around the tubing and a HTC-030 heating cord (Omega Environmental) wrapped around the adsorbent bed. The regeneration air swept through the adsorbent bed and then past another HH-314A portable temperature/humidity meter (Omega Environmental) and was then vented to the room.

After the regeneration the bed was allowed to cool. During this time the dewpoint sensor was blown down with dry nitrogen supplied from a cylinder to remove moisture that had adsorbed. After the bed had cooled and the dewpoint sensor level had been reduced to below -65°C another adsorption cycle could be run. Figures 2-5, 2-6, and 2-7 show the gas flow profiles for the adsorption, desorption, and cool-down phases of cycle operation respectively.

The entire experiment was controlled and data collected through a Labview program written by Les Dean from the Department of Chemical and Materials Engineering instrument shop. Analog signals were collected through an Opto 22 SNAP-DAC-EB2 data acquisition panel and brought to the Labview program via an Ethernet cable. RS-232 digital signals from the HH-314A

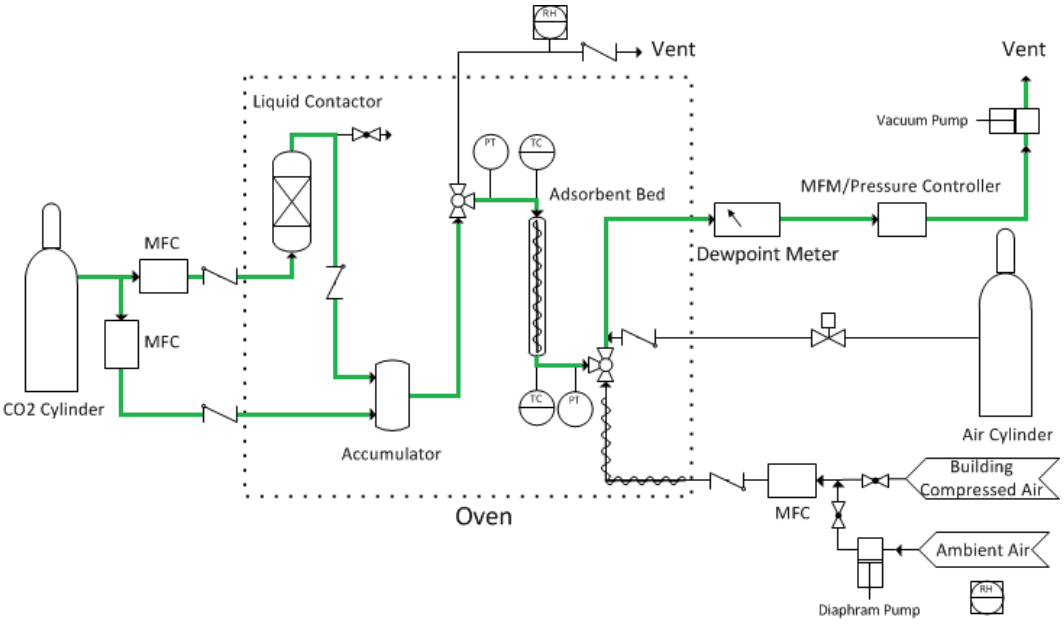

Figure 2-5. Gas flow path during adsorption phase of CO_2 drying experiment

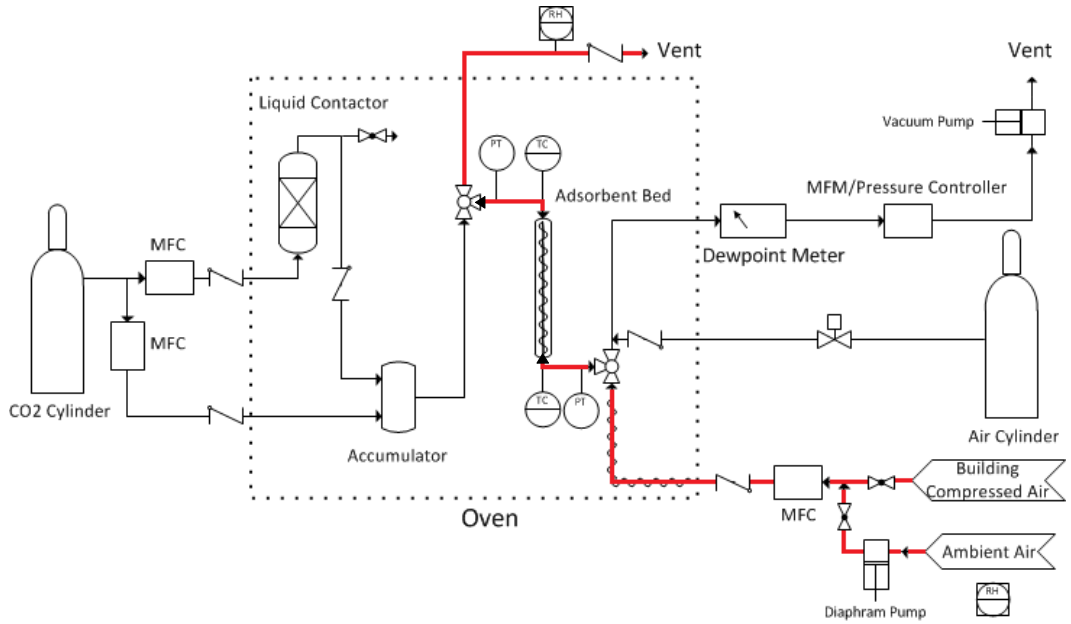

Figure 2-6. Gas flow path during desorption phase of CO_2 drying experiment

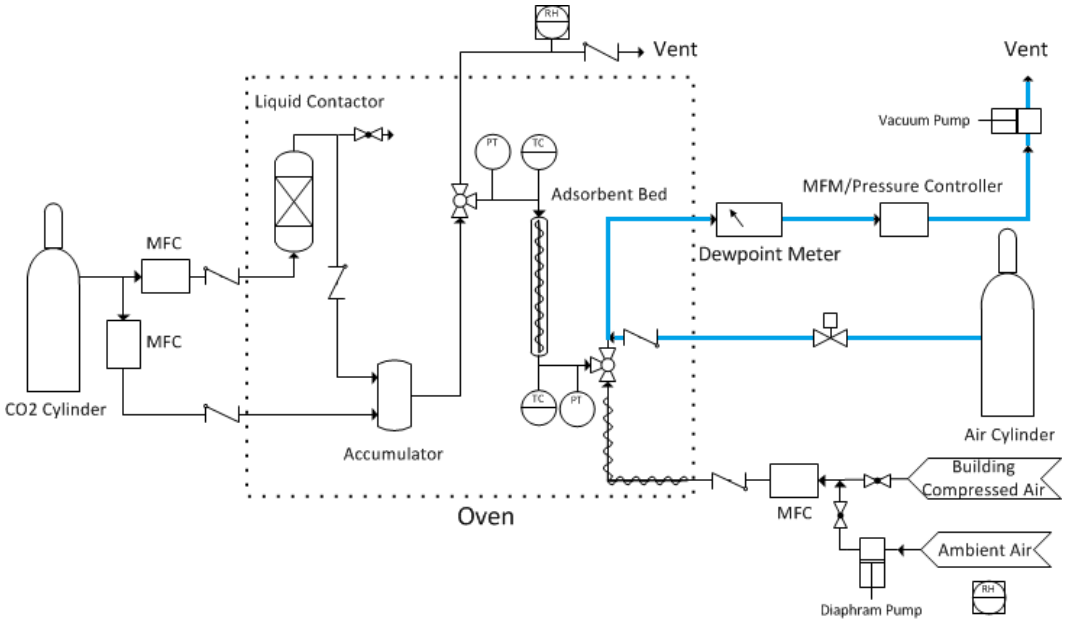

Figure 2-7. Gas flow path during cooldown phase of CO_2 drying experiment

humidity/temperature meters and from the Alicat MFCs were collected by an Edgeport USB controller and brought to the Labview program. All process inputs and outputs were displayed on the main dashboard screen of the Labview program, as shown in Figure 2-8. From this dashboard valves, pumps, gas flowrates, system backpressure, and bed temperature could be manually controlled. Cycles could be started, the number of cycles set, and the progress of cycles tracked from this screen. Though cycle operation was controlled from this screen, cycle parameters were set on the cycle configuration screen shown in Figure 2-9. On this screen, the flow rates for the various stages of cycle operation were input, as well as the trigger values to sequence the program through the various cycle steps. Each cycle started with a desorption phase where an air flow rate and bed temperature were set and Valves 1A and 1B (both operated by Valve 1 in the Labview program) moved to their desorption position. The desorption phase ended when either the vent humidity meter RH1 reached its setpoint or when a certain amount of time had elapsed at the temperature setpoint.

Upon completion of the desorption phase, the cooldown phase was initiated where air flow stopped and the bed was allowed to cool with Valves 1A and 1B actuated to their adsorption position. Simultaneously, nitrogen flow to dry the dewpoint sensor was initiated by actuating Valve 2. The cooldown phase ended when the dewpoint sensor and bed thermocouples reached their setpoints.

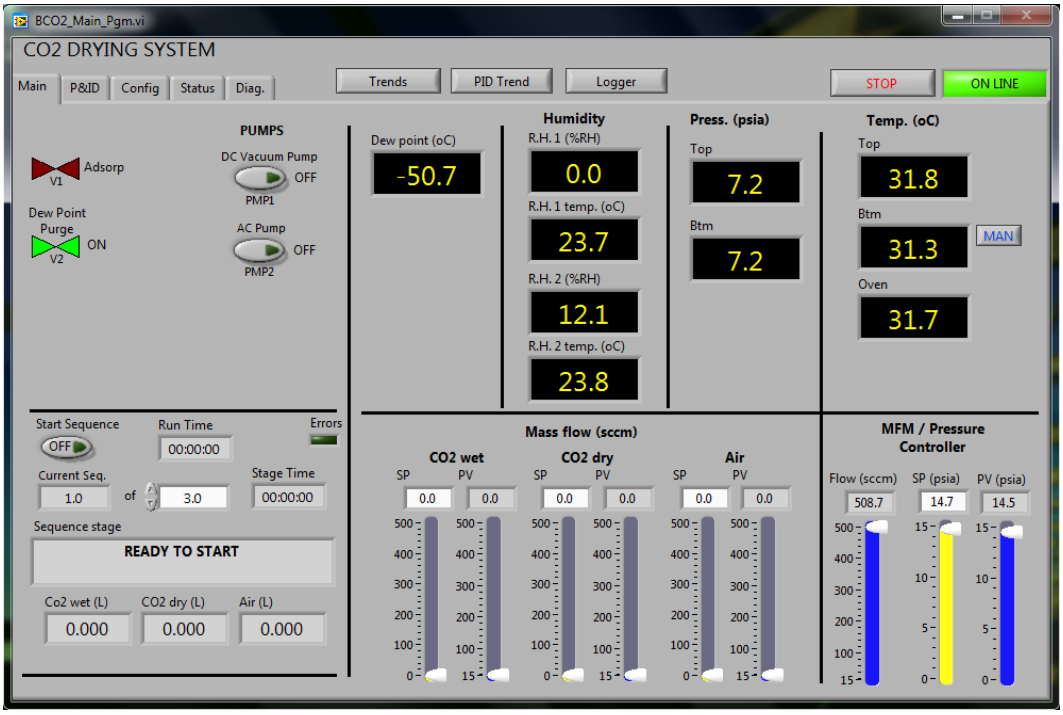

Figure 2-8. CO_2 drying experiment Labview program dashboard screen

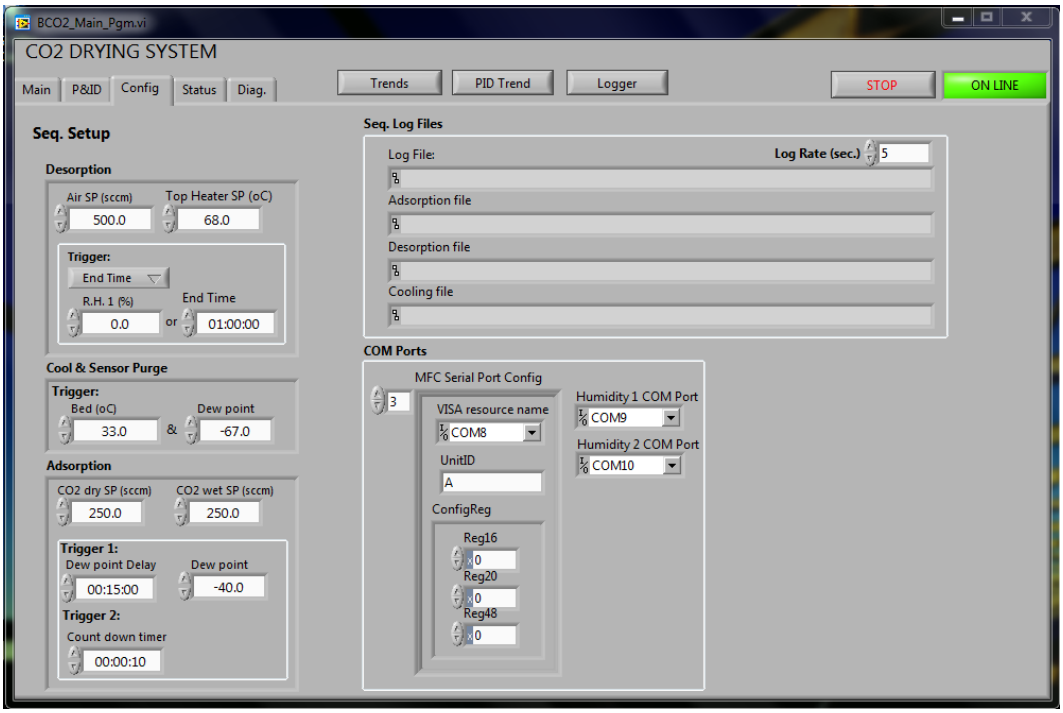

Figure 2-9. CO_2 drying experiment Labview program cycle parameters configuration screen

The adsorption phase then began by closing Valve 2 and isolating the nitrogen purge. The wet and dry carbon dioxide flow rates were then set to their setpoints and the dewpoint of the bed outlet was monitored. When the dewpoint reached a specified value a countdown timer was initiated. When the countdown ended the carbon dioxide flows were set to zero and the next desorption phase would start if required. A delay was built into the start of the dewpoint monitoring to prevent moisture entrained in the tubing downstream of the sensor from creating a slug at the start of the next cycle which would trip the dewpoint sensor and prematurely end the adsorption cycle.

3. Solid Amine CO_2 Adsorbents

A series of aminosilanes was grafted to as-synthesized Na-ETS-2. Aminosilanes containing one, two, and three amine groups were grafted to the surface of ETS-2. The thermal stability of the tethers was assessed using TG-MS under both inert and oxidizing atmospheres. The TG-MS data was also used to assess the capacity of the various samples toward trace amounts of CO_2 in humid air. The adsorption capacities of the grafted amines were assessed using pure gas CO_2 isotherms collected at 30, 50, and 70°C using a static volumetric adsorption system. Gravimetric adsorption cycling experiments under dry CO_2 were carried out to assess each materials approach to cyclic steady state.

3.1 Aminosilane Grafted ETS-2

3.1.1 Air TG-MS

To quantify the amount of grafted material on ETS-2, samples were calcined in air to completely remove the organic material from the surface of the nano-titanate. The MS plots were used to indicate the onset of decomposition of the tether which was unique for each adsorbent.

Figure 3-1 shows the decomposition, in air, of N3-ETS-2. The signal at m/z=15 was used to determine the onset of decomposition because the fragment specific toward the aminosilane decomposition and is unaffected by water or any of the components in air. The obvious spike in the MS plot and corresponding step

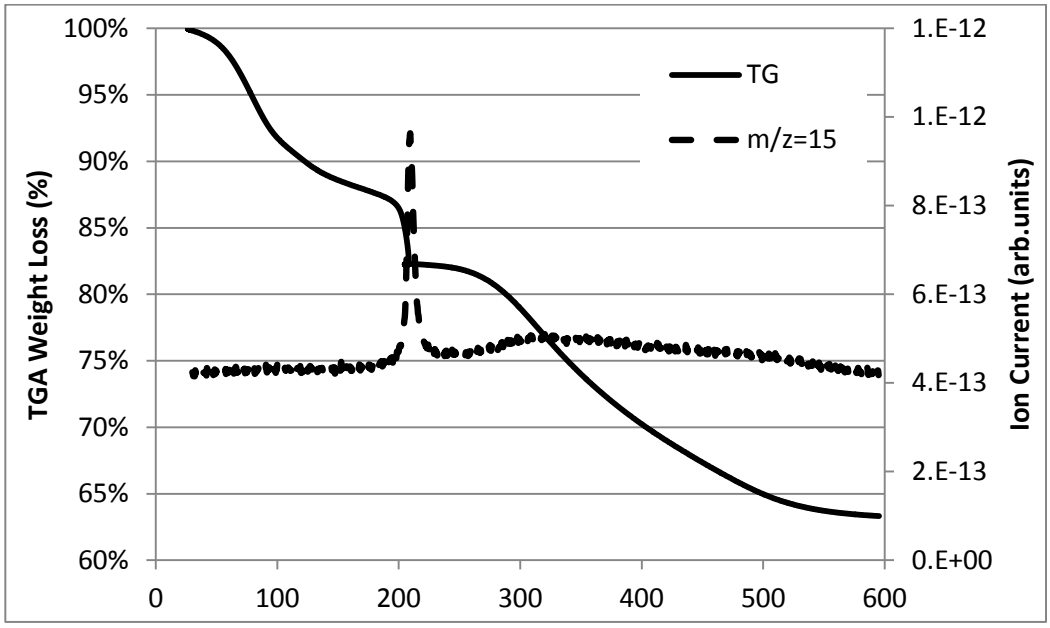

Figure 3-1. TG-MS plot for the calcination of N3-ETS-2 in air

change in the TG plot is characteristic of a combustion event as neither of these features were evident in subsequent scans under a N_2 atmosphere. The quantification of the number of moles of tether per gram of substrate required a number of influences to be taken into account. The TG experiment will only combust the organic fraction of the tether and the silicon atom will be left behind on the substrate. This influences both the calculation of the mass of the tether and the mass of the substrate. Another complication is that the substrate will continue to sinter and evolve water as the temperature is increased and so the total mass loss is a combination of combusted material and water loss from the substrate.

To calculate the weight loss due to the combustion of the tether, the onset of combustion was determined for each sample from the TG-MS plots. The onset

temperatures and onset weights for the adsorbents were taken at 275°C for N1-ETS-2, 200°C for N2-ETS-2, and 190°C for N3-ETS-2. The total weight loss between the onset temperature and 600°C was calculated for each sample from their respective TG plots. As mentioned above, the total weight loss is a combination of the removal of the combustible portion of the aminosilane tether as well as water lost from the substrate.

The weight loss due to water between the various onset temperatures and 600°C was calculated using a TG plot for raw ETS-2. While it might be considered that the grafting procedure would remove surface hydroxyls that would condense at higher temperatures, the MS signal at m/z=18 for the tethered samples shows continual emission of water from the solid as the material is heated. The rise, at elevated temperatures, in the intensity of the signal at m/z=18 was confirmed in subsequent experiments run under dry N_2 which confirmed that the solid is dehydrating at elevated temperatures. The fraction of water lost between the various onset temperatures and 600°C for raw ETS-2 was calculated from the TG plot and then scaled to the individual grafted samples' weight at each of their onset temperatures. Water loss accounted for about 10% of the total mass loss for the grafted samples and thus should be factored out to prevent this effect from skewing the calculations of amine loading. The net loss, used for all subsequent analyses, was calculated by subtracting the weight loss due to water from the total mass lost for each adsorbent's unique temperature range.

The various formula weights used in the assessment of the mass loading of the tethers were arrived at by factoring in only the chemical groups relevant to the

calculation. The molecular weight of the aminosilane tether was calculated by subtracting the three methoxy groups on the original trimethoxyaminosilane reagent because these groups should be lost as methanol during the grafting process. The aminosilane tether is thus the CHN chain including a single silicon atom. Any oxygen associated with the grafting would have come from the substrate and are therefore not accounted for in the calculation of the tether formula weight. The molecular weight of the combustible tether is simply the formula weight of the aminosilane tether less the silicon atom.

The moles of combustible tether were converted to moles of aminosilane tether by scaling the moles of amine chain lost in the TG experiment back to aminosilane by way of their respective formula weights. To determine the weight ratio of aminosilane on the substrate the mass of silicon remaining on the calcined sample must first be subtracted from the residual mass of the sample. This was accomplished by calculating the number of grams of silicon present in the same number of moles of combustible tether. The contribution of the silicon to the substrate mass at 600°C is significant, being on the order of 5 to 6% of the total sample mass.

The values provided in Table 3-1 provide the sequence of values used in the calculations. The term “AS” refers to the aminosilane tether, including the silicon atom. The weight ratio of the aminosilane is the ratio of the mass of aminosilane vs the mass of the bare substrate. The weight fraction is defined as the mass of the aminosilane over the total sample weight (including the tether). The weight ratio scales linearly with the formula weight of the aminosilane

Table 3-1. Values used in the calculation of the mass of aminosilane on ETS-2

	Unit	N1	N2	N3
FW with Si	g/mol	86.17	129.24	172.31
FW without Si	g/mol	58.09	101.16	144.23
Onset Wt	mg	40.21	38.7	35.58
600°C Wt	mg	35.06	29.8	23.65
Water Loss	mg	0.68	1.25	1.14
Net Loss	mg	4.47	7.64	10.79
Si-adjusted Net Loss	mg	6.63	9.76	12.9
Aminosilane	mol	5.19E-05	5.91E-05	6.26E-05
Aminosilane	g	4.47E-03	7.64E-03	1.08E-02
Wt Ratio		12.51%	24.61%	43.55%
Wt Fraction		11.12%	19.75%	30.34%

though the correlation coefficient suggests that the loading of the amine on each sample is not equivalent for all samples. Using the measured surface area of the substrate and the aminosilane molecular cross section (5 x 10^18 molecules/m^2) (Feng, Fryxell, Wang, Kim, Liu, & Kemner, 1997) the aminosilane weight ratio can be calculated at monolayer coverage. Table 3-2 gives the values used in the calculations and the expected tether weight ratios at monolayer coverage for ETS-2. The calculated aminosilane weight ratio at monolayer coverage is higher than the measured values for the N1 and N2 samples but quite close to the measured value in the case of the N3 sample. The same molecular cross sectional area can be used to calculate the surface area of the substrate covered by the *measured* amount of grafted material. The data in Table 3-2 shows that there is an increasing trend in the calculated degree of surface coverage moving

Table 3-2. Values used in the calculation of the weight ratio and surface area coverage of the tethers

Sample	Measured Surface Area	Estimated at Monolayer Coverage	Measured AS Wt Ratio	Calculated Surface Area
	m^2/g	AS Weight Ratio g/g	g/g	m^2/g
N1	290	20.74%	12.51%	175
N2	290	31.11%	24.61%	229
N3	300	42.91%	43.55%	304

from the N1 sample to the N3 sample. Comparing the measured surface area data with the calculated surface coverage it can be determined that the N1 sample is likely 60% covered, the N2 sample 80% covered, and the N3 sample is completely covered with aminosilane tethers. Steric arguments cannot explain why the larger aminosilane provides a higher surface coverage so it is assumed that further synthesis optimization should allow all samples to converge on 100% surface coverage.

3.1.2 Nitrogen TG-MS

TG-MS scans were run under N_2 to determine the onset decomposition temperature for the tethers in a non-oxidizing atmosphere. All of the MS scans showed an interesting and unexpected feature at low temperature at m/z=44. The magnitude of the signals and trends between samples were similarly seen in the air TG-MS data when that signal was examined. Further analysis was done on the N_2 TG-MS data to eliminate the influence of any contamination present in the air stream. Figure 3-2 shows the N_2 TG-MS plot for N3-5TS-2 with the corresponding MS signals at m/z=15 and 44. The TG plot for raw ETS-2 is

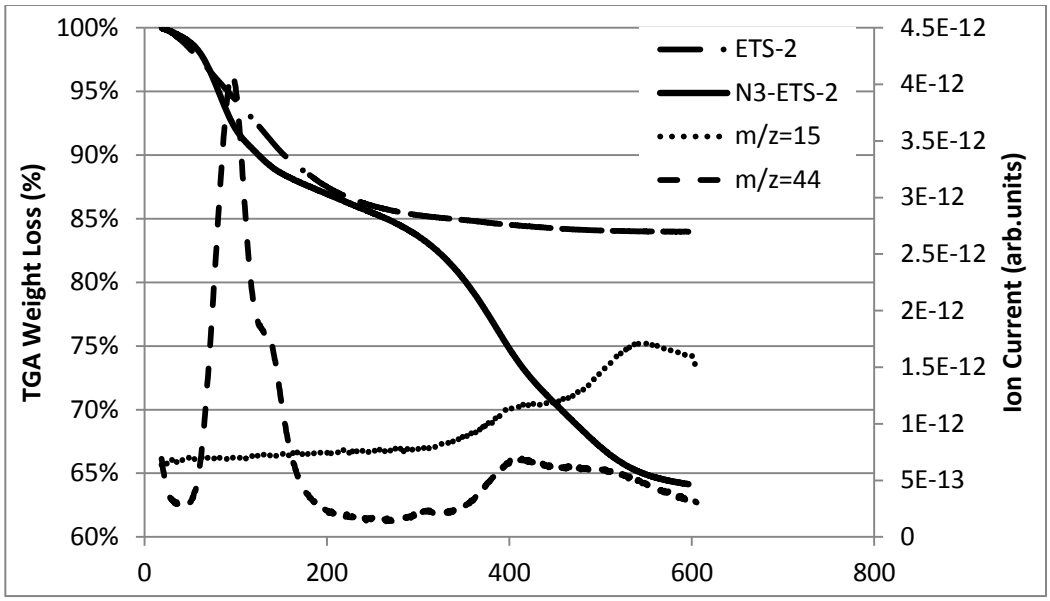

Figure 3-2. TG-MS plots for N3-ETS-2 with the TG plot of ETS-2 shown for reference

overlaid for reference. The difference in the two TG plots is evident in that the N3-ETS-2 sample contains two transitions absent in the substrate. The signal at m/z=15 indicates that the weight loss above 300°C is due to the decomposition of the tether. This result also demonstrates the enhanced thermal stability of the grafted samples under anoxic conditions since the onset decomposition temperature is shifted to significantly higher temperature. The thermal stability of the amine tethers in both air and N_2 appears sufficient for long -term process stability. The regeneration temperature for CO_2 desorption in a packed bed system is expected to not exceed 200°C as this is the temperature at which the amine reboilers are maintained to flash off the adsorbed CO_2. To be competitive, a packed bed system should work within the conventional temperature envelope for amine systems and thus regeneration temperatures in excess of 200°C are not considered.

The low-temperature TG transition centered on about 100°C is assigned to CO_2 desorption from the material. This assignment can be made unambiguously because there is no sign of pyrolysis of the tethers at low temperature (evidenced by the signal at m/z=15) and the analysis system (under N_2) has non-detect levels of CO_2 and hydrocarbons that appear at m/z=44. The CO_2 adsorption on the samples was entirely voluntary as the samples were not pre-treated or pre-conditioned in any way prior to analysis. The observation of CO_2 on the adsorbents suggests the performance of these materials will be unaffected by moisture since the moisture concentration in the lab, while not monitored, is expected to be at least an order of magnitude greater than the ~ 400 ppm of CO_2 present.

The adsorption capacity of the various materials can be assessed by integrating the signal at m/z=44. To maintain a fair comparison, all of the plots were reduced to a common baseline to prevent run-to-run baseline offset from influencing the analysis. The MS traces at m/z=44 were integrated between 30 and 200°C and these integrated ion currents represent the mass of CO_2 adsorbed on the solid. The upper limit of 200°C was chosen because this was identified as the highest common temperature at which there was no evidence of tether decomposition and at which the majority of the CO_2 had been desorbed from the sample. Figure 3-3 shows the overlay of the MS scans at m/z=44 for the N1, N2, and N3 samples that have been adjusted by subtracting each samples initial CO_2 ion current from their respective raw signal values.

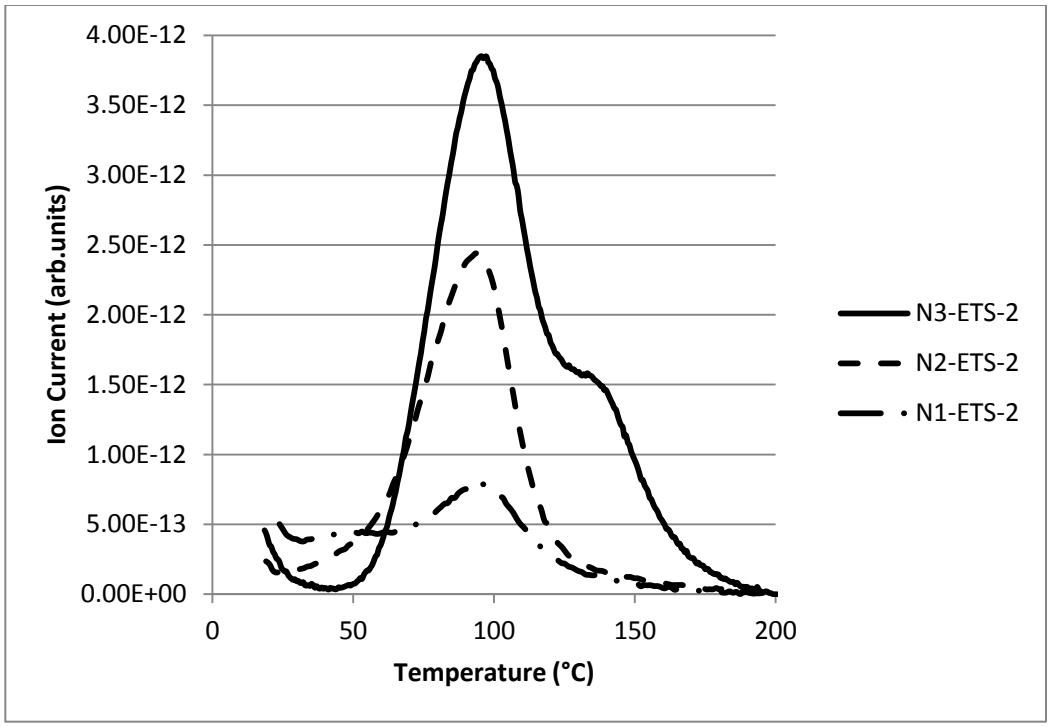

Figure 3-3. MS plots at m/z=44 for N1-, N2-, and N3-ETS-2 heated under N_2

The amount of CO_2 (in arbitrary units) can be standardized by the moles of aminosilane in each sample. Table 3-3 shows the sequence of values used in the calculations. The aminosilane weight fractions calculated from the air TG-MS data can be applied to the sample weights taken from the N_2 TG-MS plots at 200°C and the moles of aminosilane can subsequently be calculated for each sample. Dividing the integrated CO_2 signal by the corresponding molar quantity of aminosilane yields a standardized quantity that factors out the varying sample weights used in the experiments.

The relative performance of the adsorbents can be gauged by normalizing the standardized values against the N1 sample. Table 3-3 shows the trend in the normalized value for relative CO2 capacity and it is evident that the N3 material

Table 3-3. Values used in the calculation of the amount of CO_2 adsorbed per mole of aminosilane

	N1	**N2**	**N3**
FW (g/mol)	86.17	129.24	172.31
Wt % Aminosilane	11.12%	19.75%	30.34%
Onset sample mass (mg)	25.04	31.85	24.17
Aminosilane (mg)	2.785	6.29	7.332
Aminosilane (mmol)	0.03232	0.04867	0.04255
Integrated CO_2 Intensity	4.55E-11	9.18E-11	3.56E-10
CO_2/mmol AS	1.41E-09	1.89E-09	8.37E-09
Normalized Ratio	1	1.34	5.95

has significantly higher capacity compared to the other two samples. This result was not expected since the N3 tether is predominantly secondary amines which aren't as reactive as primary amines. The humidity present in ambient air will, however, allow the secondary amines to participate in CO_2 adsorption and so it would be expected that the CO_2 capacity would scale linearly with the number of amine groups on the tether. The non-linear behaviour of the trend can be explained by taking into account the degree of monolayer coverage for each sample. The 2:1 stoichiometry for CO_2 adsorption in amine systems requires the CO_2 to interact with two amine groups. It is considered that the higher degree of surface coverage and the higher density of nitrogen groups lends the N3 sample a significant advantage compared to the two other samples with lower surface

coverage. The presence of a second peak, at higher temperature, in the trace for the N3 sample in Figure 3-3, establishes the greater adsorption strength for the N3 sample as none of the other sample show similar behaviour though, chemically, the tethers are all comparable. The differences between the samples suggest that the adsorptive performance of grafted, non-porous adsorbents is significantly affected by the degree of surface coverage of the tether.

3.1.3 Adsorption Isotherms

The CO_2 isotherms at 30°C for the three amine samples are shown in Figure 3-4. There is little differentiation between samples at 30°C though the N1 material has a marginally higher capacity. This could be expected given that the N1 material is comprised entirely of primary amine groups which are more

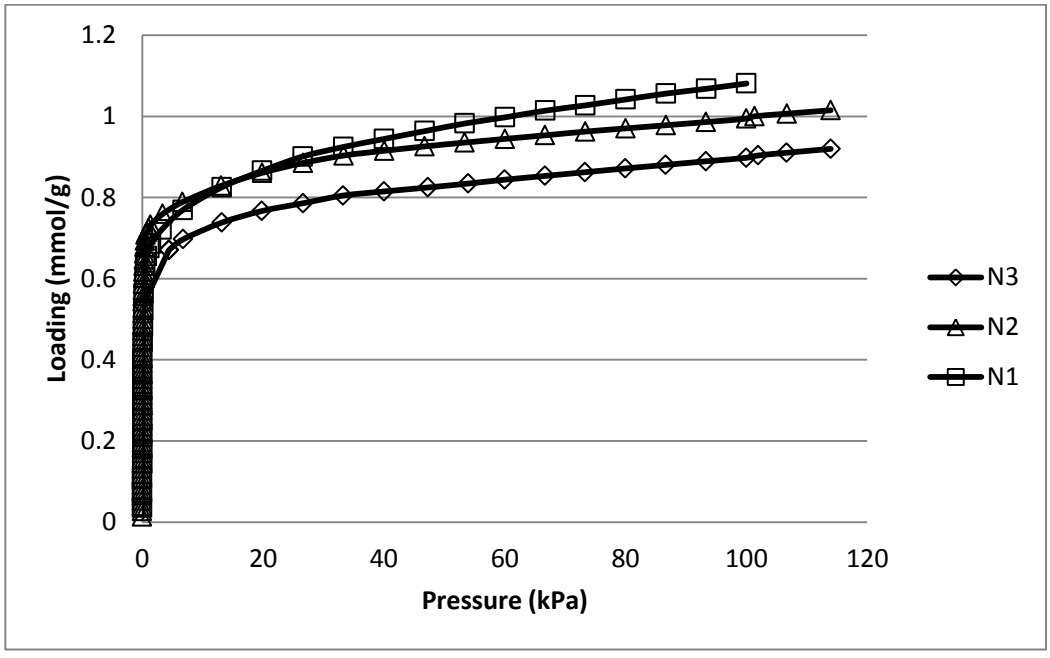

Figure 3-4. CO_2 adsorption at 30°C for aminosilane grafted ETS-2

reactive toward CO_2 compared to secondary and tertiary amines (Ko, Shin, & Choi, 2011). Kinetic influences could also contribute to this trend because the activation barrier for the reaction of the CO_2 with the amines is not expected to be overcome easily at 30°C. Kinetic effects can be expected since the equilibration delay used in the analyses is typical of small molecule adsorption on molecular sieves and will be biased against a slow approach to equilibrium. It should also be considered that all of the adsorption experiments presented are run under rigorously anhydrous conditions and thus the amines cannot take advantage of moisture acting as a promoter to form carbamate ions (Palmeri, Cavallaro, & Bart, 2008) (Park, Lee, Choi, & Lee, 2005) (Zelenak, Halamova, Gaberova, Bloch, & Llewellyn, 2008). The presence of a promoter could change the adsorption characteristics and/or rates compared to the data presented.

At 50°C the CO_2 isotherms (Figure 3-5) begin to show a trend with respect to the number of amines on the tether and at 70°C (Figure 3-6) there is a clear differentiation between the various samples. Figure 3-6 also includes the CO_2 isotherm for the raw ETS-2 substrate. The ETS-2 substrate demonstrates an affinity for CO_2 and the isotherm is well described by the Toth equation suggesting strong physisorption. Isotherms for the substrate were collected at 30, 50, and 70°C and the isosteric heat of adsorption calculated for CO_2 on raw Na-ETS-2 exceeds 30 kJ/mol at loadings less than 0.6 mmol/g and exceeds 40 kJ/mol at loadings below 0.3 mmol/g. At low partial pressures, however, the adsorption characteristics of the tethered samples is obviously directed by the

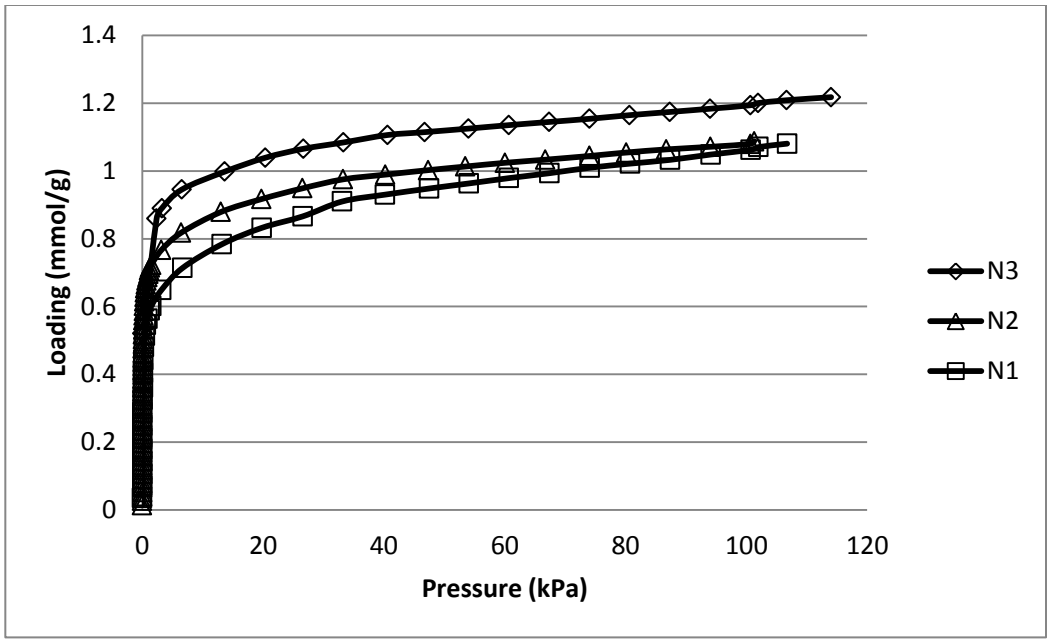

Figure 3-5. CO_2 adsorption at 50°C for aminosilane grafted ETS-2

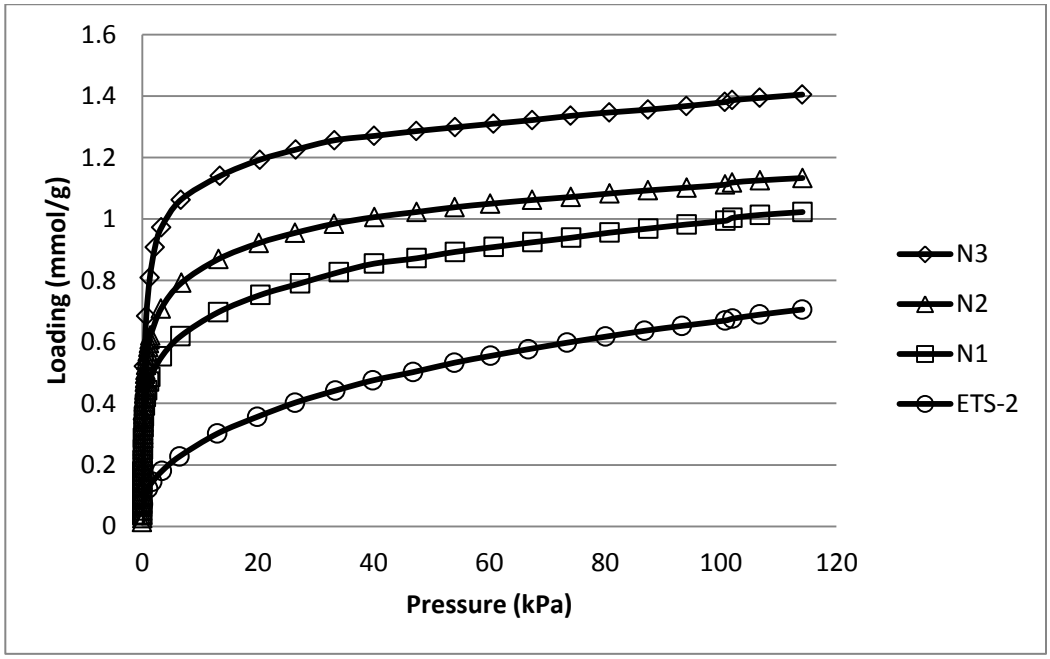

Figure 3-6. CO_2 adsorption at 70°C for aminosilane grafted ETS-2

chemistry of the tether because the CO_2 isotherm for the substrate lacks the rectangularity seen in the tethered samples. The progressive increase in capacity with CO_2 partial pressure for the tethered samples could be due to the gas interacting with the substrate because the specificity of the amine-CO_2 interaction does not predict a rise in capacity with increasing partial pressure.

At 70°C equilibrium effects should be minimized due to the greater amount of thermal energy in the gas molecules and, at this temperature, it is reasonable to assume that activation barriers are largely overcome. The comparison of the adsorption capacity of the adsorbents used the 70°C isotherms because it was felt that these isotherms were the least influenced by equilibrium effects. A similar analysis that was done using the N_2 TG-MS data can be done using adsorption data at 70°C. The capacity at 50 kPa was selected as the point of comparison because this represents a likely upper limit in the partial pressure of CO_2 that might be encountered in a flue gas cleanup process. The central pressure in the isotherm also limits the bias due to the contribution from the substrate to the overall capacity of the sample. The adsorption data at 50 kPa in mmol/g was converted to express the capacity of the adsorbent as moles of CO_2 adsorbed per mole of aminosilane. The same aminosilane weight fractions and formula weights used in analysis of the N_2 TG-MS data were used in the analysis of the volumetric adsorption data.

Table 3-4 shows the values used in the calculations and the results of the comparison. When the moles of CO_2 adsorbed are standardized against the number of moles of aminosilane, it becomes apparent that the adsorptive

Table 3-4. Values used in the normalization of 70°C volumetric adsorption data

	FW AS	**Wt % AS**	**CO_2 Capacity at 50 kPa** (mmol/g)	**mol CO_2/g AS**	**mol/mol (CO_2/AS)**	**Normalized**
N1	86.17	11.12%	0.87	0.00782	0.674	1
N2	129.24	19.75%	1.04	0.00527	0.681	1.01
N3	172.31	30.34%	1.3	0.00429	0.738	1.1

capacity for all of the samples is roughly equivalent. A slight upward trend from the N1 to the N3 sample can be noted but the increase does not scale with the number of amines on the chain. Normalizing these ratios against the N1 sample it becomes clear that the secondary amines are, at best, only marginally active for CO_2 adsorption under the experimental conditions.

This result is reasonable as it is known that only primary amines have a facile reaction with CO_2 in the absence of water vapour and the activation condition for the samples effectively excluded all water vapour from the system. The slight increase in the normalized ratio from the N1 to N3 sample could be due to some engagement of the secondary amines in CO_2 adsorption and, in the case of the N3 sample, an amplification in secondary amine engagement could be due the higher degree of surface coverage. The influence from the substrate should be similar in all cases and the influence of the substrate would be expected to be more pronounced for the N1 and N2 samples as they have a lower degree of surface coverage. The fact that a reverse trend in capacity is not noted suggests that the contribution of the substrate under the test conditions is relatively similar

in all cases. The N_2 TG-MS data showed a clear enhancement in CO_2 capacity for the N3 sample while the volumetric adsorption data indicates the performance of all tethers is comparable once the number of moles of tether on each adsorbent is accounted for. The contrast between the relative efficiencies of the adsorbents between data sets confirms the importance of water as a promoter in these materials.

3.1.4 Adsorption Cycling

Adsorptive cycling experiments were performed to examine the approach of the adsorbents to cyclic steady state under non-equilibrium conditions. The CO_2 capacity for the adsorbents isn't quantified using this data because of the uncertainty attached to the partial pressure CO_2 used in the experiment. It can be assumed that the purge gas is mixed with the balance gas to create a stream that is perfect a blend of the two but the mixing dynamics in the instrument are not known and this assumption may not be reliable. The instrument operation, however, is expected to be consistent for each cycle and each sample. As such, the trends seen in the data are considered quantitative while the CO_2 uptake values are semi-quantitative.

An example of the adsorption cycling for the N3-ETS-2 sample is shown in Figure 3-7 where it can be seen that the sample does not equilibrate with CO_2 within time allotted. This result is common for all of the tethered samples and could be due to the anhydrous condition of the test which favours the primary

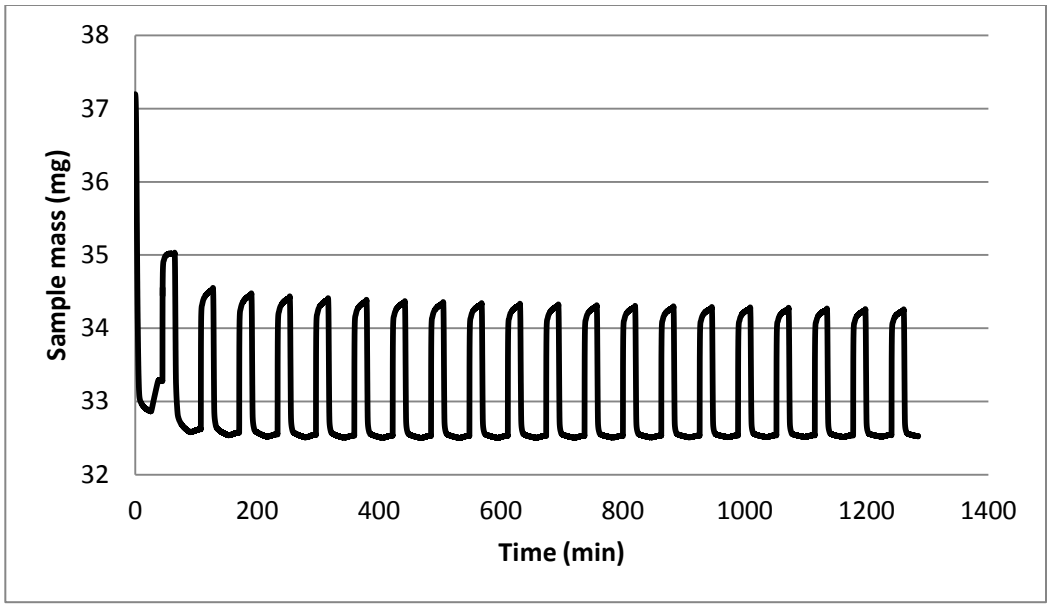

Figure 3-7. TG plot for CO_2 adsorption/desorption cycling on N3-ETS-2

amine on the tether or it could be due to system dynamics where the atmosphere within the instrument is not equilibrated within the given 20 minute period. Rather than invest in additional equilibration time, it was elected to run additional cycles to map the approach of the samples to cyclic steady-state.

The weight change for each cycle was measured from the plateau at 70°C under N_2 (just before the sample purge gas was switched to CO_2) until the end of the 20 minute isothermal delay used for CO_2 adsorption. To confirm the stability of the measurement the amount of CO_2 adsorbed and desorbed for each cycle was measured. The amount of mass gained during CO_2 adsorption was equal to the amount lost during regeneration within a hundredth of a milligram which is well within the uncertainty of the measurement.

The mass change during CO_2 adsorption was standardized using the moles of aminosilane present on the sample. The moles of aminosilane on each sample

were calculated by applying the respective weight fraction for each tether to the sample mass measured before the final adsorption step. The same analysis was done using the sample mass measured before the first CO_2 adsorption and the results are indistinguishable. From Figure 3-8 it is apparent that three samples begin having roughly the same CO_2/aminosilane ratio. This was expected since the CO_2 isotherm data demonstrated that the adsorption capacity of the three samples, under dry conditions, should be roughly equivalent when the adsorption capacity is standardized by the number of moles of amine on the support. As additional cycles are run the samples begin to distinguish themselves in their approach to steady state. While the N1 sample shows a relatively steep downward trend the N3 sample appears to be trending to steady state toward the end of the 20 cycles. The N2 sample displays behaviour somewhere between the

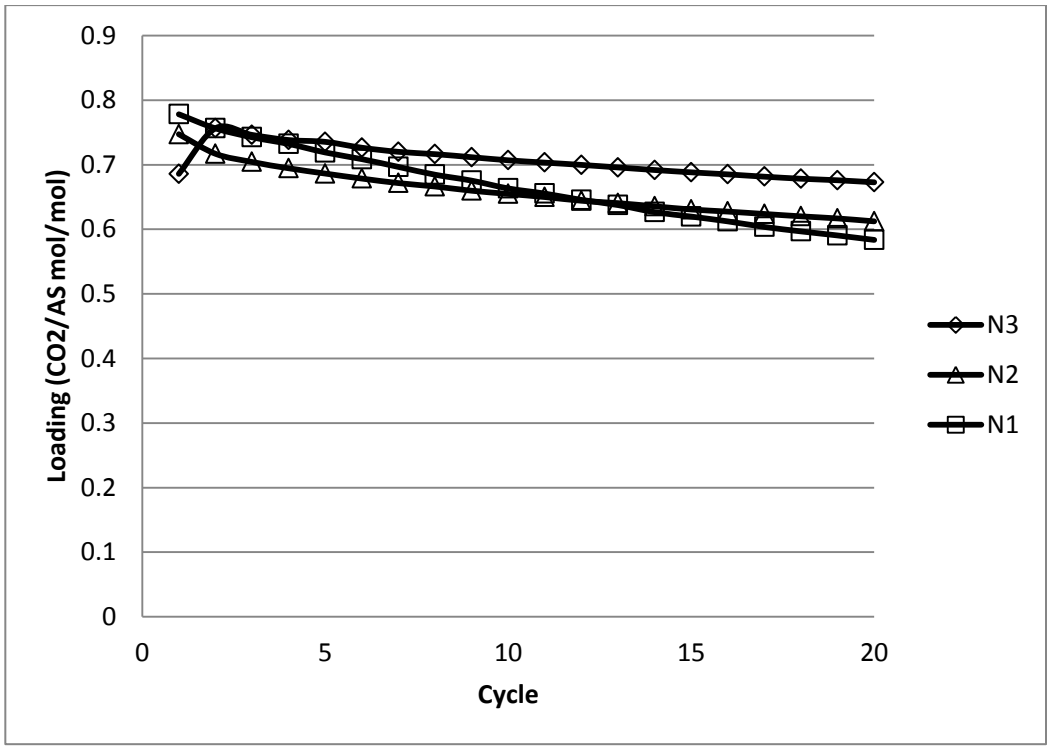

Figure 3-8. Cyclic CO_2 capacity for aminosilane grafted ETS-2

other two samples; dropping capacity as a function of cycle time yet not at the same rate as the N1 sample. The gradual loss in capacity is not likely due to the degradation of the tethers as all previous experiments have demonstrated that the tethers are thermally stable toward the selected regeneration temperature. Likewise, the substrate is not expected to be contributing to this behaviour since a sample of Na-ETS-2 was analyzed using the same protocol and the sample reached cyclic steady state within 10 cycles and displayed a loss of less than a percent over the span of cycles (Figure 3-9). It is probable that the cycle chosen, combined with the experimental conditions, are preventing the samples from equilibrating within the given cycle and that 20 cycles may not be sufficient to achieve cyclic steady state under anhydrous conditions.

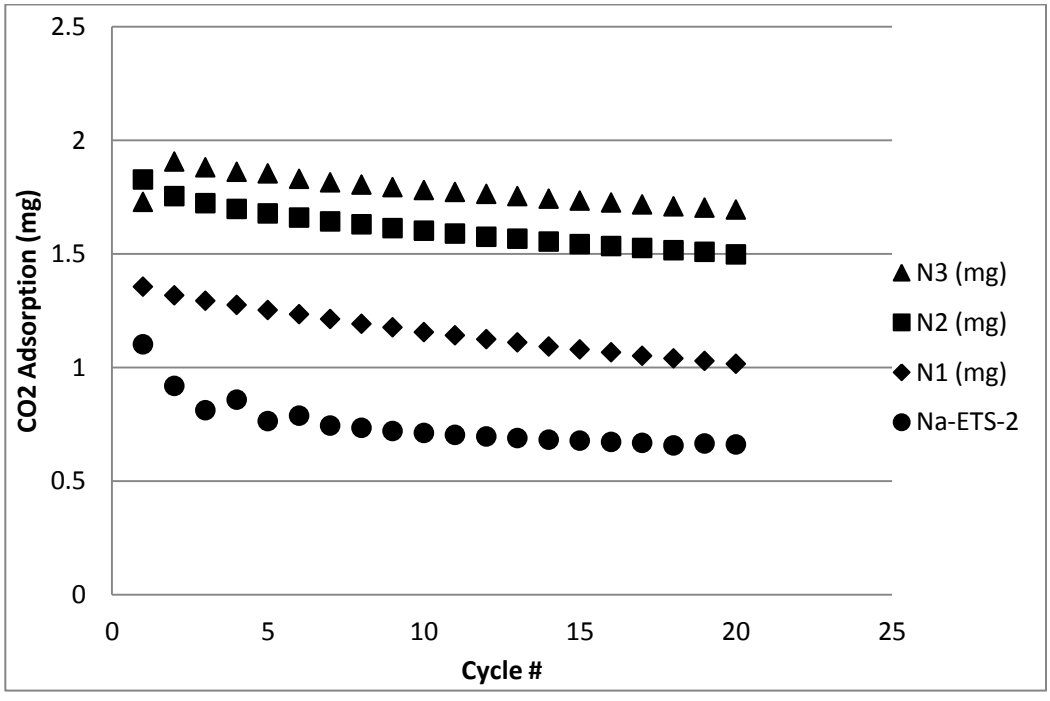

Figure 3-9. Gravimetric uptake of CO_2 for grafted and ungrafted ETS-2

It is not clear why the downward trend in capacity is not associated with any gain, or loss, in sample mass. It was measured that each cycle is completely reversible and that the activated sample mass does not fluctuate from cycle to cycle. The cyclic losses are thus not apparently due to accumulation of CO_2 on the solid nor are they due to the cumulative loss of some necessary component from the sample. It is proposed that the adsorption of CO_2 on such composite adsorbents under the test conditions is not well enough understood to provide a clear mechanism to explain the measured behaviour. It is anticipated, however, that the same tests run under humid conditions should provide the conditions necessary for the amines, and particularly the secondary amines, to behave in a manner which mirrors the accepted mechanisms for CO_2 adsorption.

The degree of aminosilane surface coverage could influence the rate at which the samples can adsorb CO_2. The closer proximity of the tethers in the N3 sample should provide a more uniform adsorption field and the close packing of the tethers should facilitate the stoichiometry needed for carbamate formation. In the N1 and N2 samples, the tethers should be further apart, on average, which should create a barrier to reaction. A sensitivity to the degree of monolayer coverage is reasonable for these samples since ETS-2 cannot take advantage of pore amplification effects where the pore system of the substrate can locally concentrate components and thus facilitate reaction with the amine functions on the tether.

3.2 Conclusions

The first series of non-porous, amine-grafted nano-titanates was prepared using a range of aminosilanes containing up to three amine groups on the chain. The N3-ETS-2 sample was shown through TG-MS to have 5X the capacity of the N1 sample for removing trace-levels of CO_2 from ambient air. The adsorption results demonstrated that anhydrous adsorption conditions favour the primary amines and that the benefits of having multiple amine groups on the tether are not measurable under such test conditions. The non-porous nano-titanates are considered to be sensitive to the degree of aminosilane monolayer coverage and that enhanced capacity and adsorption rates can be realized when the aminosilane density approaches monolayer coverage of the substrate. This behaviour may be unique to high surface area, non-porous substrates because they cannot take advantage of pore amplification effects where the pore system of the substrate can locally concentrate gases or vapour and thus facilitate reaction with the amine.

3.3 Future Work

The measured sensitivity the grafted nanotitantes show toward surface coverage should direct future efforts to increasing the degree of surface coverage of the aminosilane molecules on the ETS-2 substrates. This reportedly can be accomplished by rigorously drying all components used in the grafting process and by performing the grafting under a dry, inert atmosphere. The reactivity of the primary amines toward CO_2 adsorption suggests that the capacity of the adsorbents could also be increased by grafting aminosilane molecules having a larger number of primary amines spread over a larger surface area (via branches off the central tether chain). The aminosilane grafted ETS-2 materials should also be tested across a range of humidity to understand what, if any, affect moisture has on promoting the adsorption of CO_2 on the various amine groups on the tether. It was also recognized that an opportunity exists to map the surface coverage of the substrate by reacting the amine groups with a mineral acid such as HBr or HI. The heavy atom would facilitate 2D EDX measurements of the platelets as the strong signal from the heavy atom signal would help map the distribution of amine groups on the surface.

4. CO2 Drying

The CO_2 drying performance of Na-, Ca-, and Ca/H- forms of ETS-10 were compared to that of commercial silica and zeolite desiccants. A wet CO_2 stream was dried using a single packed-bed column. The moisture capacity and the percent recovery were calculated at breakthrough for the ETS-10, silica, and zeolite 4A desiccants. The drying performance was compared at 50%, 75%, and 100% relative humidity (RH) with a constant bed regeneration time, temperature, and air flow and constant adsorption temperature.

4.1 Material Characterization

4.1.1 Powder X-Ray Diffraction

X-ray diffraction patterns (XRDs) were obtained for all the adsorbents used in this study to verify their identities. Figure 4-1 shows the XRD pattern for the Ca-ETS-10 adsorbent prepared for the study. The peaks which are characteristic of ETS-10 were marked with (a). The peaks marked with (b) are characteristic of ETS-4 which is a typical secondary phase that may be synthesized as a by-product of ETS-10 synthesis. The remaining peaks are likely due to trace contaminants such as recrystallized silicates from ETS-10 synthesis or calcium salts recrystallized after ion exchange. Figure 4-2 shows the XRD pattern for the mixed ion Ca/H-ETS-10 adsorbent. The peaks are marked with (a) again indicating ETS-10 and (b) indicating ETS-4. These can be compared to the XRD pattern obtained for the as-synthesized, sodium form of ETS-10 shown as Figure 4-3. The peak shapes

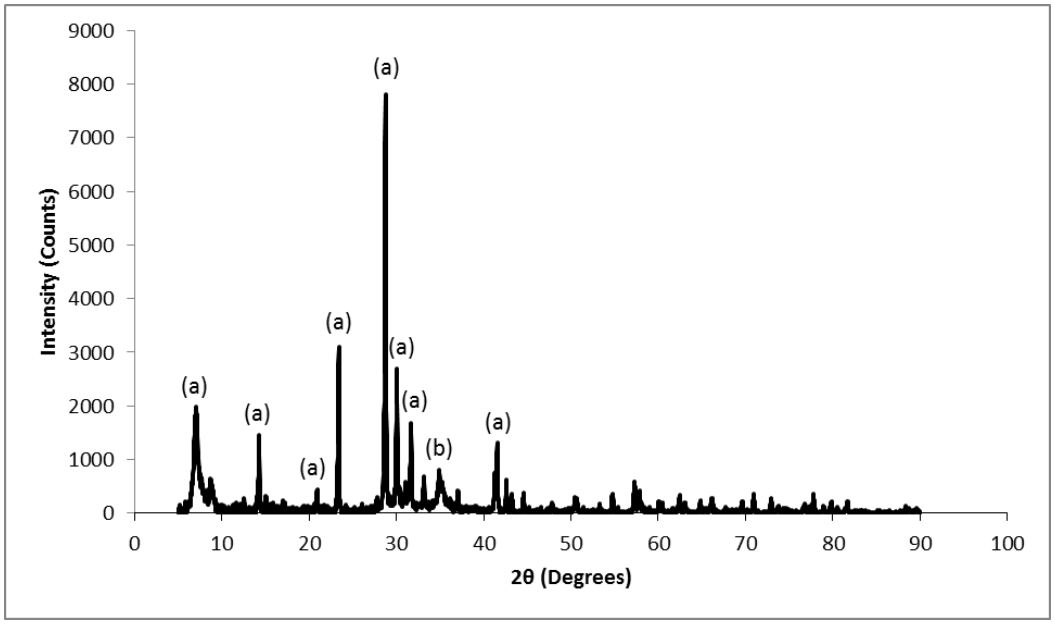

Figure 4-1. Powder XRD pattern obtained for Ca-ETS-10 adsorbent

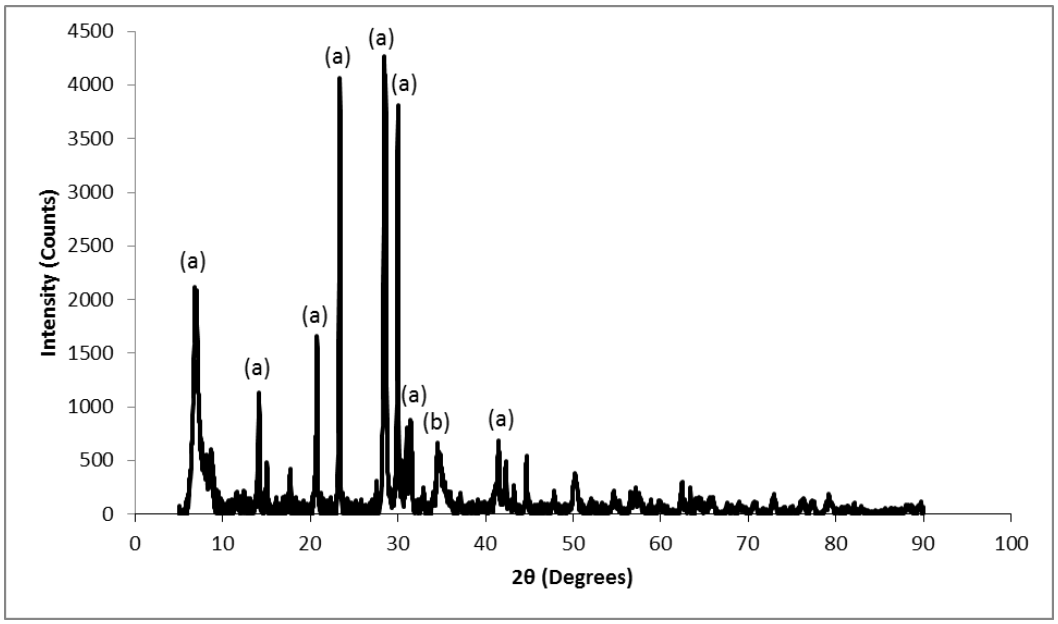

Figure 4-2. Powder XRD pattern obtained for mixed ion Ca/H-ETS-10 adsorbent

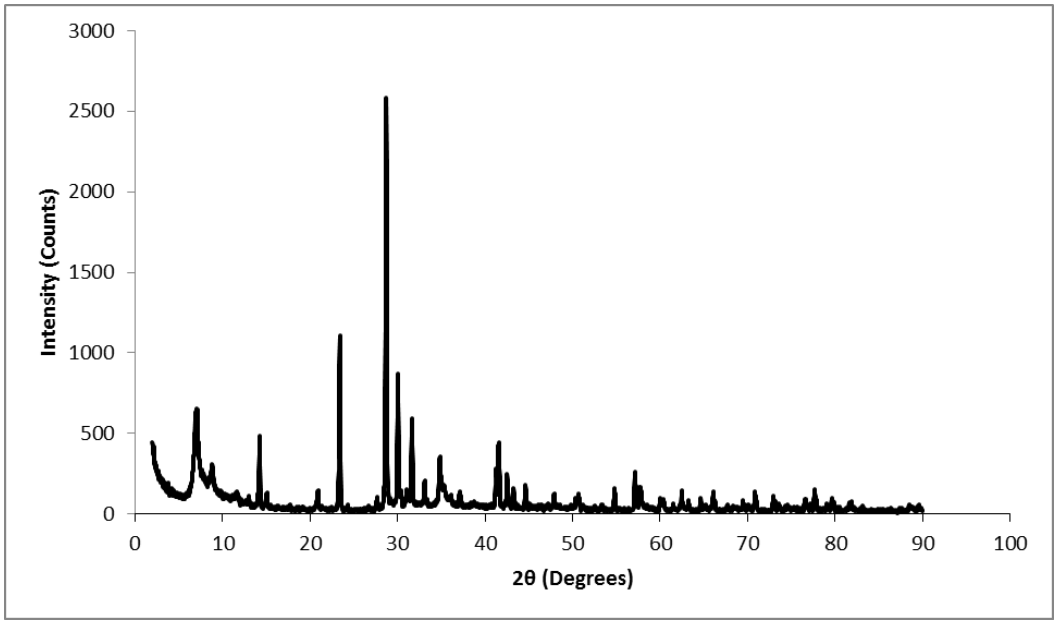

Figure 4-3. Powder XRD pattern obtained for as-synthesized Na-ETS-10

and locations match well in all three patterns which indicates that, as expected, the ion exchange procedures had no significant impact on the ETS-10 adsorbent crystal structure.

Figure 4-4 is the XRD pattern obtained for the zeolite 4A pellets used. Peaks labelled with (a) are characteristic of zeolite 4A and the peaks labelled (b) are typical of kaolin, a binding agent often used in manufacturing zeolite pellets. Other peaks are likely from other clays minerals used in the binder formulation or from metakaolin formed during calcination.

The powder XRD pattern for the aluminum oxide adsorbent used is shown in Figure 4-5. Peaks in the pattern labelled with (a) were identified as those characteristic of either η-alumina or γ-alumina. The XRD patterns of these two phases are very similar and so cannot be differentiated based on this method alone (Maciver, Tobin and Barth 1963). The peak labelled (b) corresponds well with

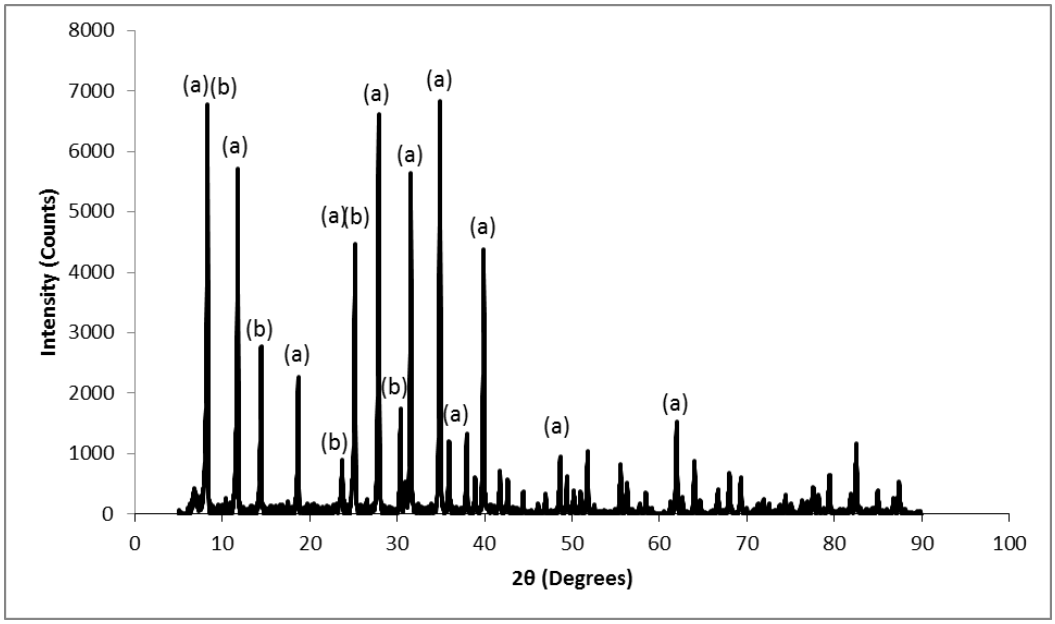

Figure 4-4. Powder XRD pattern obtained for crushed zeolite 4A adsorbent pellets

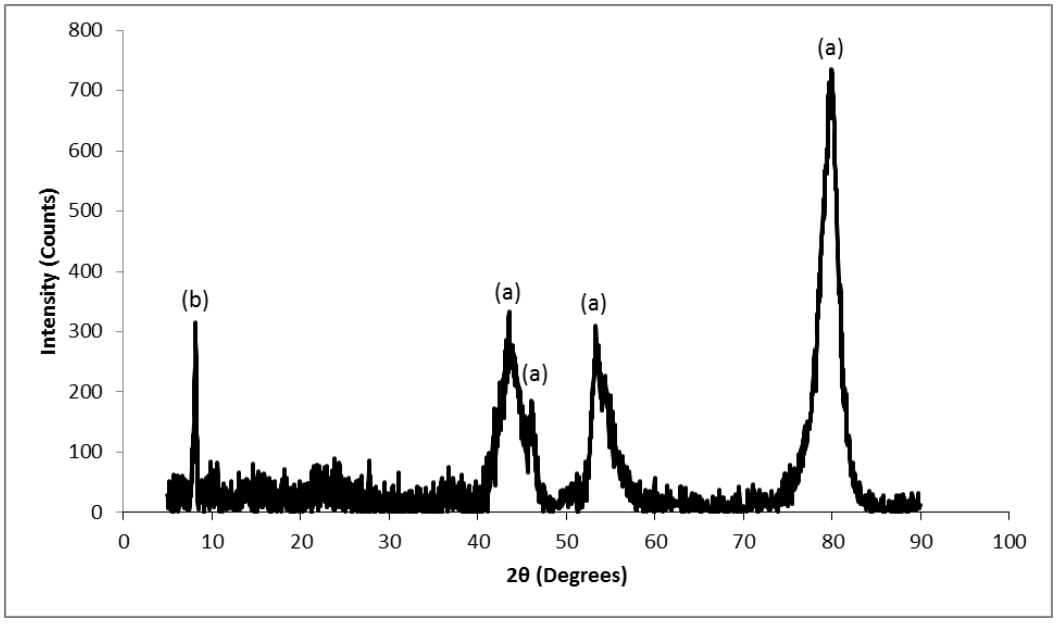

Figure 4-5. Powder XRD pattern obtained for activated aluminum oxide

one characteristic of anorthite, a calcium feldspar, though this seems unlikely as there is no reason for calcium to be present in the sample. The peaks in in this diffraction pattern are noticeably broader than those in any of the ETS-10 patterns. This is likely due to small crystal size of the particles or the presence of some amorphous alumina in the adsorbent sample. A highly crystalline material will have well-defined, sharp XRD peaks whereas an amorphous or semi-crystalline material will have no peaks or wider more blurred peaks. As the alumina used here was of laboratory grade and had lower than typical surface area it likely was less crystalline as well.

The diffraction pattern for silica gel is shown in Figure 4-6. This diffraction pattern shows no peaks and instead exhibits a large baseline roll. This type of pattern is characteristic of a glass having no long-range order and makes silica gel the only completely amorphous adsorbent used in this study.

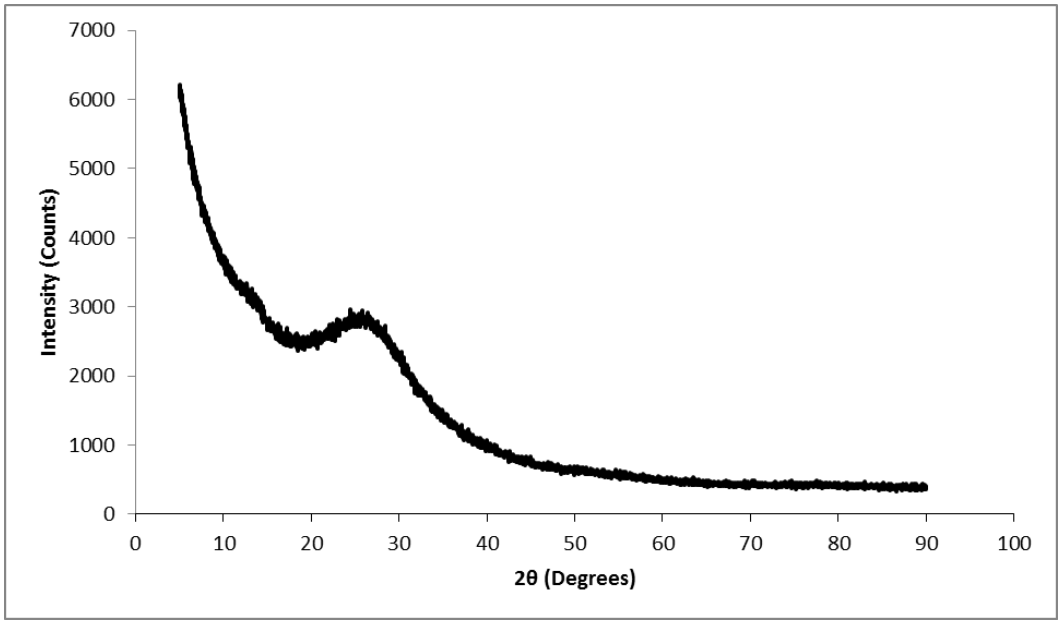

Figure 4-6. XRD pattern obtained for crushed Grace Davinson grade 40 silica gel

4.1.2 Scanning Electron Microscopy (SEM)

To characterize and compare the morphology and size of the adsorbent crystals, scanning electron micrographs were taken of the various ETS-10 adsorbents. The SEM investigation was limited to the ETS-10 adsorbents as to confirm their quality. The commercial adsorbents were used as-received and without inspection. SEM micrographs of as-synthesized Na-ETS-10 at two different magnifications are shown as Figures 4-7 and 4-8. The crystal habits can be seen in Figure 4-7. A survey of the many crystals shown in Figure 4-8 reveals that many particles have numerous defects. Additionally some plate like crystals can be seen amongst the cubic ETS-10 crystals. These crystals match the morphology of ETS-4 which is often a synthesis by-product when synthesizing ETS-10. Based on these observations this Na-ETS-10 was considered to be of suitable quality.

Figures 4-9 and 4-10 show SEM micrographs of Ca-ETS-10 at the same magnifications. After the ion exchange, similar crystal morphology and defects can be seen. Platelets of ETS-4 can also still be located in Figure 4-10 though they appear to be more numerous. The exterior of the ion exchanged crystals does appear to have more defects which may be the result of recrystallization during ion exchange, but as the XRD patterns remained unchanged there was apparently no influence on the overall crystallinity.

SEM micrographs of mixed ion Ca/H-ETS-10 are shown at the same two magnifications in Figures 4-11 and 4-12. As in the earlier SEM micrographs, defects in the crystals can be seen as well as platelets of ETS-4 crystals.

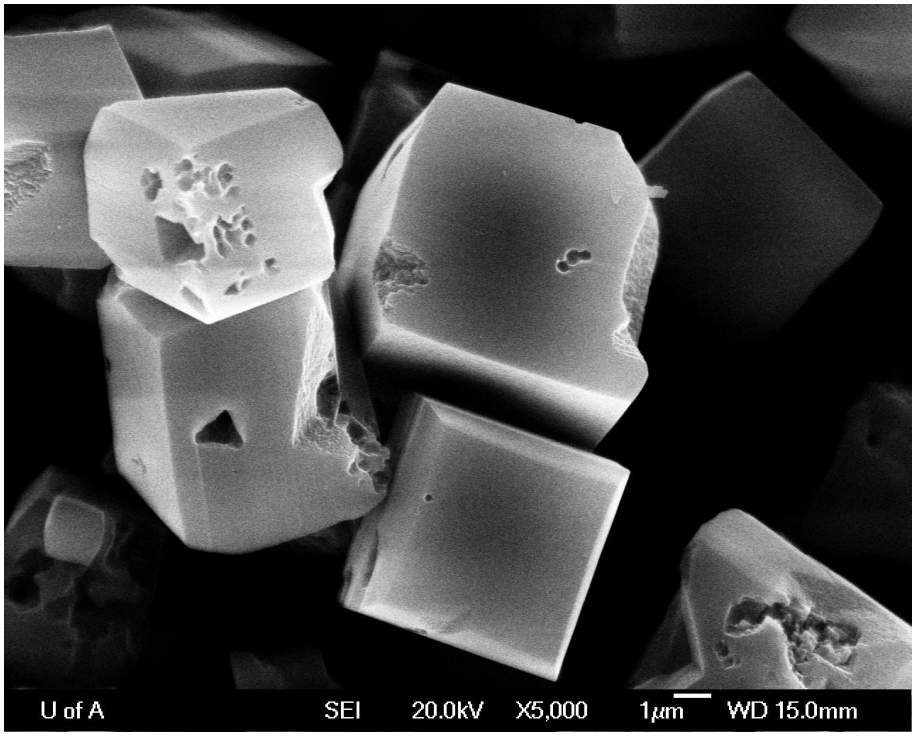

Figure 4-7. SEM micrograph of as-synthesized Na-ETS-10 at 5,000X magnification

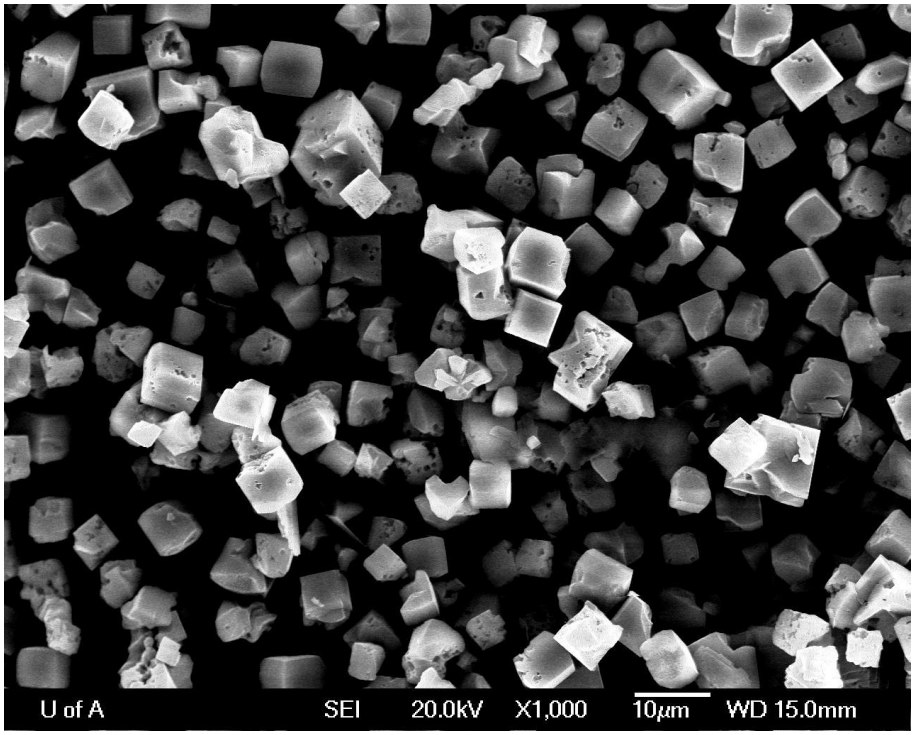

Figure 4-8. SEM micrograph of as-synthesized Na-ETS-10 at 1,000X magnification

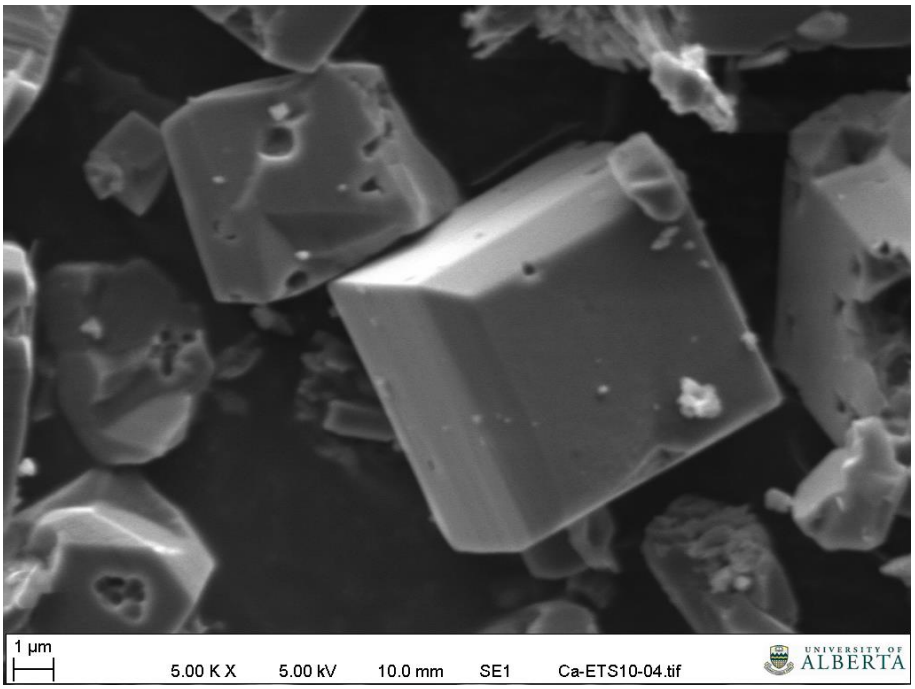

Figure 4-9. SEM micrograph of Ca-ETS-10 after ion exchange at 5,000X magnification

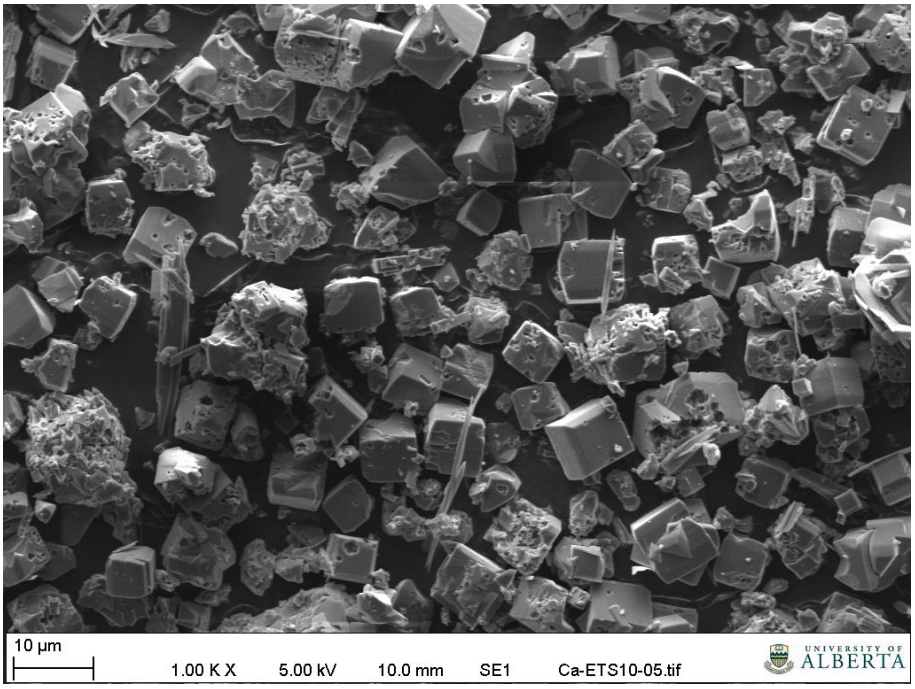

Figure 4-10. SEM micrograph of Ca-ETS-10 after ion exchange at 1,000X magnification

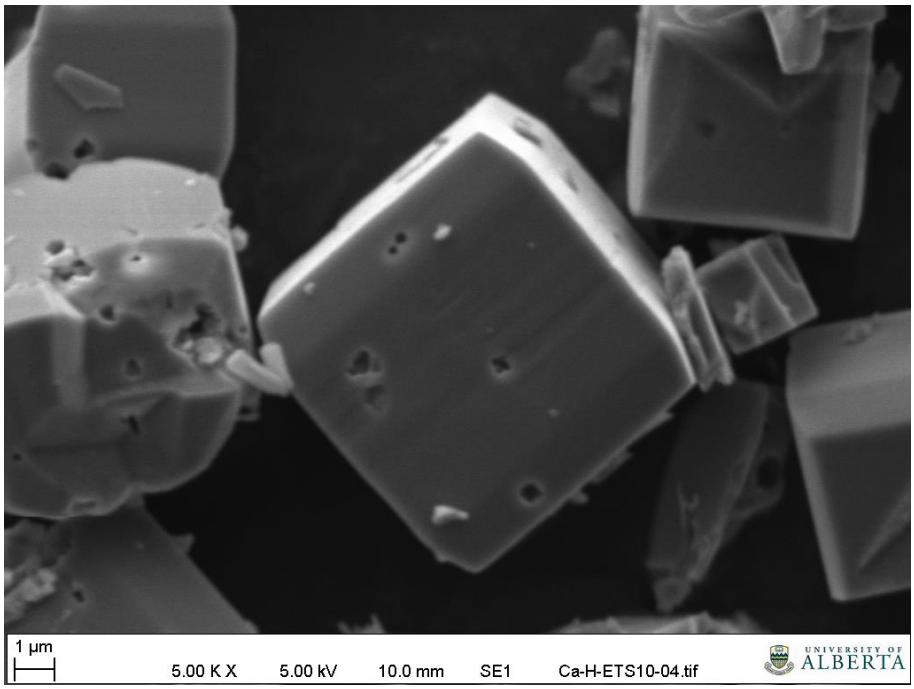

Figure 4-11. SEM micrograph of mixed ion Ca/H-ETS-10 after ion exchange at 5,000X magnification

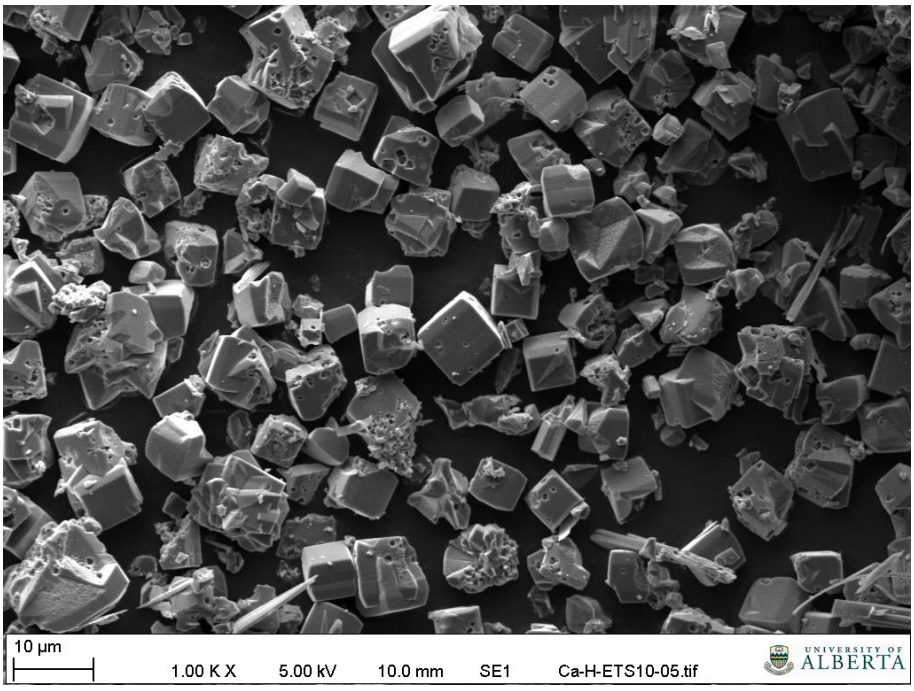

Figure 4-12. SEM micrograph of mixed ion Ca/H-ETS-10 after ion exchange at 1,000X magnification

4.1.3 Energy Dispersive X-ray Spectroscopy (EDX)

The ETS-10 adsorbent samples were further analyzed using EDX. Table 4-1 shows the results of this analysis with the relative amounts of each element shown as an atomic percent. Each of the ion exchanged adsorbent samples was analyzed at three different points. The five elements chosen for determination were silicon, titanium, sodium, calcium, and potassium. These elements were selected as Si, Ti, and O make up the framework of the ETS-10 structure, while Na and K are the typical cations which balance the net negative charge of the framework. Ca was measured for exchanged samples.

Several observations can be made from the EDX data. The amount of Na present drops significantly after both single ion Ca and mixed ion Ca/H exchange, indicating that the Na^+ ions are being displaced by the Ca^{2+} and H^+ ions. We also notice a slight decrease in the K^+ ions present after ion exchange, but the decrease is far less than that of the Na^+ ions. This indicates that the K^+ ions are less exchangeable than the Na^+ ions. This result is typical of ETS-10 ion exchanges, and can be explained by the location of the Na^+ and K^+ ions within the framework. Anderson proposes that the K^+ ions are locked within the cages of the structure and are thus unavailable for exchange, while the Na^+ ions are in more exposed and thus more easily displaced (Anderson, et al. 1999).

Table 4-2 shows the calculated atomic ratios for the ETS-10 samples from the same EDX data. Comparing the atomic ratios gives a representation of the relative changes in elemental composition as a result of ion exchange between the different samples. The structure of polymorph B of ETS-10 which was solved by

Table 4-1. Atomic percent by element for various ETS-10 samples obtained from EDX analysis

Adsorbent	Atomic Percent with 95% Confidence Interval					
	Si	**Ti**	**Na**	**Ca**	**K**	**O**
Na-ETS-10 A	18.96 ±1.31	5.07 ±0.26	6.59 ±0.71	-	1.91 ±0.10	67.29 ±13.02
Na-ETS-10 B	19.31 ±1.31	5.15 ±0.26	6.27 ±0.71	-	2.18 ±0.10	66.99 ±12.56
Na-ETS-10 C	19.21 ±1.31	5.07 ±0.26	6.36 ±0.71	-	2.02 ±0.10	67.2 ±12.78
Ca-ETS-10 A	18.88 ±1.33	5.79 ±0.29	2.82 ±0.37	3.16 ±0.18	1.39 ±0.10	67.95 ±13.66
Ca-ETS-10 B	16.63 ±1.23	5.51 ±0.29	2.03 ±0.29	3.38 ±0.21	1.42 ±0.11	71.03 ±14.88
Ca-ETS-10 C	21.34 ±1.66	5.55 ±0.31	2.75 ±0.39	3.20 ±0.2	1.22 ±0.10	65.94 ±14.89
Ca/H-ETS-10 A	24.89 ±1.88	6.29 ±0.33	1.16 ±0.20	2.20 ±0.15	1.45 ±0.11	64.01 ±14.36
Ca/H-ETS-10 B	17.62 ±1.28	5.64 ±0.29	0.98 ±0.16	1.97 ±0.13	1.50 ±0.10	72.28 ±14.61
Ca/H-ETS-10 C	21.18 ±1.63	5.50 ±0.30	0.74 ±.015	2.05 ±0.14	1.42 ±0.11	69.11 ±15.18

Table 4-2. Relevant atomic ratios for various ETS-10 samples calculated from EDX results

Adsorbent	Atomic Ratios with 95% Confidence Intervals				Total Charge:Ti
	Si:Ti	Na:Ti	Ca:Ti	K:Ti	
Na-ETS-10 A	3.73±0.32	1.30±0.15	-	0.38±0.03	1.68±0.15
Na-ETS-10 B	3.75±0.32	1.22±0.15	-	0.42±0.03	1.64±0.15
Na-ETS-10 C	3.79±0.32	1.25±0.15	-	0.40±0.03	1.65±0.15
Ca-ETS-10 A	3.26±0.28	0.49±0.07	0.55±0.04	0.24±0.02	1.83±0.11
Ca-ETS-10 B	3.02±0.28	0.26±0.02	0.61±0.05	0.37±0.06	1.85±0.12
Ca-ETS-10 C	3.85±0.37	0.50±0.07	0.58±0.05	0.22±0.02	1.88±0.12
Ca/H-ETS-10 A	3.96±0.37	0.23±0.02	0.35±0.03	0.18±0.03	1.11±0.07
Ca/H-ETS-10 B	3.12±0.28	0.27±0.02	0.35±0.03	0.17±0.03	1.14±0.07
Ca/H-ETS-10 C	3.85±0.36	0.26±0.02	0.37±0.03	0.13±0.03	1.13±0.07

Anderson gives a theoretical Si:Ti ratio of 5 (Anderson, et al. 1999). Though the experimentally gathered Si:Ti ratios do not match with this theoretical value, the Si:Ti ratio for Na-ETS-10, Ca-ETS-10 points A and C, and Ca/H-ETS points A and C agree within error with the range of Si:Ti ratios from 3.5 to 10 outlined by Kuznicki for ETS-10 (Kuznicki, 1989). Others have reported ETS-4 with a Si:Ti ratio of 2.4 or lower (Pavel, et al. 2002). This is relevant because for EDX analysis, large particle clusters were used as the focal point for analysis. It is likely based on the crystal morphology that these large clusters contained some

particles of ETS-4. The presence of ETS-4 would account for the lower Si:Ti ratio values obtained via EDX analysis. The presence of ETS-4 as an impurity phase was verified by XRD and SEM.

The cation to metal ratios (Na:Ti, Ca:Ti) can be examined to determine the degree and type of ion exchange. In the Ca-ETS-10 sample a significant decrease in the Na:Ti ratio is seen, and the presence of calcium is now observed. However, the charge equivalents before and after the exchange do add to the expected value of 2 and the cation content of the Ca-ETS-10 appearing to exceed that of the Na-ETS-10. One possible explanation for this is the presence of H^+ ions in addition to the K^+ and Na^+ cations in the as-synthesized Na-ETS-10. These protons would have exchanged in during the washing of the Na-ETS-10 after synthesis.

Theoretically to balance the net negative charge of the TiO_6^{2-} octahedra, a net 2+ charge is necessary. For the sodium form of ETS-10 this means that in addition to the Na^+ and K^+ cations there are likely H^+ cations as well, as no other cations are present in significant quantities in the synthesis mixture. For as-synthesized Na-ETS-10 the H:Ti ratio is calculated to be ~0.34. After calcium exchange, the H:Ti ratio becomes ~0.15, dropping along with the other monovalent cations as they are exchanged out. In the mixed ion Ca/H-ETS-10 the H:Ti ratio is ~0.87. These results suggest that the ion affinity of ETS-10 follows the trend of $Ca^{2+} > H^+ > Na^+ / K^+$. This ion affinity trend agrees with sources in literature which note ETS-10 to have a strong affinity for divalent cations and for protons (Nak, et al. 2009) (Lv, Tsoi and Zhao 2004) (Camarinha, et al. 2009).

4.1.4 Surface Area and Pore Volume

Nitrogen adsorption/desorption isotherms were obtained to determine the pore volume and surface areas for the various adsorbents. These results are presented in Table 4-3. Zeolite 4A samples were not analyzed as nitrogen is unable to access the zeolite 4A pores at the 77K experimental conditions. Silica gel and alumina sample surface areas were calculated via the BET method surface area, while for the ETS-10 samples the Langmuir method was used. The different methods for calculating surface areas were used to reflect the different nitrogen adsorption behaviour of the various materials. To determine the pore volume, micropore and external surface areas the deBoer t-plots method was used. In the case of alumina no micropores were observed using the deBoer t-plots method. However, activated alumina is known to be microporous and capable of adsorbing carbon dioxide and water molecules. This implies that the pore size of the activated alumina is less than 3.7Å (the size of a nitrogen molecule) and that

Table 4-3. Surface areas and pore volumes of adsorbent samples

Adsorbent	**Total Surface Area (m^2/g)**	**Micropore Volume (cc/g)**	**Micropore Area (m^2/g)**	**External Surface Area (m^2/g)**
Silica Gel	677.9±9.8	0.0854	171.5	506.4
Alumina	178.1±0.5	-	-	178.1
Na-ETS-10	389.8±0.5	0.1327	341.6	48.85
Ca-ETS-10	380.1±0.1	0.1214	336.4	43.7
Ca/H-ETS-10	392.7±0.2	0.1249	348.2	44.4

the nitrogen was unable to enter the pores. (Kaye & Laby Online 1995). The surface areas and pore volumes of the various ETS-10 samples are relatively consistent since ion exchange should not affect these properties.

4.1.5 Bulk Density

The bulk densities of the adsorbent pellets were measured using the procedure previously outlined. The values obtained are shown in Table 4-4. These values will later be used to determine the moisture capacity per unit of volume of adsorbent. The moisture capacity per unit volume of adsorbent is a useful metric in that it allows for more fair comparison of the performance of a fixed-volume adsorbent bed. Adsorbents with higher volumetric capacity are preferred. The bulk density of the laboratory grade alumina pellets was not measured as the purpose of the comparison is to compare the new materials to commercial grade desiccant materials.

Table 4-4. Adsorbent bulk densities

Adsorbent	**Silica Gel**	**Zeolite 4A**	**Na-ETS-10**	**Ca-ETS-10**	**Ca/H-ETS-10**
Density (g/cc)	0.73±0.04	0.81±0.06	0.74±0.07	0.74±0.06	0.69±0.06

4.2 Commissioning and Validation

As the carbon dioxide drying experimental apparatus was designed and fabricated by the author several commissioning runs were carried out to verify and validate the process inputs and outputs. The results of these commissioning runs were compared to literature data in order to validate the operation of the system and readings of the instruments.

Figure 4-13 shows the moisture breakthrough profiles for the silica gel commissioning runs. The commissioning experiments were carried out with a total carbon dioxide flow rate of 500 sccm, adsorption temperature of 20°C, and ambient pressure on the column exhaust. The bed was regenerated for 12 hours at 60°C between runs using building-supplied compressed air at a flow rate of 500 sccm. The general pattern of the breakthrough times was compared to the literature water adsorption isotherm for silica gel shown in Figure 4-14. For this comparison the trend in breakthrough time with carbon dioxide stream humidity was compared to the shape of the literature water adsorption isotherm. For silica gel, the breakthrough times decreased linearly with increasing levels of humidity, which correlates to the isotherm showing increased capacity at higher levels of humidity. The actual capacities do not match between the commissioning breakthrough and the isotherm. For example, for the 100% relative humidity breakthrough run, the bed capacity was calculated to be 0.0819 g H_2O/ g adsorbent. At 20°C and one atmosphere pressure a relative humidity of 100% corresponds to a moisture content of 23,729 ppm or 2.404 kPa partial pressure. On the isotherm these conditions correspond to a capacity of ~11 mol/kg or

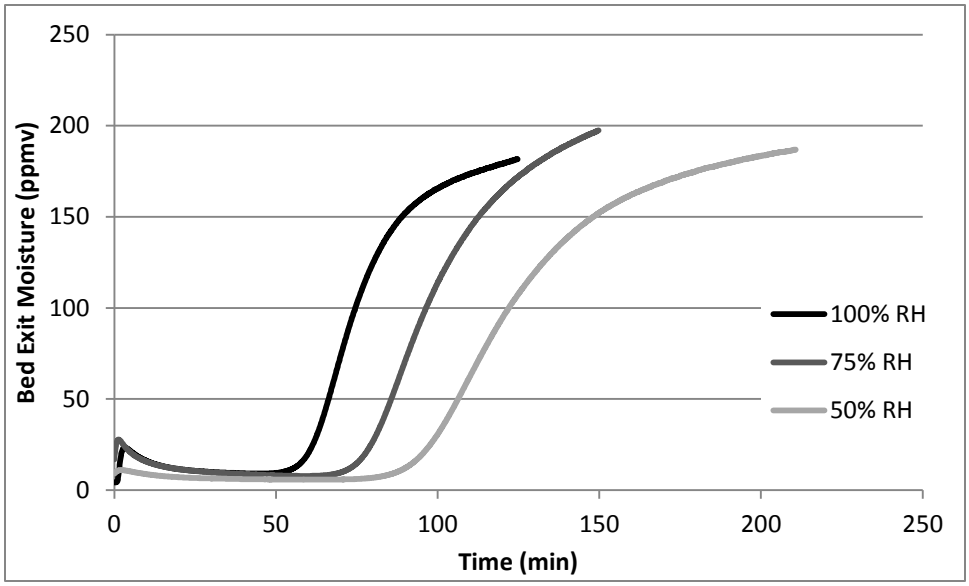

Figure 4-13. Bed exit moisture breakthrough profiles for silica gel commissioning runs

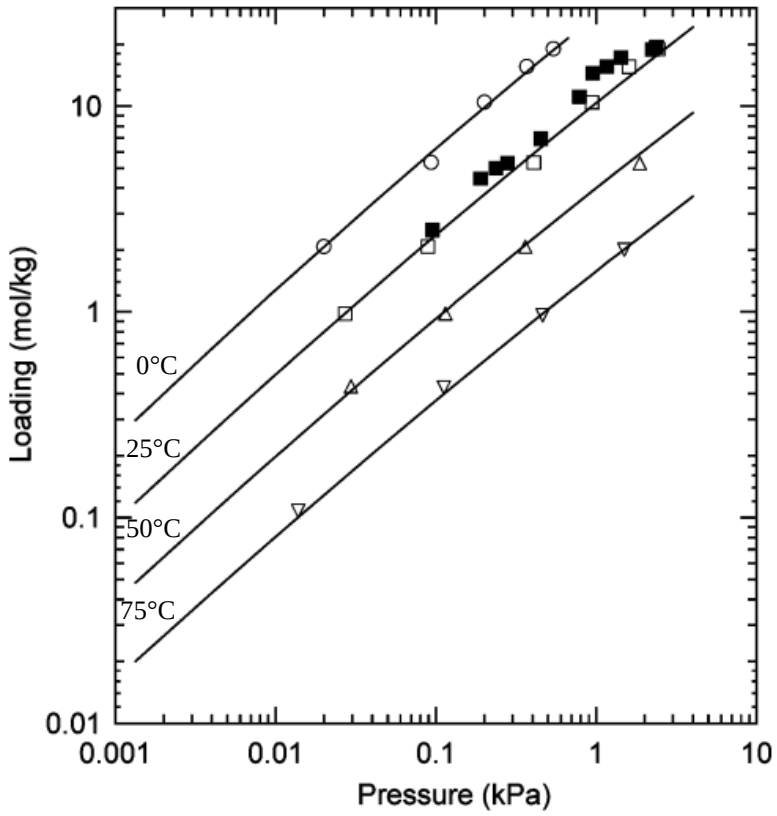

Figure 4-14. Adsorption isotherms of water on silica gel **(**Wang and LeVan 2009**)**

~0.2 g H2O/ g adsorbent. This difference is due to the isotherm capacity being the capacity when the adsorbent is *at equilibrium* with its humid surrounding, whereas the breakthrough capacity is calculated when the moisture front reaches a specified level. For the purpose of these experiments, the breakthrough capacity was calculated when the dewpoint sensor at the exhaust of the bed first recorded an increase humidity. The capacity for silica gel is linear at low pressures and, at the specified breakthrough conditions, the adsorbent has little capacity for moisture and will breakthrough well before the majority of the bed is saturated with water vapour. Because the bed has not yet reached equilibrium the capacity calculated through the breakthrough experiment will not match that predicted by the isotherm.

A similar comparison was made using alumina and the breakthroughs for test experiments are shown in Figure 4-15 and the literature water adsorption isotherm for alumina shown in Figure 4-16. For these commissioning experiments a total carbon dioxide flow rate of 500 sccm, an adsorption temperature of 20°C, and ambient pressure were used. The bed was regenerated at 60°C under a 500 sccm flow of building-supplied compressed air for 12 hours. Similar to the silica gel commissioning experiments the general pattern of the isotherm is mirrored by the trend in breakthrough times (and thus capacity). Once again the experimental breakthrough capacity differs in value from what the isotherm would predict and for the same reasons. In addition, the surface area of the activated alumina used in the commissioning adsorption experiment is much lower than that used for the

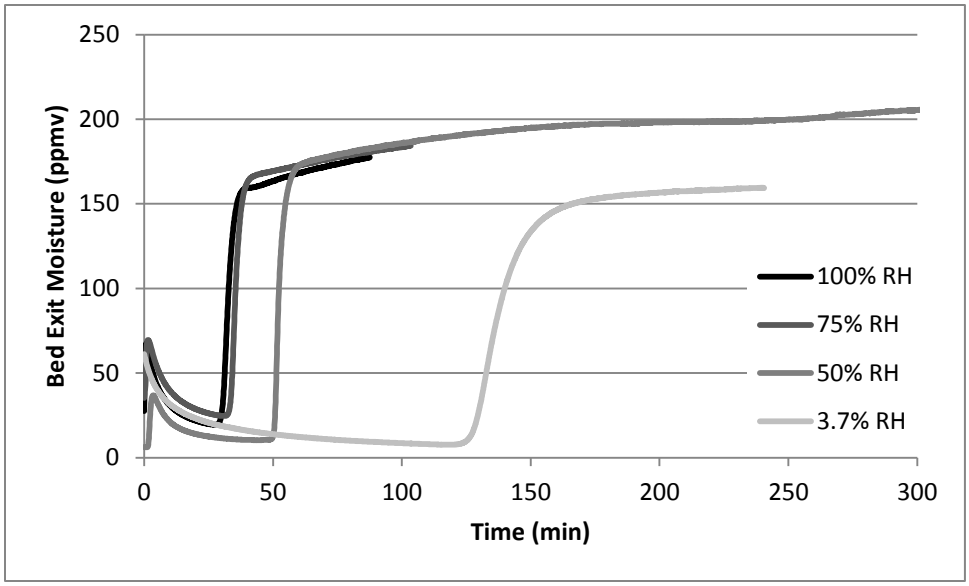

Figure 4-15. Bed exit moisture breakthrough profiles for alumina commissioning runs

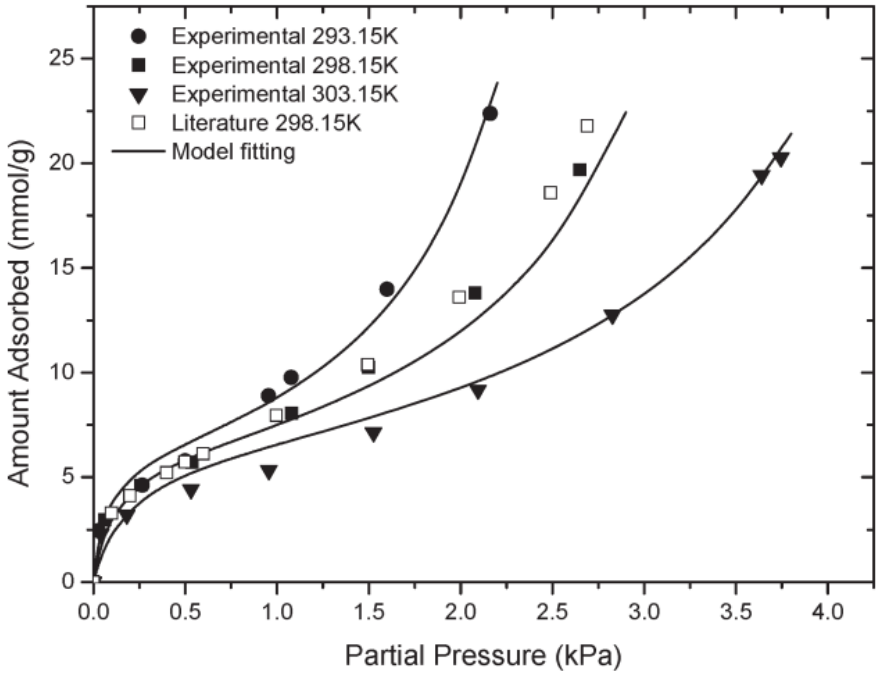

Figure 4-16. Water adsorption isotherms on activated alumina (Li, Xiao and Webley 2009)

experiments to obtain the isotherm (366.8 m^2/g) (Li, Xiao and Webley 2009) and thus only a qualitative comparison between data sets can be made.

Alumina and silica were chosen for these commissioning experiments because they exhibit different adsorptive behaviours, as can be seen in Figure 4-17 which overlays their respective water adsorption isotherms. Silica gel has a linear water adsorption isotherm where loading increases with pressure, while the water isotherm for activated alumina can be classified as type 2. The difference in the breakthrough response and the fact that the breakthrough responses mimic the general trend of the adsorption isotherms were expected results which indicate that the experimental system will differentiate between adsorbents and provide useful data.

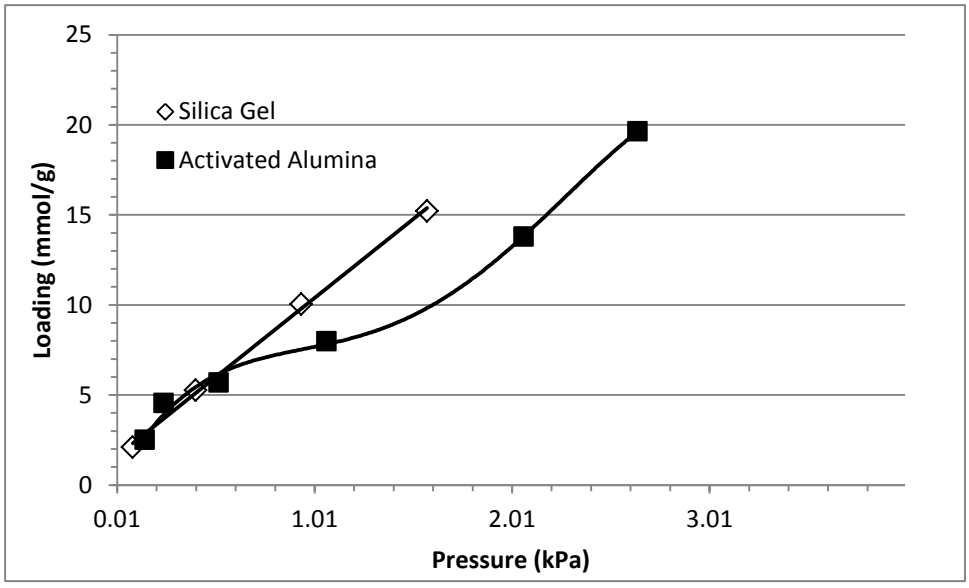

Figure 4-17. Water adsorption isotherms at 25°C for silica gel and activated alumina

4.2.1 Regeneration Air Humidity

As another part of the unit commissioning and test method validation the impact of regeneration air humidity was investigated. Figure 4-18 shows the effect on bed moisture capacity for zeolite 4A and Ca-ETS-10 by switching the regeneration gas from dry, compressed air to ambient, "wet" air. The experiments were run using a feed stream humidity of 100% RH carbon dioxide and one hour regeneration time. Other than the regeneration air stream humidity, the conditions for the experiments were kept the same. The building compressed air had a measured humidity of 46 ppmv while the ambient air humidity was between 3100 ppmv and 4100 ppmv. In all cases, the moisture capacity of the adsorbent bed was lower when using ambient air for regeneration. Silica gel appears to be the adsorbent most affected by the regeneration stream humidity while Ca-ETS-10 appears to be the least sensitive. The sensitivity of silica gels capacity to moisture

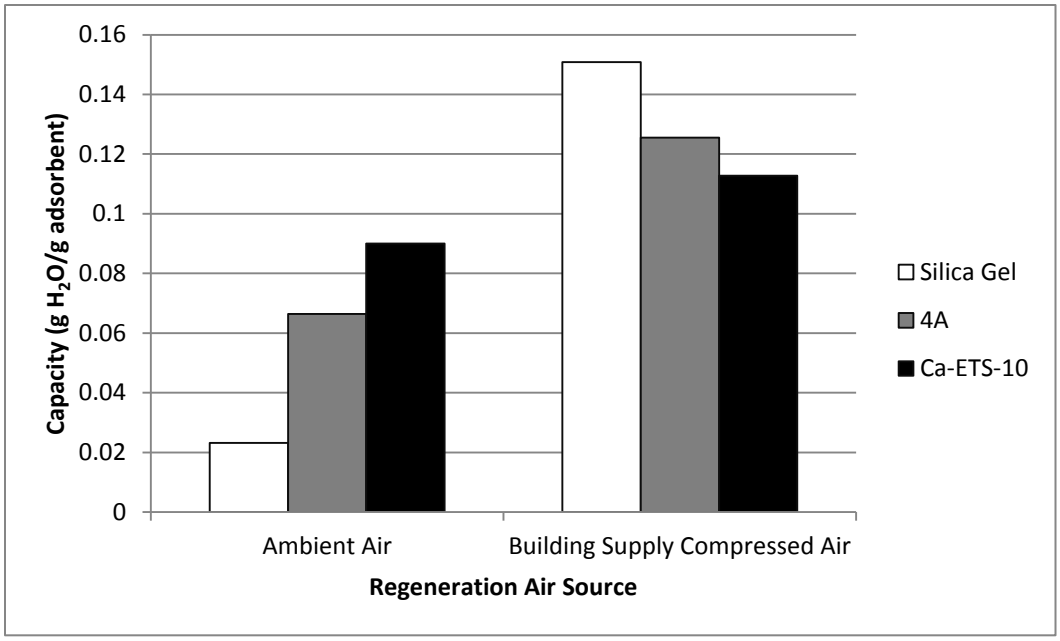

Figure 4-18. Moisture breakthrough capacity for several adsorbents using different regeneration air sources with a 100% RH CO_2 feed stream

in the regeneration stream can be explained by silica gel's low capacity at low moisture levels. A moist ambient air regeneration stream results in more adsorbed water being present after regeneration. The adsorbed water will occupy the strongest and most selective adsorption sites, thereby lowering the breakthrough capacity. For zeolite 4A the reduction in breakthrough capacity is due to the small difference in the equilibrium capacity between the adsorption and regeneration temperatures. During regeneration of zeolite 4A a portion of the driving force is the partial pressure of moisture in the gas phase, which is increased by having moisture in the regeneration stream. This also applies to silica gel, though to a lesser extent. The relative insensitivity of Ca-ETS-10 to moisture in the regeneration air stream is due to Ca-ETS-10's equilibrium capacity dropping significantly once the temperature reaches 70°C. This means that even if moisture is present in the regeneration stream it is unable to adsorb. The small reduction in capacity can be attributed to moisture from the regeneration stream being adsorbed once the bed was isolated to cool down between desorption and adsorption phases of the cycle.

4.3 Carbon Dioxide Drying Experiments

4.3.1 Breakthrough Capacities

Five different adsorbents were studied for carbon dioxide drying experiments: silica gel, zeolite 4A, Na-ETS-10, Ca-ETS-10, and Ca/H-ETS-10. The breakthrough experiments used a carbon dioxide flow rate of 500 sccm. The adsorption temperature was kept constant at 30°C to maintain a controllable, near-ambient condition. The bed regeneration conditions were set at a bed temperature of 70°C, with ambient room air used at a flow rate of 500 sccm. The regeneration time was set to one hour. The regeneration temperature was selected to compare the performance of the adsorbents using low grade heat for regeneration, such as the waste heat available from low pressure steam at a power plant. The performance of each adsorbent was assessed using a CO_2 inlet feed having a moisture content of 50, 75, and 100 percent relative humidity. Data points were collected once every five seconds throughout the experiments. These conditions were used for all adsorbents and all carbon dioxide stream humidities.

In order to ensure the consistency of data collected, replicate runs were performed for each set of experimental conditions. An example breakthrough profile for the experimental runs using silica gel at 100% RH is shown as Figure 4-19. The breakthrough point is indicated on the figure by the black line. The initial rise in bed exit moisture is an artifact created by residual moisture from the regeneration phase of the cycle remaining in the adsorbent bed. After this pulse of moisture, the sensor dries out as carbon dioxide dried by the adsorbent bed flows past, reducing the bed exit moisture continues to drop until the breakthrough.

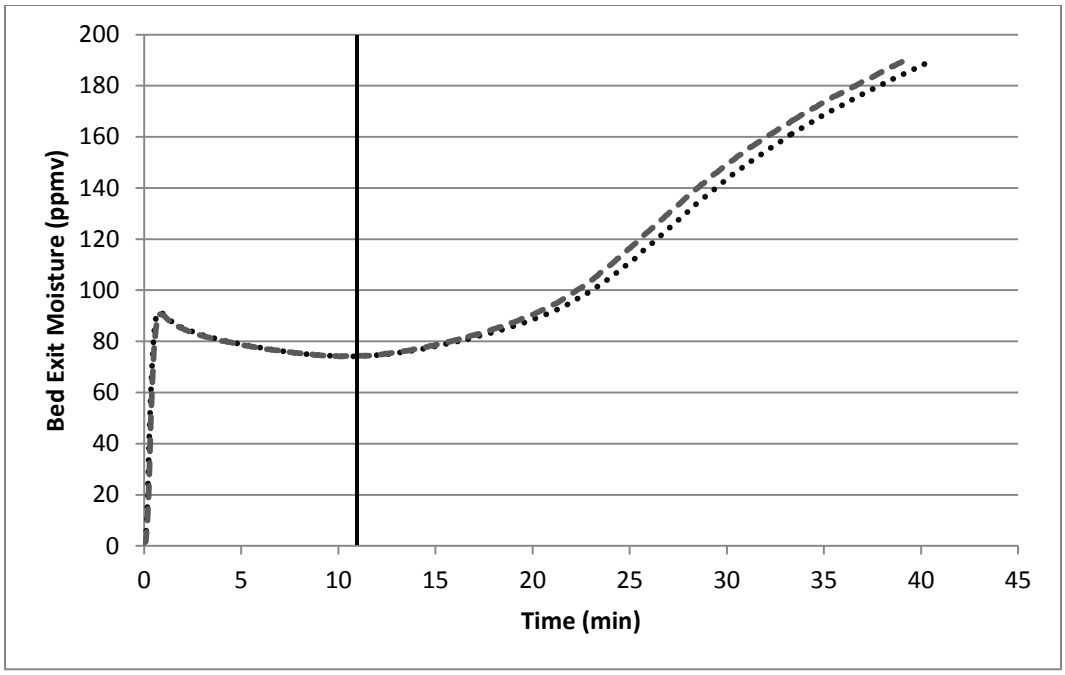

Figure 4-19. Moisture breakthrough profiles for silica gel bed with 100% RH CO_2 feed stream

After moisture breakthrough the bed exit moisture continues to increase until the experiment ends. If left to run long enough it the bed exit moisture would eventually equilibrate with the feed stream moisture.

From the breakthrough profiles, the average bed breakthrough capacities were calculated on a mass H_2O per mass adsorbent basis. Figure 4-20 shows the breakthrough capacities for silica gel, Figure 4-21 shows the breakthrough capacities for zeolite 4A, Figure 4-22 shows the breakthrough capacities for Na-ETS-10, Figure 4-23 shows the breakthrough capacities for Ca-ETS-10, and Figure 4-24 shows the breakthrough capacities for Ca/H-ETS-10. Several

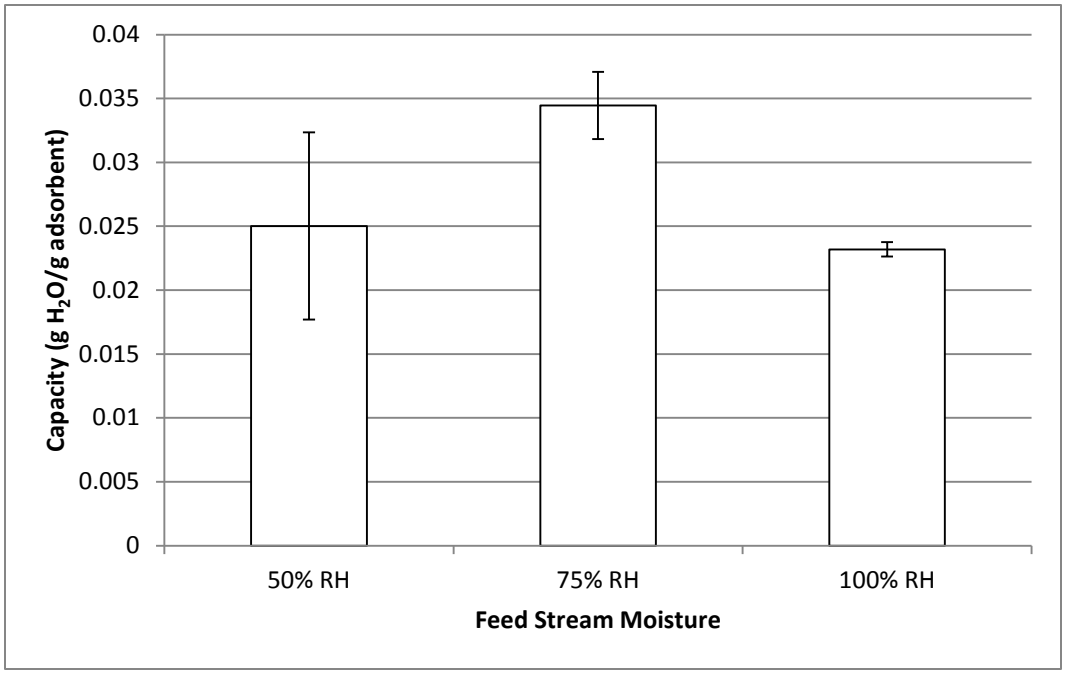

Figure 4-20. Silica gel moisture capacities and 95% confidence intervals at various CO_2 feed stream humidities

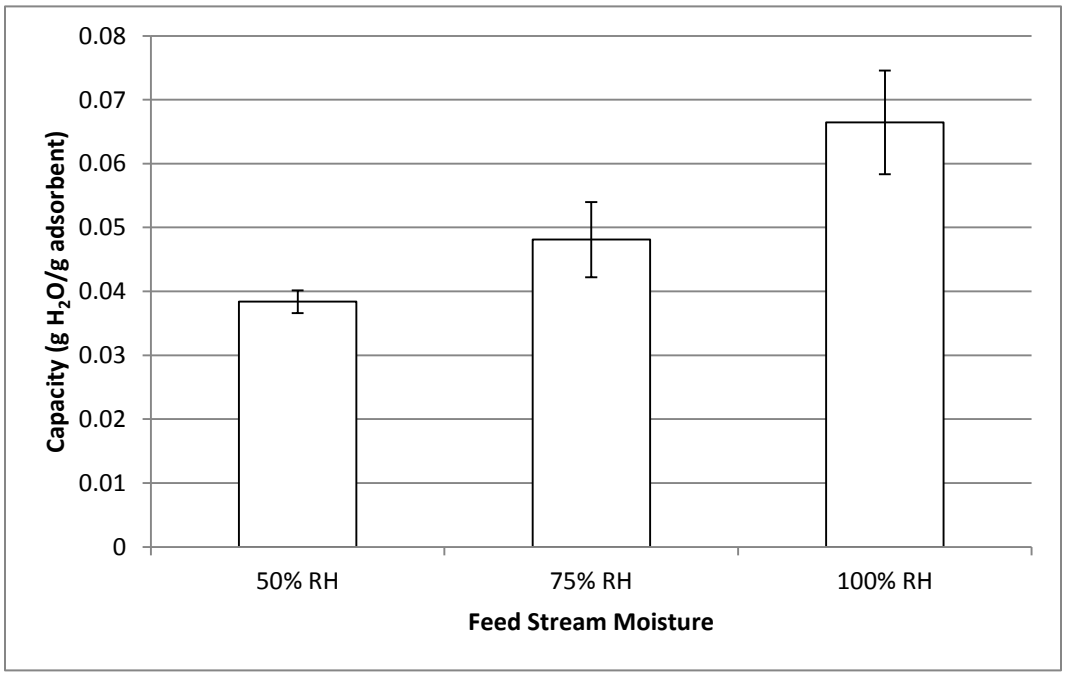

Figure 4-21. Zeolite 4A moisture capacities and 95% confidence intervals at various CO_2 feed stream humidities

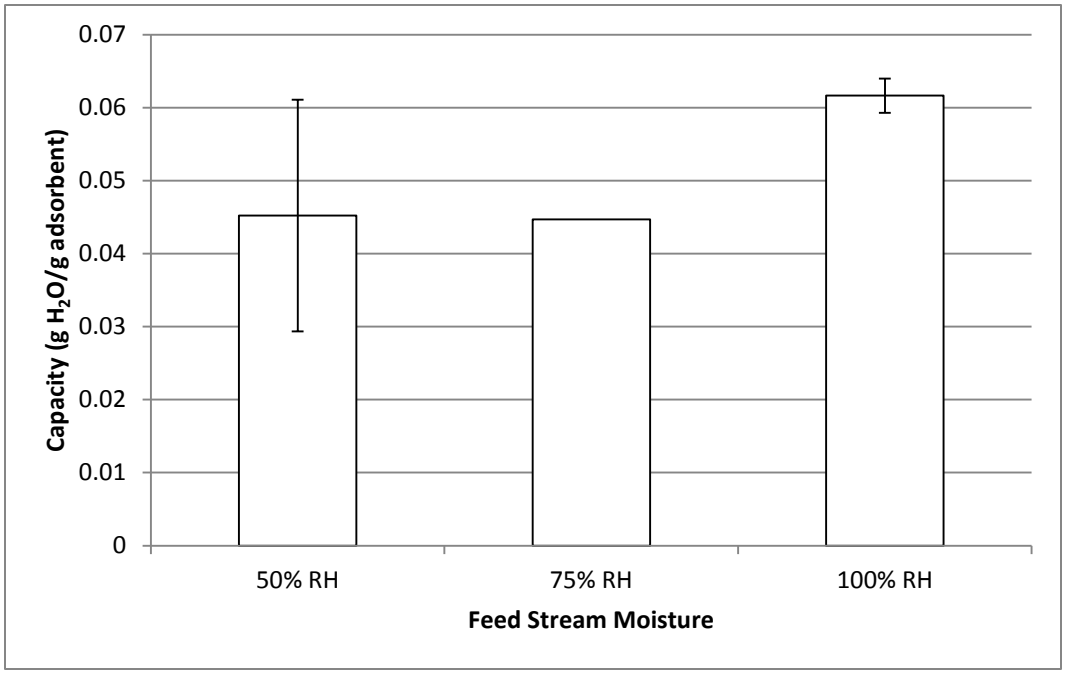

Figure 4-22. Na-ETS-10 moisture capacities and 95% confidence intervals at various CO_2 feed stream humidities

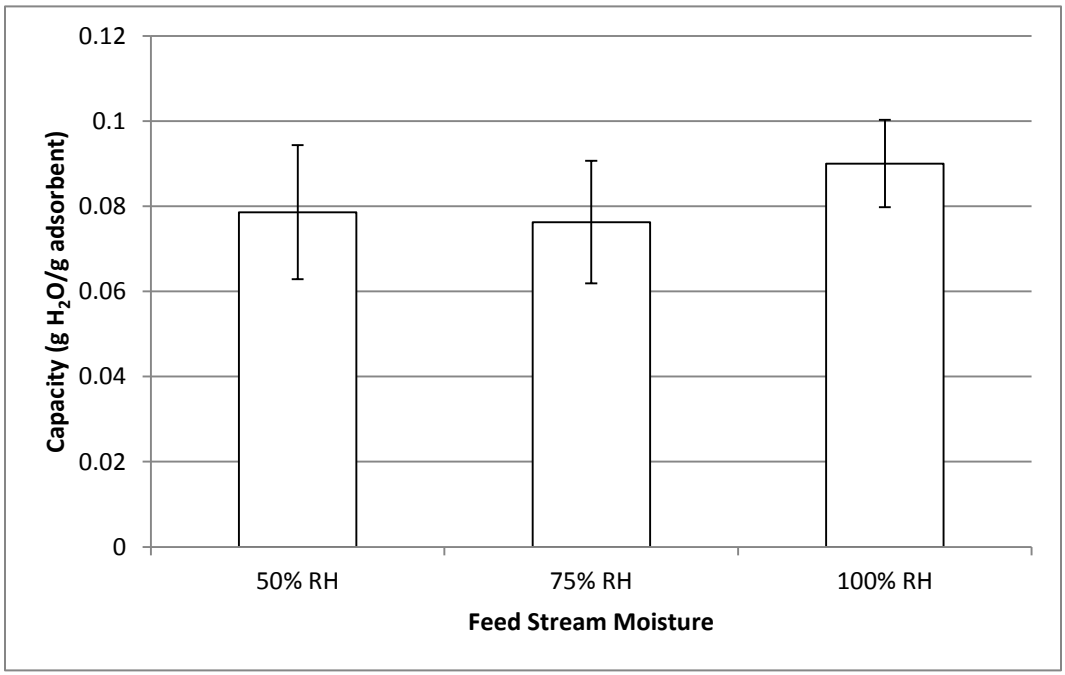

Figure 4-23. Ca-ETS-10 moisture capacities and 95% confidence intervals at various CO_2 feed stream humidities

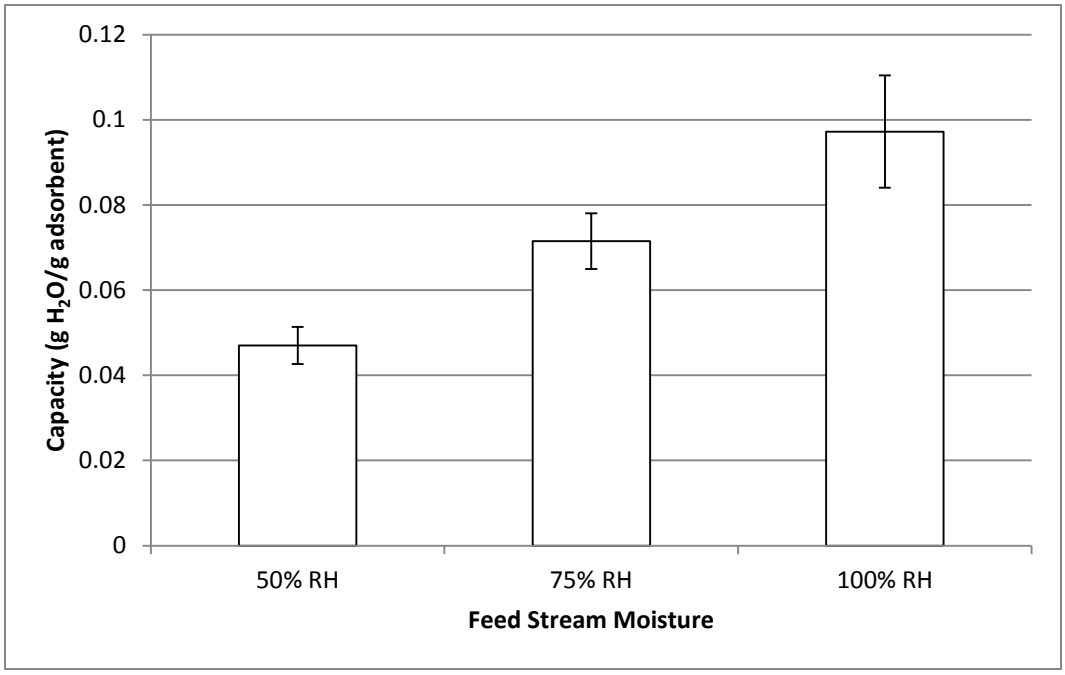

Figure 4-24. Ca/H-ETS-10 moisture capacities and 95% confidence intervals at various CO_2 feed stream humidities

different results can be drawn from these figures. The breakthrough capacity for the Ca-ETS-10 bed appears to have little dependence on the feed stream humidity. The zeolite 4A, Na-ETS-10, and Ca/H-ETS-10 beds show increasing moisture adsorption capacity as the humidity of the CO_2 stream increases. It was expected that the breakthrough capacity of zeolite 4A and the ETS-10 materials would remain constant as the feed stream moisture content increased, similar to the result obtained for Ca-ETS-10, since the water adsorption isotherm for these adsorbents shows an essentially constant equilibrium water capacity at the humidity range investigated. The increased capacity with increasing humidity would be expected if the feed stream moisture level was low enough to have moved out of the rectangular region of the adsorption isotherm. However at 30°C the 50%-100% RH range places the conditions of the experiment within the

rectangular region of these adsorbents water adsorption isotherm. One possible explanation for these results is that for 4A, Na-ETS-10, and Ca/H-ETS-10 the bed length is not long enough for the mass transfer front to fully develop under the experimental conditions, leading to breakthrough before any portion of the bed is fully saturated. In this situation an increased initial concentration can lead to higher capacity. The high fraction of divalent Ca^{2+} cations in Ca-ETS-10 while 4A, Na-ETS-10, and Ca/H-ETS-10 all have a high amount of monovalent cations present may also be a factor that influences water adsorption and moisture breakthrough.

The 95% confidence intervals are also shown in the figures. The uncertainty, for some of the experiments, such as for silica gel with a 50% RH feed stream, is quite large. The most likely explanation for this variability is changes in the humidity of the ambient air used for regeneration. The data sets with a larger variability in moisture capacity measurements also had a higher degree of variability in the recorded ambient air humidity. Increasing moisture in the regeneration air stream correlates to a decrease in bed moisture capacity, as shown for Ca-ETS-10 at 75% RH in Figure 4-25. Though Ca-ETS-10 was shown, in commissioning, to be less affected by moisture in the regeneration air stream than zeolite 4A or silica gel, an effect is still measureable.

Table 4-5 shows the adsorbents sorted from highest to lowest average breakthrough capacity at each of the CO_2 feed stream humidities. At a 50% RH CO_2 feed stream Ca-ETS-10 has a capacity twice that of zeolite 4A. At a 75% RH CO_2 feed stream Ca-ETS-10 still has the highest breakthrough capacity but

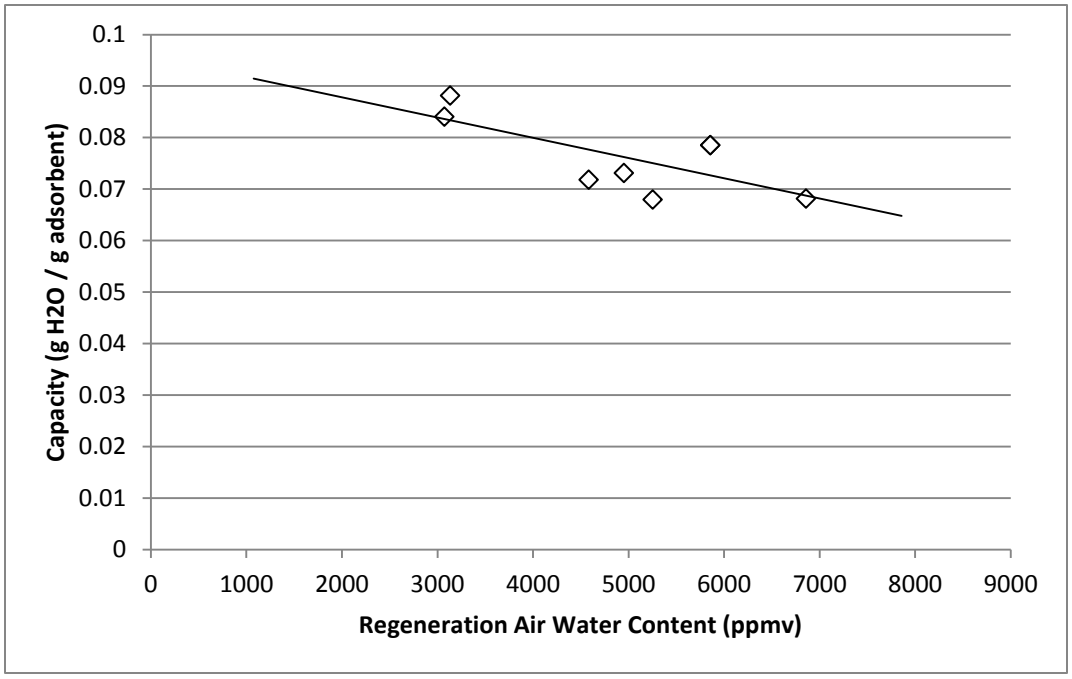

Figure 4-25. Breakthrough capacity of Ca-ETS-10 as a function of regeneration air humidity

Table 4-5. Adsorbents sorted by average capacity from highest to lowest at all CO_2 feed stream humidities

Capacity (g_{H2O} / $g_{adsorbent}$)					
Adsorbent	**50% RH**	**Adsorbent**	**75% RH**	**Adsorbent**	**100 % RH**
Ca-ETS-10	0.0786	**Ca-ETS-10**	0.0763	**Ca/H-ETS-10**	0.0972
Ca/H-ETS-10	0.0470	**Ca/H-ETS-10**	0.0715	**Ca-ETS-10**	0.0900
Na-ETS-10	0.0452	**Zeolite 4A**	0.0481	**Zeolite 4A**	0.0665
Zeolite 4A	0.0384	**Na-ETS-10**	0.0447	**Na-ETS-10**	0.0616
Silica	0.0250	**Silica**	0.0344	**Silica**	0.0232

now comparable to the capacity of Ca/H-ETS-10. The capacity of zeolite 4A is noticeably lower. At a feed stream humidity of 100% RH Ca/H-ETS-10 now has the highest breakthrough capacity. The breakthrough capacity of Ca-ETS-10 is similar to that of Ca/H-ETS-10 with the capacity of zeolite 4A noticeably lower than both of these ETS-10 adsorbents.

The breakthrough capacities can also be examined on a capacity per unit volume of adsorbent basis (g H_2O adsorbed per cc adsorbent). Table 4-6 shows the adsorbents sorted by average breakthrough capacity per unit volume of adsorbent similar to Table 4-5. This comparison of breakthrough capacities is relevant because the adsorbent bed volume is a major factor in determining the capital cost of an adsorptive gas separation unit. On a capacity per unit volume basis Ca-ETS-10 has the highest capacity for both 50% RH and 75% RH CO_2 feed streams. For the 50% RH CO_2 feed this is noticeably higher than Na-ETS-10, the second

Table 4-6. Adsorbents sorted by average capacity (g_{H2O} / $cc_{adsorbent}$) from highest to lowest at all CO_2 feed stream humidities

50% RH		**75% RH**		**100 % RH**	
Adsorbent	**Capacity**	**Adsorbent**	**Capacity**	**Adsorbent**	**Capacity**
Ca-ETS-10	0.0582	**Ca-ETS-10**	0.0564	**Ca/H-ETS-10**	0.0671
Na-ETS-10	0.0335	**Ca/H-ETS-10**	0.0493	**Ca-ETS-10**	0.0666
Ca/H-ETS-10	0.0324	**Zeolite 4A**	0.0390	**Zeolite 4A**	0.0538
Zeolite 4A	0.0311	**Na-ETS-10**	0.0331	**Na-ETS-10**	0.0456
Silica	0.0183	**Silica**	0.0251	**Silica**	0.0169

highest capacity adsorbent, and the capacity of zeolite 4A. For the 75% RH CO_2 feed Ca/H-ETS-10's breakthrough capacity is close to that of Ca-ETS-10. The capacity of zeolite 4A is still noticeably lower than that of Ca-ETS-10 and Ca/H-ETS-10. At 100% RH in the CO_2 feed stream, Ca/H-ETS-10 and Ca-ETS-10 have approximately the same breakthrough capacity, higher than that of the other adsorbents.

The consistently low breakthrough capacity of silica gel is due to its relatively low affinity for moisture when compared to the other adsorbents. This gives it a low equilibrium capacity at low inlet levels of moisture, allowing ppm levels of moisture to easily breakthrough. The breakthrough capacity of zeolite 4A follows a similar trend to that of Na-ETS-10 and Ca/H-ETS-10. The rate of increase is different for the three adsorbents with the breakthrough capacity of Ca/H-ETS-10 increasing the most with increasing feed stream humidity, followed by zeolite 4A, with Na-ETS-10 increasing the least. This may imply that Na-ETS-10 is the closest to fully developing a mass transfer front and thus is less affected by the increasing moisture content.

4.3.2 Carbon Dioxide Recovery

An important performance metric used to compare separations is the recovery of the product, or the amount of target gas produced divided by the amount of target gas fed to the system. In these breakthrough experiments the dry carbon dioxide exiting the system can be considered the product stream. The recoveries for the various breakthrough experiments are shown in Table 4-7. For all the adsorbents

investigated the recovery is greater than 95%. This high level of recovery was expected, since the only carbon dioxide losses that occur are the initial few seconds of flow where the moisture pulse occurs, the void volume of the bed, and the small fraction of carbon dioxide which is adsorbed by the desiccant pellets. The high selectivity of the adsorbents for water over carbon dioxide also contributes to the high recovery rate.

Table 4-7. Percent recovery of carbon dioxide at moisture breakthrough for various adsorbents at several CO_2 feed stream humidities

Adsorbent	**Percent Recovery at Several CO_2 Feed Stream Humidities**		
	50% RH	**75% RH**	**100 % RH**
Silica	95.8±1.1	95.4±0.1	95.5±0.9
Zeolite 4A	97.4±0.2	98.5±2.5	96.6±0.6
Na-ETS-10	98.2±1.3	96.9±1.2	96.1±0.5
Ca-ETS-10	99.1±0.6	98.1±0.9	97.4±0.4
Ca/H-ETS-10	97.9±0.1	98.1±0.2	97.5±0.6

4.4 Conclusions

The XRD and SEM data indicate that the structure of the Ca-ETS-10 and Ca/H-ETS-10 adsorbent samples are unaffected by the ion exchange procedure. From the EDX results an ion affinity of $Ca^{2+} > H^{+} > Na^{+} / K^{+}$ can be observed for ETS-10. The humidity of the regeneration air stream has been observed to be an important process variable and has been identified as a cause of variance in the measured breakthrough capacities. Ca-ETS-10 has a notably lower sensitivity to moisture in the regeneration air stream than either silica or zeolite 4A. Data indicates that all adsorbents provide a high recovery of carbon dioxide. At the conditions investigated the breakthrough capacity of Ca-ETS-10 was highest across all feed stream humidities, with Ca/H-ETS-10 having a comparable breakthrough capacity at 100% RH. On both gravimetric and volumetric bases for breakthrough capacity measurement Ca-ETS-10 and Ca/H-ETS-10 show higher breakthrough capacity than either zeolite 4A or silica gel. The relative insensitivity of ETS-10 towards humidity in the regeneration stream allows it to be used without pre-drying the stream. The high CO_2 recovery of an adsorptive separation system coupled with the performance advantages of ETS-10 makes such system an attractive alternative to solvent-based absorption systems. The ability to utilize ambient, humid air and waste heat sources for regeneration indicates these desiccants may be usable on a wide range of streams.

4.5 Future Work

There are several areas of this project which should be the subject of further investigation, the majority of them focused on optimizing the design of a low energy input regeneration ETS-10 based TSA drying cycle. The limiting drying level achieved by the various ion forms of ETS-10 should be assessed. This can be done using the existing testing apparatus, using a longer blow down to zero the dewpoint sensor. These initial adsorbent screening tests did not demand the sensor be fully zeroed before each cycle, but it should be conducted as the next step in this project.

One step in the optimization is gaining a better understanding of the regeneration conditions for Ca- and Ca/H-ETS-10. In this study, regeneration time and temperature were taken as fixed parameters to allow for a comparison between desiccants. However, further work should be done to describe the water desorption behavior from the ETS-10 desiccants as a function of regeneration time and regeneration temperature coupled with the flow rate of the regeneration gas stream. Some previous work has been done exploring the use of microwaves to provide energy for the regeneration of Na-ETS-10 for ethane/ethylene and carbon dioxide/methane separations (Chowdhury, Shi, Hashisho, Sawada, & Kuznicki, 2012). This technique could be applied to the regeneration of ETS-10 desiccants and could prove to be more efficient than other types of regeneration.

The impact of varying the feed stream flow rate should also be explored to optimize the moisture capacity by matching the space velocity of the gas to the mass transport properties of the adsorbent bed system.

In addition investigating ways to optimize a TSA cycle, effort should be focussed on forming particles of ETS-10 with enhances durability. Finding a binder that can be paired with ETS-10 to form strong macroscopic particles while preserving the properties drying capacity and other behaviours described in this study is another key ingredient to moving this project forward. Once effective particles have been formed, it will be possible to operate TSA test cycles using a larger sized bed.

6. References

Al-Baghli, N. A., & Loughlin, K. F. (2006). Binary and Ternary Adsorption of Methane, Ethane, and Ethylene on Titanosilicate ETS-10 Zeolite. *Journal of Chemical Engineering Data, 51*, 248-254.

Anderson, M. W., Agger, J. R., Luigi, D.-P., Baggaley, A. K., & Rocha, J. (1999). Cation sites in ETS-10: 23Na 3Q MAS NMR and lattice energy minimization calculations. *Physical Chemistry Chemical Physics*, 2287-2292.

Anson, A., Kuznicki, S. M., Kuznicki, T., Haastrup, T., Wang, Y., Lin, C. C., et al. (2008). Adsorption of argon, oxygen, and nitrogen on silver exchanged ETS-10 molecular sieve. *Microporous and Mesoporous Materials, 109*, 577-580.

Anson, A., Wang, Y., Lin, C. C., Kuznicki, T. M., & Kuznicki, S. M. (2008). Adsorption of ethane and ethylene on modified ETS-10. *Chemical Engineering Science, 63*, 4171-4175.

Arean, C. O., & Delgado, M. R. (2010). Variable-temperature FT-IR studies on the thermodynamics of carbon dioxide adsorption on a faujasite-type zeolite. *Applied Surface Science, 256*, 5259-5262.

Avila, A. M., Yang, F., Shi, M., & Kuznicki, S. M. (2011). Extraction of ethane from natural gas at high pressure by adsorption on Na-ETS-10. *Chemical Engineering Science, 66*, 2991-2996.

Aycaguer, A.-C., Lev-On, M., & Winer, A. (2001). Reducing Carbon Dioxide Emissions with Enhanced Oil Recovery Projects: A Life Cycle Assessment Approach. *Energy & Fuels*, 303-308.

Baltusaitis, J., Schuttlefield, J., Zeitler, E., & Grassian, V. H. (2011). Carbon dioxide adsorption on oxide nanoparticle surfaces. *Chemical Engineering Journal, 170*, 471-481.

Breck, D. W. (1974). *Zeolite Molecular Sieves.* New York: Wiley.

Camarinha, E. D., Lito, P. F., Antunes, B. M., Otero, M., Zhi, L., Rocha, J., et al. (2009). Cadmium (II) removal from aqueous solution using microporous titanosilicate ETS-10. *Chemical Engineering Journal*, 108-114.

Chang, F.-Y., Chao, K.-J., Cheng, H.-H., & Tan, C.-S. (2009). Adsorption of CO2 onto amine-grafted mesoporous silicas. *Separation and Purification Technology, 70*, 87-95.

Chang, P.-H., Chang, Y.-P., Chen, S.-Y., Yu, C.-T., & Chyou, Y.-P. (2011). Ca-Rich Ca-Al-Oxide, High-Temperature-Stable Sorbents Prepared from Hydrotalcite Precursors: Synthesis, Characterization, and CO2 Capture Capacity. *ChemSusChem, 4*, 1844-1851.

Chatti, R., Bansiwal, A. K., Thote, J. A., Kumar, V., Jadhav, P., Lokhande, S. K., et al. (2009). Amine loaded zeolites for carbon dioxide capture: Amine loading and adsorption studies. *Microporous and Mesoporous Materials, 121*, 58-89.

Chowdhury, T., Shi, M., Hashisho, Z., Sawada, J. A., & Kuznicki, S. M. (2012). Regeneration of Na-ETS-10 using microwave and conductive heating. *Chemical Engineering Science, 75*, 282-288.

Feng, X., Fryxell, G. E., Wang, L.-Q., Kim, A. Y., Liu, J., & Kemner, K. M. (1997). Functionalized Monolayers on Ordered Mesoporous Supports. *Science, 276*, 923-926.

Goff, J. A. (1957). Saturation pressure of water on the new Kelvin temperature scale. *Transactions of the American Society of Heating and Ventilating Engineers*, (pp. 347-354).

Grasa, G. S., & Abanades, J. C. (2006). CO2 Capture Capacity of CaO in Long Seris of Carbonation/Calcination Cycles. *Industrial & Engineering Chemistry Research, 45*, 8846-8851.

Hiyoshi, N., Yogo, K., & Yashima, T. (2005). Adsorption characteristics of carbon dioxide on organically functionalized SBA-15. *Microporous and Mesoporous Materials, 84*, 357-365.

Jeong, N. C., Lee, Y. J., Park, J.-H., Lim, H., Shin, C.-H., Cheong, H., et al. (2009). New Insights into ETS-10 and Titanate Quantum Wire: A Comprehensive Characterization. *Journal of the American Chemical Society, 131*, 13080-13092.

Jeong, N. C., Lim, H., Cheong, H., & Yoon, K. B. (2011). Distribution Pattern of Length, Length Uniformity, and Density of TiO3 2- Quantum Wires in an ETS-10 Crystal Revealed by Laser-Scanning Confocal Polarized Micro-

Raman Spectroscopy. *Angewandte Chemie International Edition, 50*, 8697-8701.

Jou, F. -Y., Deshmukh, R. D., Otto, F. D., & Mather, A. E. (1987). Vapor-liquid equilibria for acid gases and lower alkanes in triethylene glycol. *Fluid Phase Equilibria, 36*, 121-140.

Kaye & Laby Online. (1995). *2.2.4 Mean velocity, free path and size of molecules.* Retrieved January 7, 2013, from Tables of Physical & Chemical Constants: http://www.kayelaby.npl.co.uk/general_physics/2_2/2_2_4.html

Knofel, C., Descarpentries, J., Benzaouia, A., Zelenak, V., Mornet, S., Llewellyn, P. L., et al. (2007). Functionalised micro-/mesoporous silica for the adsorption of carbon dioxide. *Microporous and Mesoporous Materials, 99*, 79-85.

Ko, Y. G., Shin, S. S., & Choi, U. S. (2011). Primary, secondary, and tertiary amines for CO2 capture: Designing for mesoporous CO2 adsorbents. *Journal of Colloid and Interface Science, 361*, 594-602.

Kovscek, A. R., & Cakici, M. D. (2005). Geologic storage of carbon dioxide and enhances oil recovery. II. Cooptimization of storage and recovery. *Energy Conversion and Management*, 1941-1956.

Kuznicki, S. M. (1989, August 1). *Patent No. 4,853,202.* United States.

Kuznicki, S. M., Anson, A., Koenig, A., Kuznicki, T., Haastrup, T., Eyring, E. M., et al. (2007). Xenon Adsorption on Modified ETS-10. *The Journal of Physical Chemistry C, 111*, 1560-1562.

Kuznicki, S. M., Thrush, K. A., & Garfinkel, H. M. (1993, January 7). *Patent No. WO 93/00152.*

Li, G., Xiao, P., & Webley, P. (2009). Binary Adsorption Equilibrium of Cabon Dioxide and Water Vapor on Activated Alumina. *Langmuir*, 10666-10675.

Liu, Z., Grande, C. A., Li, P., Yu, J., & Rodrigues, A. E. (2011). Adsorption and Desorption of Carbon Dioxide and Nitrogen on Zeolite 5A. *Separation Science and Technology, 46*, 434-451.

Lu, H., Smirniotis, P. G., Ernst, F. O., & Pratsinis, S. E. (2009). Nanostructured Ca-based sorbents with high CO2 uptake efficiency. *Chemical Engineering Science, 64*, 1936-1943.

Luca, V., Osborne, M., Sizgek, D., Griffith, C., & Araujo, P. Z. (2006). Photodegradation of Methylene Blue Using Crystalline Titanosilicate Quantum-Confined Semiconductor. *Chemistry of Materials, 18*, 6132-6138.

Lv, L., Tsoi, G., & Zhao, X. S. (2004). Uptake Equilibria and Mechanisms of Heavy Metal Ions on Microporous Titanosilicate ETS-10. *Industrial & Engineering Chemistry Research*, 7900-7906.

Maciver, D. S., Tobin, H. H., & Barth, R. T. (1963). Catalytic Aluminas I. Surface Chemistry of Eta and Gamma Alumina. *Journal of Catalysis*, 485-497.

Nak, C., Young, J., Park, J.-H., Lim, H., Shin, C.-H., Cheong, H., et al. (2009). New insights into ETS-10 and titanate quantum wire: A comprehensive characterization. *Journal of the American Chemical Society*, 13080-13092.

Nielsen, R., & Kohl, A. L. (1997). *Gas Purification* (5th ed.). Houston, TX: Elsevier Gulf.

Palmeri, N., Cavallaro, S., & Bart, J. C. (2008). Carbon Dioxide Absorption by MEA- A preliminary evaluation of a bubbling column reactor. *Journal of Thermal Analysis and Calorimetry, 91*, 87-91.

Park, S.-W., Lee, J.-W., Choi, B.-S., & Lee, J.-W. (2005). Kinetics of Absorption of Carbon Dioxide in Monoethanolamine Solutions of Polar Organic Solvents. *Journal of Industrial and Engineering Chemistry, 11*(2), 202-209.

Pavel, C. C., Vuono, D., Catanzaro, L., De Luca, P., Bilba, N., Nastro, A., et al. (2002). Synthesis and characterization of the microporous titanosilicates ETS-4 and ETS-10. *Microporous and Mesoporous Materials*, 227-239.

Ramis, G., Busca, G., & Lorenzelli, V. (1991). Low-temperature CO2 adsorption on metal oxides: spectroscopic characterization of some weakly adsorbed species. *Materials Chemistry and Physics, 29*, 425-435.

Sayari, A., & Harlick, P. J. (2010, August 3). *Patent No. US 7,767,004 B2*. United States.

Shi, M., Lin, C. C., Kuznicki, T. M., Hashisho, Z., & Kuznicki, S. M. (2010). Separation of a binary mixture of ethylene and ethane by adsorption on Na-ETS-10. *Chemical Engineering Science, 65*, 3494-3498.

Solomon, S., Quin, D., Manning, M., Marquis, M., Averyt, K., Tignor, M. M., et al. (2007). *Climate Change 2007I: The Physical Science Basis.* Cambridge, UK: Intergovernmental Panel on Climate Change, Cambridge University Press.

United Nations Statistics Division. (2012). *Carbon dioxide emissions (CO2), thousand metric tons of CO2 (CDIAC).* Retrieved December 10, 2012, from UNData: http://data.un.org/Data.aspx?q=Carbon+dioxide+emissions+(per+capita)+CFCs&d=MDG&f=seriesRowID%3a749

United States Energy Information Administration. (2011). *International Energy Outlook 2011*.

Wang, S., Yan, S., Ma, X., & Gong, J. (2011). Recent advances in capture of carbon dioxide using alkali-metal-based oxides. *Energy & Environmental Science, 4*, 3805-3819.

Wang, Y., & LeVan, M. D. (2009). Adsorption Equilibrium of Carbon Dioxide and Water Vapor on Zeolites 5A and 13X and Silica Gel: Pure Components. *Journal of Chemical & Engineering Data, 54*, 2839-2844.

Yilmaz, B., Warzywoda, J., & Sacco, A. (2006). Spectroscopic characterization of the quantum wires in titanosilicates ETS-4 and ETS-10. *Nanotechnology, 17*, 4092-4099.

Zelenak, V., Halamova, D., Gaberova, L., Bloch, E., & Llewellyn, P. (2008). Amine-modified SBA-12 mesoporous silica for carbon dioxide capture:

Effect of amine basicity on sorption properties. *Microporous and Mesoporous Materials, 116*, 389-364.

Zhao, Y., Shen, Y., & Bai, L. (2012). Effect of chemical modification on carbon dioxide adsorption property of mesoporous silica. *Journal of Colloid and Interface Science, 379*, 94-100.

Zhao, Z., Cui, X., Ma, J., & Li, R. (2007). Adsorption of carbon dioxide on alkali-modified zeolite 13X adsorbents. *International Journal of Greenhouse Gas Control, I*, 355-359.

Zukal, A., Mayerova, J., & Kubu, M. (2010). Adsorption of Carbon Dioxide on High-Silica Zeolites with Different Framework Topology. *Topics in Catalysis, 53*, 1361-1366.